OPERATIONS, ACCELERATOR PHYSICS, AND INSTRUMENTATION

K1200 OPERATING EXPERIENCE

D.R. Poe, H.A. Thulin and P. Miller

Table I shows operating time statistics for the K1200 cyclotron in 1993, and Table II shows the various beams which were run. There were 78 beams with 138 different beam changes, in 6386 hours of operation, and 5102.25 hours of research. This means that there was a beam change every 46.3 hours of operation, and every 37.0 hours of research time.

There were 5102.25 hours of research time in 1993 against 4993.5 hours in 1992. The category of operation, or (research + development + overhead), which represents the time that the cyclotron was running, went from 6625.5 to 6386 hours in 1993. The efficiency as defined in Table I, which is the time the cyclotron ran divided by the time that we tried to run it, increased from 88.8 % to 90.8 %. There were also 68 hours of startup time. This is the time, after a cyclotron shutdown, during which the machine is being brought back up.

The total number of hours in 1993 was 8760. Research was therefore carried on 58.3 % of the time, and operation 72.9 %.

As noted last year, the dee stems are now using silicone rubber O-rings. This seems to be a success. Further attempts to replace them with delta seals have been unsuccessful, owing to problems with leaks.

During the months of June, July and August, the RF system used the anode power supply of the K500 cyclotron, the Transrex, as there was damage to the rectifier circuitry during a trial run of a 200 MeV/u beam. This meant that the higher energy beams could not be run at this time.

The project was completed of replacing the electromechanical switches in the trim coil power supplies which power the bumps with all electronic switches of NSCL design. These switches are prone to failure due to their frequent usage, so the all electronic variety are improving the reliability, as well as making the cyclotron easier to tune.

Deflectors are now able to run up to 120 KV/CM operatonally, or 72 KV, and we have had tests at 80 KV with some beam time there. Both E1 and E2 are now running with anodized aluminum shoes, and spares of this type are being made. The anodized layer is believed to help control electron emmision from the negative surface. As reported last year, E1 now has a water cooled housing on the segment in which the beam enters, and we have changed to a new model of insulator, which is made of Macor with titanium end caps, has a larger diameter than the old version (for strength), and has flutes cut into the side to inhibit electron travel along the length of the insulator. This change has been a success, as they have proved rugged and reliable. We have adopted the operational technique of treating the deflectors with a high pressure oxygen bath at voltage as a form of rapid reconditioning when they begin drawing current. This has frequently allowed us to resume operations in less than 1/2 hour after the onset of trouble.

TABLE I K1200 Time Distribution 1993

	Hours	Percentage
Operation		
Research	5102.25	70.23
Development	257.25	3.54
Overhead	1026.50	14.13
(R + D + O)	6386.00	87.90
Maintenance	234.00	3.22
Breakdown	645.25	8.88
TOTAL	7265.25	100.00%
OFF	1425.75	
STARTUP	68.00	

EFFICIENCY = E
= (R + D + O) / (TOTAL - MAINTENANCE)

E = 6386.00 / (7265.25 - 234.00)
= 0.908 = 90.8 %

TABLE II K1200 BEAMS 1993

Ion	E/A [MeV/u]	Hours	% Time
2 D 1+	155	2.0	0.0
3 (H-D) +	70	17.0	0.3
4 He 2+	155	72.5	1.4
4 He 2+	145	12.0	0.2
4 He 1+	60	39.5	0.8
4 He 1+	50	223.0	4.3
4 He 1+	40	55.0	1.1
5 (He-H)+	35	71.0	1.4
6 Li 2+	100	343.3	6.6
6 (He-D)+	22	3.0	0.1
7 Li 2+	50	160.5	3.1
11 B 2+	32	103.8	2.0
12 C 6+	155	26.0	0.5
12 C 5+	125	8.0	0.2
12 C 4+	100	45.8	0.9
12 C 4+	75	39.5	0.8
12 C 4+	70	10.0	0.2
12 C 3+	60	144.8	2.8
12 C 3+	40	8.5	0.2
12 C 2+	22	20.8	0.4
14 N 7+	155	38.8	0.7
14 N 6+	130	40.5	0.8
14 N 6+	100	5.5	0.1
14 N 4+	70	166.0	3.2
14 N 3+	35	8.8	0.2
16 O 8+	155	24.8	0.5
16 O 6+	80	191.8	3.7
16 O 5+	70	15.3	0.3
16 O 4+	70	14.0	0.3
16 O 4+	40	41.3	0.8
17 O 3+	25	73.0	1.4
18 O 6+	100	32.5	0.6
18 O 6+	80	573.8	11.0
18 O 5+	60	131.0	2.5
18 O 4+	35	63.0	1.2
20 Ne 10+	155	55.8	1.1
20 Ne 8+	115	16.8	0.3
20 Ne 8+	110	110.5	2.1
20 Ne 4+	40	113.5	2.2
22 Ne 6+	70	119.5	2.3
28 Si 14+	155	30.0	0.6
28 Si 8+	70	10.0	0.2
28 Si 7+	40	12.0	0.2
36 Ar 12+	100	10.8	0.2
36 Ar 8+	35	9.5	0.2
40 Ar 16+	115	51.3	1.0
40 Ar 14+	95	33.3	0.6
40 Ar 13+	80	41.5	0.8
40 Ar 12+	80	103.3	2.0
40 Ar 11+	55	21.0	0.4
40 Ar 10+	40	16.5	0.3
40 Ca 12+	80	118.3	2.3
48 Ca 16+	100	14.5	0.3
48 Ca 11+	55	51.5	1.0
56 Fe 14+	50	8.5	0.2
60 Ni 24+	115	15.0	0.3
64 Ni 15+	60	38.3	0.7

78 Kr 22+	75	146.8	2.8
81 Kr 17+	45	20.3	0.4
84 Kr 14+	22	23.3	0.4
84 Kr 19+	50	75.8	1.5
86 Kr 21+	60	5.5	0.1
86 Kr 19+	45	11.0	0.2
106 Cd 26+	60	122.3	2.4
126 Xe 23+	35	72.5	1.4
129 Xe 32+	70	114.0	2.2
129 Xe 28+	50	126.3	2.4
129 Xe 26+	40	20.0	0.4
129 Xe 26+	30	16.5	0.3
129 Xe 23+	30	202.8	3.9
129 Xe 24+	30	1.8	0.0
129 Xe 19+	20	39.8	0.8
136 Xe 25+	35	2.0	0.0
136 Xe 24+	30	216.0	4.2
136 Xe 24+	28.4	44.0	0.8
197 Au 36+	35	55.0	1.1
197 Au 32+	25	29.8	0.6
238 U 35+	20	25.5	0.5

DEVELOPMENT OF 200 MeV PER NUCLEON $^{16}O^{8+}$ BEAM FROM THE K1200

T. Antaya, H. Blosser, F. Marti, P. Miller, and D. Poe

The highest velocity (or correspondingly, energy per nucleon) beams that the K1200 cyclotron is designed to produce are the ions with charge to mass ratio Q/A= 0.5 at 200 MeV per mass unit (u). The beam velocity is 0.568 c, where c is the speed of light. This operating point is at the focusing limit for the cyclotron magnet. On Feb 2, 1994 a beam of $^{16}O^{8+}$ ions was accelerated to 200 MeV/u and detected in the beam line outside the cyclotron by observation of a scintillator with television and by the beam current absorbed in a Faraday cup. This demonstration confirms that the K1200 works for this high energy case, one we expect to use extensively in the future. The success of this experiment was the result of contributions from staff, students and visitors at the NSCL over many years and was a source of satisfaction for many persons, within and outside of the NSCL.

In 1992 the decision was made to schedule time for beam tests leading to the goal of 200 MeV/u. In October 1992 a 170 MeV/u He beam was extracted, and 200 MeV/u beams were accelerated near extraction radius but were not extracted. Problems with the anode power supply for the rf transmitters postponed development of high energy beams for some months. After new rectifiers were procured and installed the power supply worked properly again. In October 1993 both 190 and 200 MeV/u beams were attempted. A centered beam was obtained in the cyclotron but it was lost before extraction due to an upward axial displacement. During subsequent experiments to study this problem we encountered failures of sliding contacts in the rf resonators. Some contact fingers on the shorting plane to the outer conductor burned out, apparently due to insufficient contact force. The problem has been corrected in one resonator by several improvements to the fit and assembly of the components.

The operating diagram for the K1200 calls for deviation from the isochronous magnetic field profile to enhance vertical focusing of the beam. In the 200 MeV/u field this deviation is slightly greater than for lower energy. We found that the optimum operating point had currents in the main magnet coils that were a few amperes outside of the previously selected operating boundary. The boundary definition was adjusted to include the desired operating point (920.4/ -384.7 A) within the safe operating range. The minimum value of ν_z was 0.151, and the phase deviation was still usable ($-0.51 < \sin \phi < 0.69$).

A water cooled load resistor was reinstalled on the output of each rf transmitter to damp harmonic frequencies. It was necessary to add a 12 pF coupling capacitor to prevent flashover of the

insulation of the load resistor under transient overvoltage conditions and to get the desired frequency response.

When runnning the rf system at high power we observed an increase of the pressure in the beam chamber. This was due to an air leak that appeared only when operating at high dee voltage (> 110 kV peak) and at frequencies above 20 MHz. The leak, which was not detectable when the rf power was lowered, was shown to be at the vacuum feedthru for a dee fine tuner capacitor. The indium seals were replaced, and the leak was gone. Another leak developed in a different part of the accelerator about 3 days before the desired external beam was achieved. This leak was in the cover of trim coil 0 in the center of the lower magnet pole. The metal liner for the beam chamber was eroded by action of dee sparks. At one place the sparks had punctured the liner and the stainless steel trim coil cover behind it. Trim coil 0 is in contact with the atmosphere, so air could leak into the beam chamber through the puncture. A guard vacuum was established using an external pump to allow completion of beam development. The leak was permanently repaired afterwards.

We discovered that the destructive axial deflection of the beam at large radius could be cancelled by moving the main magnet coil upward. This was attributed to a mismatch of the median planes of the coil and the iron poles. The same effect was reported at the K500 cyclotron at Texas A&M university [1]. The beam deflection for a given mismatch depends on the radial derivative of the coil field and on the axial focusing frequency such that the deflection of the beam increases very rapidly as the final energy is increased. The effect was not noticeable at 170 MeV/u and below. The coil was moved upward by 0.025 inches in two trials, +0.040 in., then -0.015 in. After this the beam was extracted with no measureable vertical deflection of the internal beam centroid.

References

1. D.P. May and G. Mouchaty, "Effect of the Main Coil Position on the Accelerated Beam of the K500 Cyclotron" in Cyclotrons and Their Applications, Proc. 13th International Conference, G. Dutto and M.K Craddok, eds. World Scientific(1992) 439

MEASUREMENTS OF HIGH-ENERGY BEAM EMITTANCE

J. Stetson

In the past year, beam emittances for about 45 extracted beams were determined. These values were derived from TRANSPORT fits to beam sizes measured at 4 successive locations (A-12, A-04, A001, & A004) in the beam line.

The average measured horizontal emittance was 2.2 π*mm*mr, with values ranging from 0.6 to 7.7 π*mm*mr. The average measured vertical emittance was 5.1 π*mm*mr, with values ranging from 1.3 to 14.7 π*mm*mr. The orientation of the phase ellipses was remarkably consistent, as shown in figure 1.

Making these measurements is, at present, a fairly labor-intensive process: photographing the beam at the 4 locations, manually determining beam size by scaling from reference marks on the viewers, entering by hand the sizes and quadrupole strengths into TRANSPORT, and fitting. Additionally, to obtain the best beam spot, fitting to the required characteristics using the measured beam parameters as input then setting the fitted quadrupole values, is desirable. In the coming year, steps will be taken to automate this procedure using PC-based frame-grabber technology.

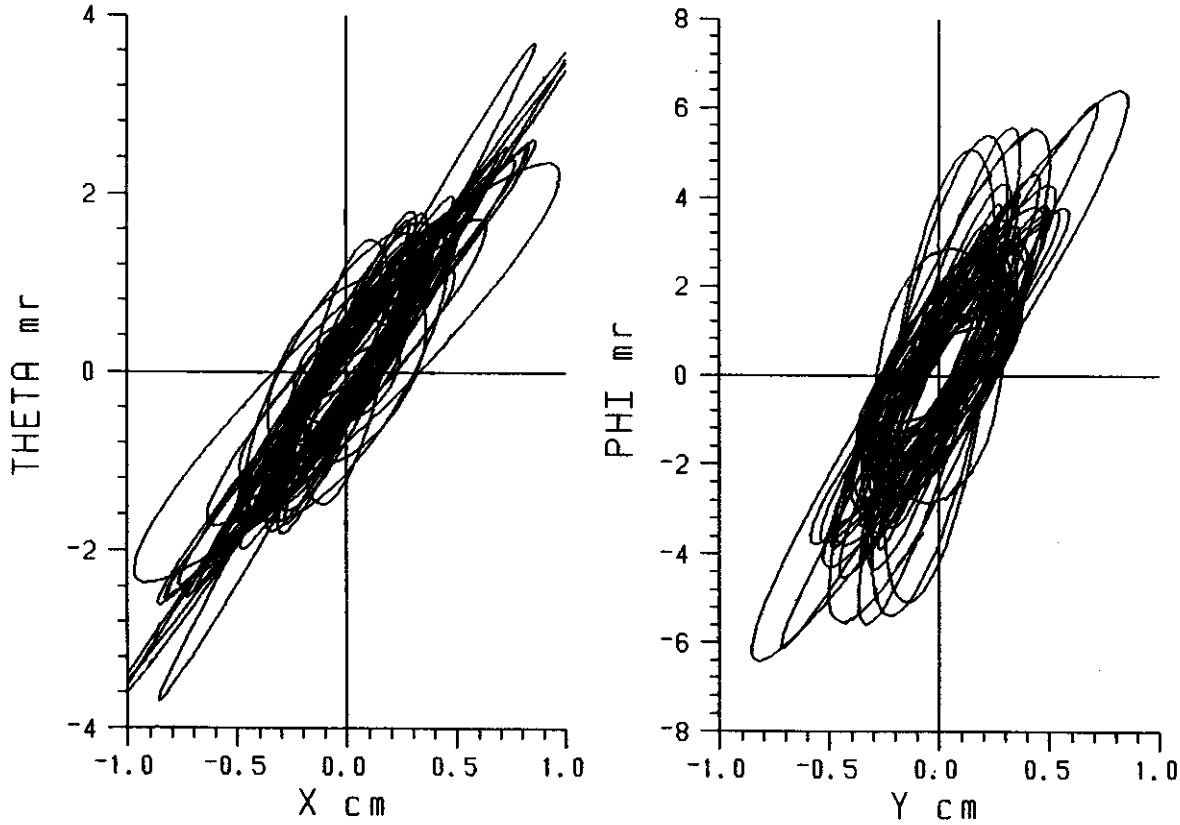

Figure 1: 40 Measured Beam Phase Ellipses at the Start of the High-Energy Beam Line.

MEASUREMENT OF POSITIONS OF K1200 EXTRACTION ELEMENTS

P. Miller, D. Poe, A. McCartney, and G. Stork

The electrostatic and magnetic channels used to guide the beam out of the K1200 cyclotron are be moved radially by remote controlled motors to accomodate the different trajectories represented by the possible range of ions and energies produced. Due to the large number of devices and their sensitivity it is necessary to preset the channel positions accurately. We measured the positions of 24 (out of 26 total) drives for these devices and compared to the positions displayed by the control system. The calibration constants were corrected based on analysis of these measurements.

Measurements

On each drive the position was measured at 3 or 4 places, usually the inner limit, the outer limit and two points between. The radius from the center of the cyclotron to a known point on the extraction channel was measured, e.g. to the inner face of the septum of the electrostatic deflectors. The radius at the center of the beam aperture was inferred by adding or subtracting a constant offset determined by the appropriate dimensions of the channel, e.g. for the electrostatic deflectors add the septum thickness plus one half the radial aperture from septum to high voltage electrode. For E1 and E2 the aperture was 0.236 inches (6.0 mm).

For the focusing bars M1-M6 the radius to the center of the physical aperture was determined, just as described for the electrostatic deflectors. Along with the radius measurement the control system display of position along the drive direction (inches from an arbitrary zero) and the follow pot voltage measured by the control system were recorded. The radius was measured from a center fixture positioned by dowels in the pole tips of the cyclotron magnet. An inside micrometer with various extension rods measured the radius. The precision for this measurement was ±0.003 inches; systematic errors of the micrometer and extensions are less than 0.005 inches. The location of the center was compared to the center position of a fixture that mounted only to the center plug rf cover, which may be offset relative to the pole tips. The offset measured was 0.015 inches.

Two of the channels, M5 and M6, were not accessible directly with the inside micrometer since they lie behind the wall of the magnet cryostat. These channels lie on either side of access port A5, so fixtures were built to insert into the beam aperture of each. The radius to the end of the fixture in A5 was measured. No such access to M7 or M8 was possible, so their positions were not measured.

The results of the calibration are in Table 1. The second column gives the azimuth θ relative to the zero degree hill of the point on the drive axis which is the origin of the horizontal coordinate for the channel or compensator. For channels the coordinate origin is the center of the beam aperture. The third column gives the the angle α between the radius from the cyclotron center and the drive axis. The fourth column contains R_0, the radius to the channel coordinate origin when the drive position displays zero. Since the position display, called DI below, is calibrated in inches along the drive direction, the radius of the channel origin for any position is given by

$$R = R_0 + DI/\cos\alpha. \qquad (1)$$

A majority of the channels are usually positioned at the same radius as the beam passing through them, but often it is necessary to fine-tune the exit beam position by moving one or more of the focusing channels (max. 0.10 in.) to match to the beam line. The focusing channels M1-M8 have a horizontal aperture of 0.50 in.

The useful range of DI is typically about 1.2 inch (e.g. -0.4 to +0.8 inch). The deviation of the measured "inches per volt" slope used to convert the follow pot voltage to inches is 1-2% in all cases. This is small enough to be neglected. Therefore we did not change the calibration constants for the control system (slope and offset). We corrected all discrepancies by adjusting R_0. The amount of this adjustment (present R_0 - previous R_0) is tabulated as ΔR_0.

Limit switches

The position readout DI at the inner and outer limit switch positions is given in Table 1. For E1 and C2 there are additional switches which constrain the drives to prevent collision of the devices. These switches are mounted on a mechanism that links the drives and reproduces the gap between the back of E1 and the front of C2. The limit switches disable the appropriate drives before contact occurs. We had to enlarge this gap by removing a portion of the E1 housing to a depth of about 0.15 inches where it faces C2. This allowed us to reach the optimum positions for all beams. The constraint can be expressed by two inequalities involving the positions DI_i for the drives E1B, E1C, C2A and C2B.

$$DI_{C2A} > 0.7189\, DI_{E1B} + 0.2811\, DI_{E1C} - 0.210. \qquad (2)$$

$$DI_{C2B} > 0.8333\ DI_{E1C} + 0.1667\ DI_{E1B} - 0.270\ . \qquad (3)$$

If both inequalities are satisfied there is no contact. Of course, the limit switches sense this directly. The inequalities are used to check that a set of calculated positions is actually allowed by the interlock.

Conclusion

As can be seen in Table 1 several drives were corrected for significant calibration errors, up to 0.1 inch. This was necessary to have the beam position match predictions. The agreement between the cyclotron and the computer model used for presetting the extraction system is now accurate enough that the beam appears outside the cyclotron without repositioning channels once the extracted beam position is correct on the A2 probe, which is between B1 and M2.

Table 1--Drive calibration data.

Name	θ [deg]	α [deg]	Ro [in]	ΔR [in]	DI inner limit [in]	DI outer limit [in]
E1A	31.0	9.32	39.956	0.078	-0.216	0.920
E1B	51.0	10.10	40.739	0.033	-0.600	0.761
E1C	72.0	11.10	40.875	-0.033	-0.437	0.700
E1D	89.0	0	40.399	-0.077	-0.397	0.855
E2A	151.0	9.40	40.775	0.054	-0.688	0.788
E2B	174.0	12.55	41.566	0.001	-0.416	0.726
M1	94.0	0	40.311	0.011	-0.368	0.875
C3	214.0	0	40.323	0.023	-0.371	0.875
C4	334.0	0	40.313	0.013	-0.499	0.901
B1A	175.0	5.04	41.625	-0.030	-0.404	0.725
C1A	297.0	5.36	42.271	-0.016	-0.341	0.781
C2A	57.0	3.34	42.184	-0.103	-0.331	0.791
B1B	191.0	9.17	41.835	-0.070	-0.385	0.700
C1B	309.0	5.36	42.446	-0.030	-0.352	0.792
C2B	69.0	7.42	42.372	-0.105	-0.349	0.795

M2	214.0	0	41.669	-0.001	-0.460	0.940
C5	334.0	0	41.565	-0.105	-0.393	1.007
C6	94.0	0	41.665	-0.005	-0.487	0.913
M3	260.0	0	42.482	0.011	0.001	4.326
M4	293.0	0	43.761	0.001	-0.454	0.661
M5	314.25	11.40	44.937	-0.013	-0.311	0.603
M6	329.6	0	46.474	-0.086	-0.183	0.551
M7	340.0	0	48.220	NA	-0.216	3.915
M8	349.0	0	50.500	NA	-0.334	0.535
C7	97.0	0	45.377	-0.023	-2.798	0.252
C8	144.0	0	43.566	-0.034	-0.910	0.285

NSCL CONTROL SYSTEM DEVELOPMENTS

J. Priller, L. Foth, and J. Vincent

Introduction

The most important change in the NSCL control system over the last two years has been the introduction of Intel-based "IBM compatible" PCs, running Microsoft Windows, as the primary control and monitoring workstations. The VAX/VMS color graphics workstations used previously had the advantage of a robust and mature operating system (VMS), but were based on an expensive and proprietary hardware platform. Interface boards (such as arcnet communications boards) and device drivers for the VAX workstations' QBUS architecture were expensive and becoming increasingly more difficult to find, and the VMS software development tools and environment were comparatively primitive and cumbersome. While the operating systems for the PC platform (Microsoft Windows, and more recently Microsoft Windows for Workgroups) are not as stable a platform as VMS, the many advantages of the PC platform outweigh this consideration. PCs are inexpensive, and use open industry standards for their CPUs, I/O buses, and peripheral components. PC hardware and software components are also inexpensive, and are available from a wide variety of manufacturers. PC-based development tools are more sophisticated than their VMS counterparts, and provide a considerably shorter development cycle. Finally, a large number of third-party tools and applications exist for the PC's Microsoft Windows environment, which can be interfaced with the NSCL control system software via Window's DDE and OLE data-sharing methods.

A Typical Control Workstation

A typical control system PC workstation, such as those used at the NSCL main console, consists of the following components. The prices listed are as of May 1994, and are likely to decrease as time goes on.

Industrial case w/power supply	350
486-66DX2 ISA/VLB motherboard w/IDE controller	750
16MB RAM	1,350
340MB IDE hard drive	280
3.5" 1.44MB floppy drive	50
VESA-Localbus accelerated video board	170
17" 1024x768NI multisync monitor	950
Ethernet board	230
Arcnet board (for VME data)	100
16550-based serial board (for Modicon data)	50
Keyboard	90
Trackball	115
MS Windows-for-Workgroups	100
MS-DOS 6.2	60
Total	4,645

Interface Hardware

The control system PCs at NSCL interact with both of the primary control subsystems, the

VME/Fermi subsystem and the Modicon/PLC subsystem. The VME/Fermi interface is performed via arcnet to a VME create acting as a data server. A data-server simplifies the PC's arcnet-request software considerably, as it no longer has to break up data requests that span multiple VME crates. The data-server handles breaking up the requests, and also controls the knob and meter hardware panels associated with each workstation PC (these are described more fully in a later section).

The Modicon/PLC interface is currently performed via a serial line linking the PC to a port on a Modbus multiplexor. This serial line interface is comparatively slow (it typically runs at 19.2k-baud, compared to arcnet's 2M-baud), but is sufficient to support a small number of concurrent Modicon/PLC-data-requesting programs. The nature of Modicon/PLC data (largely target ladders and interlocks) is such that it changes slowly, and so a response time on the order of a few seconds is not considered problematical.

Operating System Platforms

Initial development of the NSCL control system software was done for the Microsoft Windows 3.1 operating environment. This same software is also supported on the newer, network-aware version of Microsoft Windows, Windows for Workgroups 3.11. Work is in progress on control system software for Microsoft's 32-bit Windows platform, Windows NT. This software will also be supported on Microsoft's next version of Windows, Windows 4.0 (usually referred to by its code-name, "Chicago").

Major Applications

Some of the major control system applications developed thus far are described briefly below.

Chart Recorder

This application allows eight VME analog channels to be simultaneously monitored, with their readings graphed in a scrolling, chart-recorder-like fashion. The time scale for the graph is adjustable, and each channel has separate and configurable scaling and offset parameters. Pen colors for the eight channels are also configurable. Multiple chart recorder programs may be run simultaneously.

Knob/Meter Application

The knob/meter application provides an interface to the VME hardware knobs and meters that accompany PC control system workstations (these are described in a later section). It provides an interface where VME-channel knob and meter assignments can be made and broken, and where device readings and reading-to-setting differences can be viewed. Several types of knob ganging and "row-mode" banking assignments are provided, as well as user-defined "knob functions" comprised of multiple device channels and scaling factors. Hardware meter ranges can be changed. Device settings can be saved and restored. As this program interacts closely with the hardware meters and knobs associated with the PC workstation, only a single instance of it may be run at a time.

PanelMate Emulator

This application was developed in response to the increasing cost of maintaining the IDT PanelMate systems used for Modicon PLC monitoring and control at NSCL. The screen layout of the program is designed to closely mimic the look of a PanelMate III screen, with a simple mouse-based interface replacing the membrane-key interface of the IDT product. Template configuration is done via menus and dialog boxes, with all inputs again closely mimicking those of an actual PanelMate. Multiple instances on the PanelMate Emulator may be run simultaneously.

DDE Server

The DDE Server process is capable of responding to VME and Modicon data requests made by DDE-

aware third-party Windows applications, such as spreadsheets (Excel, Lotus 123, Quattro Pro), graphing programs (Harvard Graphics, Stanford Graphics) and databases (Microsoft Access, dBase, Paradox). This allows one to easily place "live" control system data into a spreadsheet and perform calculations with them. Such applications can also perform device settings, allowing a spreadsheet to calculate optimal settings for a given beam and then set beamline devices accordingly, for example.

VME Data Servers

As mentioned earlier, VME/Fermi stations acting as data servers assist the control system PCs. A VME/Fermi data server provides simplified access to VME control system data by allowing the PC to request data from any group of channels without regard to what stations actually contain those channels. When the PC makes the request, the VME/Fermi data server handles gathering the data fragments from the stations and combines them into a single response message. One data server can serve a number of PCs, depending on how much data each is requesting.

A data server crate can also act as a knob and meter server for the control system PCs. The knob and meter interface boards reside in the VME/Fermi crate. The VME/Fermi system accepts commands from the PC to assign up to eight knobs and 16 meters to control system channels. When an assigned knob is turned, the VME/Fermi server system sees that and sends out an appropriate setting to the assigned channel(s). Up to ten channels can be ganged together on each knob with varying multiplicative scaling factors. When a meter is assigned to a control system channel, the server collects and displays the reading on the meter 12 1/2 times per second. Each meter can be assigned to have any value as its full scale value. Also, the server can compute a running average using up to the last ten readings for any meter channels. All of this work is done directly by the VME/Fermi server without any intervention by the PC. The PC only issues commands to assign and deassign knob and meter channels, and set parameters such as scaling and averaging. This makes the knobs and meters much more responsive than they were when they had to be processed by the VAX Workstation. More than one PC can cooperate to share the eight knobs and 16 meters supported by a data server crate.

RPC Data Servers and Clients

Two software applications already developed for Microsoft Windows NT are DCE/RPC data server processes for both the VME/Fermi and the Modicon/PLC subsystems. These processes run on a Windows NT Advanced Server machine (which also acts as a file server for the control system workstation PCs) that possesses an arcnet card and a Modicon multiplexor serial link. These processes allow any DCE-compliant RPC computer, given the appropriate client software, to access the VME/Fermi and Modicon/PLC subsystems over it's ethernet link, rather than through local arcnet and serial connections. Client software has thus far been developed for Windows NT 3.1 and VAX/VMS 5.5-2. UNIX and Microsoft Windows-for-Workgroups client software is planned.

Future Directions

One direction already being taken with the control system software is the move from 16-bit Windows code, such as is used under Windows 3.1 and Windows for Workgroups, to 32-bit Windows, as is used under Windows NT and Windows 4.0 ("Chicago"). To make the code more portable, much of the underlying subsystem-interface software has been ported from Borland Pascal to ANSI C. Most of the application programs written thus far rely on libraries of object-oriented code written for Borland Pascal's ObjectWindows version 1.0, these will be ported to Borland C++ 4.0's ObjectWindows version 2.0. This platform allows us to create both 16-bit and 32-bit Windows applications and

libraries.

Another planned direction is to replace the serial-line access currently used in the Modicon/PLC subsystem with access via a Modicon Modbus-Plus interface board. This board will provide the substantially higher throughput needed for real-time control functions, and will allow a greater number of processes to access Modicon/PLC data without decreased response times.

RELIABILITY OF THE LIQUID HELIUM SUPPLY

H. Laumer

The operation of all superconducting magnets at the NSCL depends on liquid helium to maintain the operating temperature of the superconductor below the transition temperature. The reliability of the liquid supply is essential for successful operation of the laboratory. The main components of the liquid helium system are :

1) a helium liquefier rated to maintain 400 watt reliquefaction at 4.5K and at the same time make 100 l/hr rate-of-rise of liquid in a dewar, of 2500 l storage volume associated with it;

2) a CTI-1400 helium liquefier rated 25 l/hr at 4.5K or 100 watt in reliquefying mode, and its 500 l dewar;

3) three Sullair screw compressors supplying a total of 80 g/s at 250 psig,

4) gas storage tanks to hold 470 Kg of gas at 250 psig, and high pressure gas storage for 360 Kg to resupply them.

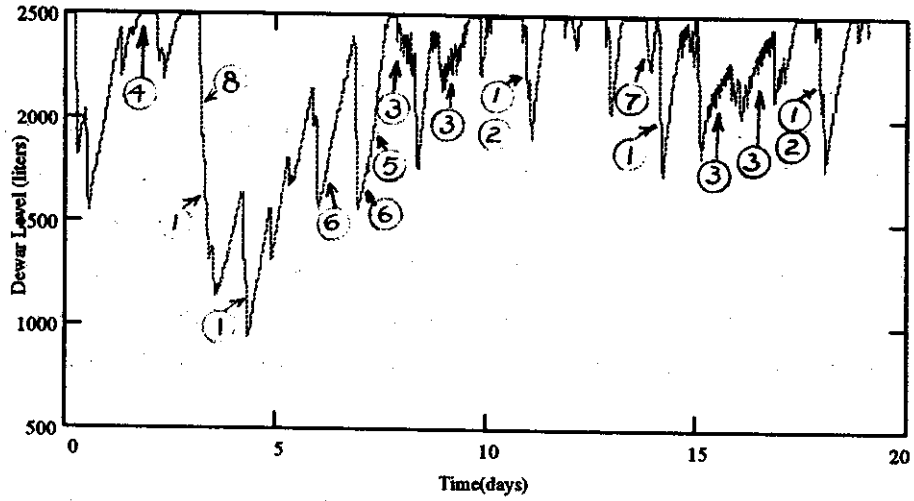

Figure 1: The Dewar level vs. time. (1) Typical beam line magnet fill cycle under computer control. (2) Three sets of beam line magnets filled on a weekly schedule. (3) Production rate limited by gas inventory. This appears as a saw-tooth pattern with a period of hours due to a heater in the 2500 l Dewar being turned on and off. In the weeks before a scheduled helium gas delivery the Dewar will never be full due to this limit. (4) Dewar is filled to maximum level. (5) A sharp change in production rate due to tuning expansion engines. Compare to rate at (6). (7) A filling cycle which failed to fill any magnets; the cause could not be ascertained. (8) A filling cycle that failed because a modicon controller had been left without power.

The dewar level can be used as a basis for predicting liquid supply reliability; the level is recorded every ten minutes. Figure 1 is a plot of level vs. time for a three week operating period. It is typical with respect to the usual beam line filling cycles. The K-500 cryopanels were off during this period. Turning them on would decrease the production rate if liquefier performance is not changed. No losses due to mechanical failure were observed in this operating period. By accumulating dewar level data for a year the fractional time vs. dewar level

can be generated as shown in figure 2 for 1993. From this figure it can easily be determined what fraction of time the dewar was completely full (16% of the time).

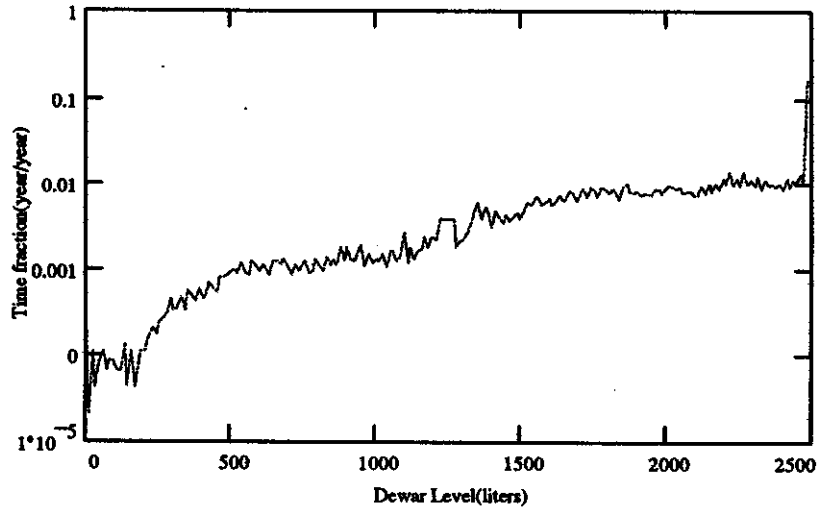

Figure 2. Fraction of the year 1993 vs. Dewar level in 12 liter increments

It is also possible to carry out other statistical calculations. For example: what is the probability that a compressor shutdown in 1993, which cost 1450 liters of liquid helium before restarting, will lead to a program disruption? Obviously, any time the dewar level is below 1450 liters, such an event will lead to turning off the cyclotrons since their cryostats will run low on liquid. The probability is 0.16, given by the area under the fractional time curve between 0 liters and 1450 liters. Similarly calculating PF the probability that any of the events associated with maintenance or failure of refrigerator hardware (there where 23 such events in 1993) lead to an interruption is given by

$PF=1-(1-P_1)(1-P_2)...(1-P_{23})$

where P_i is the probability that event i causes a disruption. And again P_i is obtained by finding the area under the curve appropriate for event i. For 1993 this probability is 0.37.

What effect would doubling the dewar capacity have on Figure 2? To first order, one would expect that the dewar would still be full 16% of the time for the following reason: the excess production rate available is still between 20 and 50 l/hr. Even at 20 l/hr the recovery rate is 2500l/20l/hr=125 hr. which is short compared to a year , the basis of Figure 2. The result is then that the curve is shifted up 2500 liters with a tail below 2500 l which is expected to account for very little time. Under this condition the event which cost 1450 liters will be very unlikely to cause disruption; no doubt the probability would drop from 16% to below 1%. The value of PF calculated above would see an equally dramatic decline. This shows that provided the excess capacity is enough to fill the available storage on the order of days, liquid storage can be a very effective means of reducing the odds for down time.

We have decided to link the 2500 liter Dewar with the 500 liter Dewar by an efficient transfer line. This line will make it possible to fill the 7 tesla solenoid and the S-800 beam line magnets from either Dewar, (it's reason for construction) and at the same time it increases the generally available stored liquid capacity.

What effect will increased demand due to more beam line magnets and the S-800 spectrometer have? Based on operating experience with equipment we have built in the past we have allocated 50 l/hr to this operating load. If we operate the liquefier under the same operating conditions we know we have available 16% of rate-of-rise production rate or about 12 l/hr. This value is a lower limit since whenever the heater is turned on in the dewar due to low gas inventory we also lose capacity. It may double the actual available capacity to 25 l/hr. As shown by an example in figure 1 the tuning of expanders can yield significant production rate improvements. We assign the observed value for this case at 30 l/hr. It is closely related to the increase that can still be achieved by operating expanders at higher speed since we must expect faster wear and the associated drop in engine efficiency. 80 l/hr is perhaps achievable as spare capacity. If the K-500 cryopanels and the 7-tesla solenoid have to be operated in addition to the S-800, we should expect serious problems.

As the spare capacity approaches 0, the shape of the curve in figure 2 will shift away from the 16% of the time full peak to distribute more time to lower dewar levels. Assuming that the excess production rate drops to 0 to 20 l/hr, would lead us to practically never expect a full dewar . Unfortunately operating engines at higher speeds to operate closer to maximum capacity will increase the maintenance and failure frequency of the engines. The effect on figure 2 will be to again shift more time to lower dewar levels. If the events for engine repair experienced in 1993 are scaled by the square of the engine speed the expected maintenance and failure rate of engines is expected to be 3 times higher. The total equivalent liquid helium to be made up based on 1993 events would increase from 15700 liters to at least 22600 liters (this assumes only losses due to engine maintenance will increase). At the same time excess production rate will drop. For example, if 50 l/hr was available before and 25 l/hr are expected under conditions of higher load; the makeup time, based on events experienced in 1993, then increases from 13 days to 38 days. The actual shape of figure 2 under these circumstances can only be predicted qualitatively. One has some control by scheduling beam line fills and preventive maintenance to avoid bottle necks. Ordering gas deliveries earlier will minimize production limitations and let total dewar capacity be exploited more fully. This will become more important as we operate closer to maximum capacity. It also must be realized that as the system becomes larger, unforeseen events are more likely to occur, and it becomes more difficult to pinpoint the cause of trouble.

It is quite evident that spare liquefaction capacity and increased gas and liquid storage are equally important in reducing the likelihood of beam time loss due to lack of liquid helium. To operate successfully when the S-800 system comes into operation it is desirable to have in place:

1)Dewar upgrade

2)The gas storage (30,000 gallon propane tank) to make the liquid accessible without incurring gas losses.

3)Compressor upgrade in the 30 to 60 g/s range to make full use of all on site helium liquefaction capacity.

4)Cooling tower upgrade.

5)Additional liquefaction capacity of 75 l/hr .

THE STUDY OF A 2.45 GHz PLASMA SOURCE AS A PLASMA GENERATOR FOR THE SCECR

A.K Srivastava*, J. Asmussen*, T. Antaya and K. Harrison

Introduction

For many years now, electron cyclotron resonance ion sources (ECRIS) have been used to inject energetic beams of highly charged ions into accelerators [4,5,6]. While the development of these ECRIS has progressed steadily, many performance related questions remain unanswered. The superconducting source (SCECR) at the National Superconducting Cyclotron Laboratory (NSCL), Michigan State University (MSU) is used in this study for further development of ECRIS technology.

Like many ECRIS, the SCECR is a two stage system. It consists of a "pre-ionizer" or the first stage, and a multimode microwave cavity downstream that acts as the main stage. The main stage is operated at a sufficiently low pressure to make highly charged ions. The SCECR has been demonstrated as having one of the world's best performance characteristics today [3,4]. While the necessity of having a first stage has been proved beyond doubt (removing it reduces performance of the main stage), there is some ambiguity as to the exact nature of its effect on the performance of the main stage. A unique opportunity to study this has arisen through a collaboration with the plasma laboratory of the Department of Electrical Engineering (EE) at MSU. The EE group has developed several ion and plasma sources for chemical vapor deposition, anisotropic etching of silicon, molecular beam epitaxy (MBE) and other materials processing applications [8,9,10]. One commercially available plasma and free radical source is the MPDR 610™, a compact coaxial multi-cusp ECR plasma source which has been comprehensively characterized in terms of its performance (such as ion density, electron and ion energies, and their distribution functions) relative to input parameters (pressure, gas flow rates, power, excitation frequency, etc.) [1,2]. This study aims to use the MPDR 610 as a substitute for the first stage on the SCECR and evaluate the relative performances of the two sources. The 610 is mounted such that it is floating relative to the SCECR, so that the effect of positive, negative, or neutral injection from the 610 into the main stage of the SCECR can be studied here. Also, since the 610 normally runs at 10^{-4} Torr pressures while the SCECR runs at pressures at least three decades lower, the important question of coupling a high pressure first stage to a low pressure main stage is addressed.

Experimental Results

Figure 1 is a cross-section of the SCECR with its original injector on top of the main stage. Since it uses superconducting electromagnets, the SCECR is a variable frequency source (theoretically, 5GHz - 35GHz). Axial confinement, which is of paramount importance for the creation of high charge states, is provided by a set of five solenoid coils. A pressure gradient in the first stage allows for a pressure differential between the two stages. The main stage is a fixed volume multi-mode cavity, from which multiply ionized beams are extracted using a three electrode spherical Pierce-type system.

Figure 2 shows the cross-section of the MPDR 610. The coaxial structure of the microwave cavity extends well beyond the loop antenna. The plasma is, however, created downstream from the center conductor of the cavity, enclosed in a quartz or alumina cup. For a specific input power and gas pressure, the cavity dimensions may be adjusted to tune the source. In this manner, up to 98 % of the incident power is absorbed by the plasma. Due to its coaxial nature, theoretically, the 610 can work at any frequency of excitation, provided the permanent magnets are strong enough to provide the necessary ECRH field strength.

Figure 3 shows the ion density spread of the 610 at a different input powers (at 2.45 GHz) as pressure is varied. The working gas is argon, and the source is tuned such that about 95 % to 98 % of the incident power is absorbed into the plasma. A double Langmuir probe is used to take the density data. It is seen that there are two distinct modes of operation for the 610, the high density, and the low density, as the pressure is varied. There is some evidence of hysteresis as the plasma source changes modes. Figure 4 is an ion energy distribution function of the 610, as taken by a multi-grid ion energy analyzer. The source produces low average energy ions, typically less than 40 eV, with narrow and predictable distribution functions. Thus, the density, and energy distribution functions of the plasma source can be easily controlled using pressure and power variation. The electron energy distribution functions for the 610 , taken using a single Langmuir probe, are near Maxwellian although there is some evidence of a depleted high energy tail. Langmuir probes and energy analyzer data are taken in accordance with techniques described by Hopwood [8]. A charge state distribution of the beam extracted from the 610, with the SCECR off, indicates the creation of both Ar^{1+}, and Ar^{2+} ions, the ratio being about 95:5 for the two charged species.

Figure 5 shows the cross-section of the 610 mounted on the injection box of the SCECR. A UHV compatible ceramic break electrically isolates the 610 from the SCECR. In order to accommodate the 610 on the top flange, the SCECR main stage waveguide had to be reduced to a 1/2 height waveguide, and tilted at an angle. The SCECR is excited at 6.4 GHz, while the 610 is excited at 2.45 GHz microwave frequency. The power supply for the 610 is dc isolated from the plasma source. Plasma gas is fed through the 610 gas line. The problem of balancing the difference in operation pressures of the two ion sources is somewhat overcome

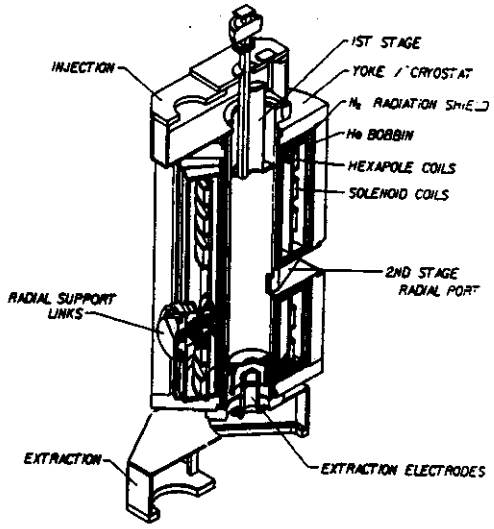

FIG. 1. The SCECR is shown in schematic form.

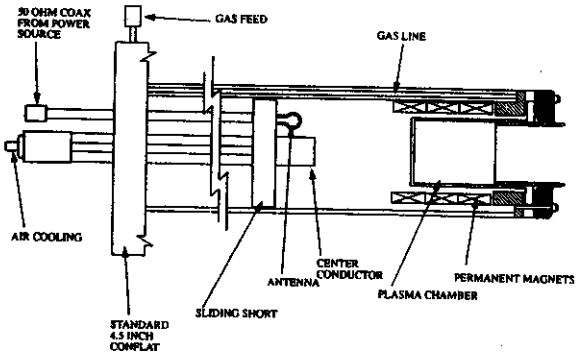

FIG. 2. Cross section of the MPDR 610.

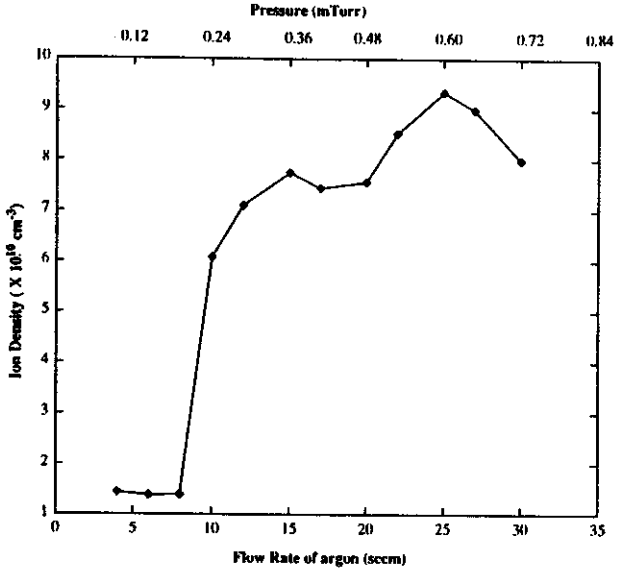

FIG. 3. Ion density vs argon gas flow/pressure at 125 W input power, 2 cm downstream from the source.

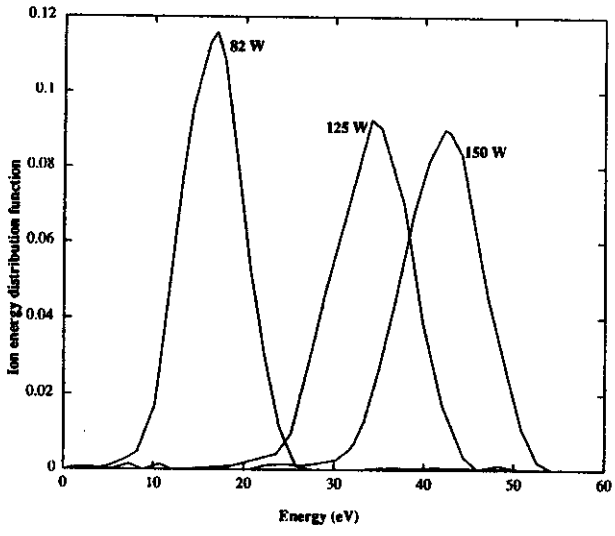

FIG. 4. Ion energy distribution functions for the 610 at 0.31 mTorr argon gas pressure, 3 cm downstream from the source.

by using a baffle with a one cm through hole at the bottom of the injection stage, and a steel plate at the output of the 610, also with a one cm hole. The 610 is then biased at a potential relative to the SCECR to extract a beam from it, and into the main stage.

Summary and Conclusions

This study has a preliminary answer to the question: what is the purpose of the first stage in an ECRIS for multiply charged ions? In Figure 6, the effect of positive, neutral or negative plasma injection from the 610 on the charge state distribution of the SCECR main stage is seen. The species ionized is oxygen. The SCECR field is set for the High-B mode. It is seen that there is a shift towards enhanced production of higher charged ions when the 610 is biased at -1 KV relative to the main stage. The purpose, then of the first stage is electron injection into the main stage. Note also, that while the absolute currents shown in figure 6 are high, it does not show a particularly good charge state distribution for the SCECR. This is because the 610+SCECR operating pressure is about one order of magnitude higher than optimal for the SCECR. Clearly, a better pressure balance between the strong operation of the 610, and a strong operation of the SCECR needs to be achieved.

It has been shown that a high pressure plasma source (the 610) can be coupled to a low pressure ECRIS for multiply charged species (the SCECR). With this hybrid source (610+SCECR), an old question may have been answered: the ECRIS plasmas require low energy electrons, and the first stages can provide them. The results of this study are very promising. Future research involves stronger coupling between the 610 and the SCECR to operate both at their respective optimal pressure conditions. Beam characteristics of the 610 using the SCECR need to be done. Also, the SCECR variable magnetic fields can be scaled down to study the effects of 2.45 GHz. microwaves for the main stage excitation.

a. Department of Electrical Engineering, Michigan State University.

References

[1] Srivastava, A.K., Dahimene, M., Grotjohn, T.A., and Asmussen, J., Rev. Sci. Instrum. 63(4), 2556, 1992.

[2] Srivastava, A.K., and Asmussen, J., J. Vac. Sci. Technol., A 11 (4), 1307, 1993

[3] Antaya, T.A., Nuclear Instrum. Methods B40/41, 1024-1027, 1989.

[4] Antaya, T.A., and Gammino, S., to be presented at this conference.

[5] Clark, D.J. et. al., 5th ECR Ion Source Workshop, Louvain la Neuve, 137, 1983.

[6] Loiseaux, J.M. and Fruneau, M., 10th Int. Conf. on Cyclotrons and Their Applications, East Lansing,

IEEE 84CH 1996-3, 188, 1984.

[7] C. Lyneis, 13th Int. Conf. on Cyclotrons and Their Applications, Vancouver 1992, to be published.

[8] Hopwood, J., Ph.D. Dissertation, Dept. of Electrical Engineering, Michigan State University, 1990.

[9] Pearton, S.J., and Hobson, W.S., J. Appl. Phys., 66(10), 5018, 1989.

[10] Zhang J., Hwang, B., Reinhard, D.K., Asmussen, J., J. Vac. Sci. Technol., A(8), 2124, 1990

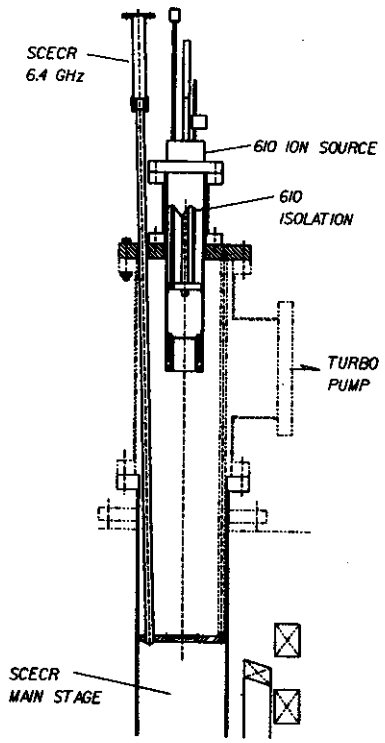

FIG. 5. Cross section of the 610 mounted on top of the SCECR.

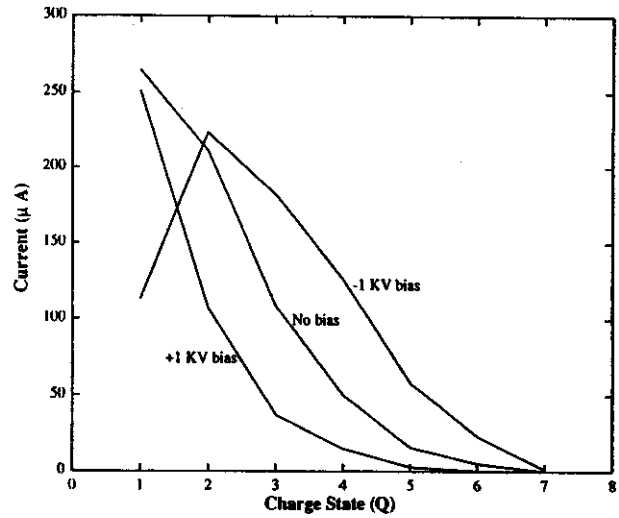

FIG. 6. Comparison of the effect of negative, positive, and neutral injection from the 610 into the main stage, on the charge state distribution of the SCECR. Ionized species is oxygen.

SCECR EMITTANCE AND BEAM FORMATION

K. A. Harrison and T. A. Antaya

1. Introduction

With the SCECR we have the ability to study the emittance as a function of the magnetic confinement fields, both radial and axial. This is possible because the SCECR has both tunable superconducting solenoid and hexapole coils[1]. From these studies we hope to understand the beam formation processes in ECR sources. We would like to make a preliminary report on our emittance measurements of the SCECR. The emittance for argon and oxygen charge states has been measured at 5, 10 and 15 kV and found to be in the range of 40 to 250 p mm-mrad. For both oxygen and argon it was observed that for low charge the emittance increases (implying the expected magnetic field dependence) and that for high charge the emittance decreases sharply, perhaps implying that the high charge state ions are being produced at a effective radius smaller than the extraction aperture.

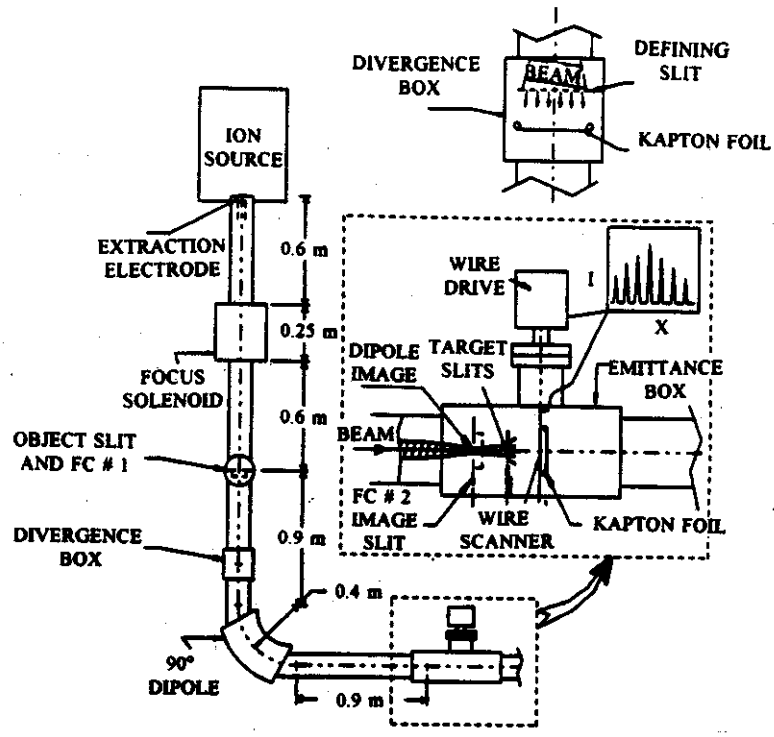

Figure 1: The SCECR Analysis Beamline and Emittance Measuring System

2. Theory

Consider an ion of charge Q and mass M extracted from an aperture of radius r_0 and accelerated through a potential V_{ext}. It can be shown[2], that the final emittance would be given by

$$e = r_0 \sqrt{\frac{T_Q}{2QV_{ext}}} + r_0^2 B_0 \sqrt{\frac{Q}{8MV_{ext}}} \qquad (1)$$

where B_0 is the magnetic field at the extraction radius. There are two simple limiting cases to this formula. If the first term dominates, then we have the *Hot Ion* limit:

$$e\mu r_0 \sqrt{\frac{T_Q}{2QV_{ext}}} \mu \frac{1}{\sqrt{Q}} \qquad (2)$$

$$e\mu r_0^2 B_0 \sqrt{\frac{Q}{8MV_{ext}}} \mu \sqrt{Q} \qquad (3)$$

If the ions are cold ($T_Q \sim 0$), and the interaction of the ions with the magnetic field in the ion source dominates, then we have the *Cold Ion* limit:

3. Technique of Measuring the Emittance

A beam incident on a slit plate will produce multiple beamlets. Using a wire scanner device (figure 1), we can determine the positions and divergence angles of different beamlets. With this information we then construct a phase space diagram of the beam and extract the phase space area A by making an ellipse fit. We then define the emittance e as

$$e_{equiv} \frac{A}{p} \qquad (4)$$

The wire scanner is a 0.4 mm diameter tungsten wire tube mounted on a horseshoe frame. The horseshoe frame is attached to a linear vacuum feedthrough, driven by a synchronous stepping motor. The slit plate is just behind the faraday cup. It is mounted on a shaft, which can be rotated in or out of the beam's path. The slit's are .25 mm wide and 4 mm apart, with the exception of the two central slits, which are 2.5 mm apart and used to reference the center of the beam relative to the center of the apparatus. As the wire moves in a plane perpendicular to the beam axis, a current profile is generated. A peak in the current profile corresponds to a beamlet from a slit. From the current profile, the edges of the beamlet, and hence the divergence angle of the beamlet, can be found.

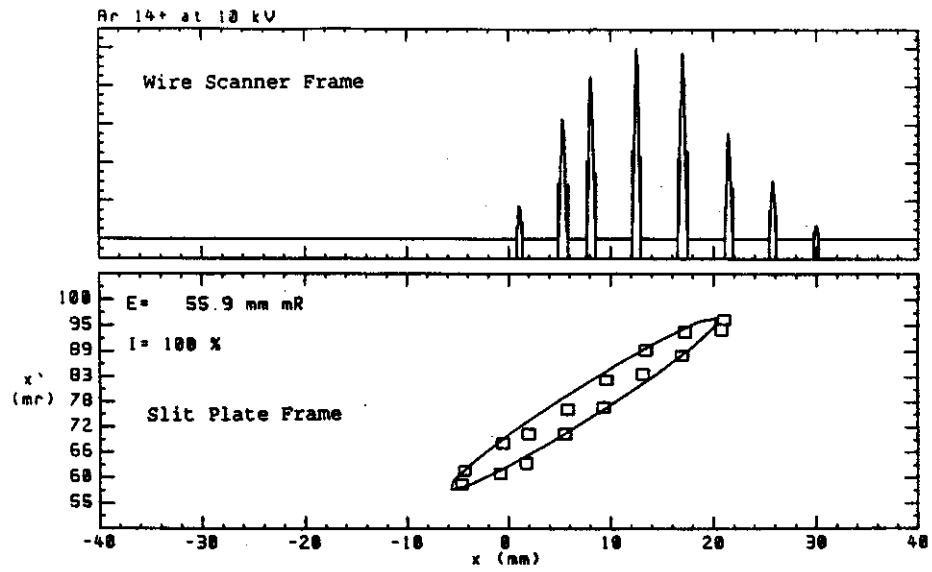

Figure 2: Raw data from the SCECR emittance system: an argon 14+ 100% intensity emittance fit, showing a uniform cross-section and a good fit to an ellipse, implying a circular beam with an abscence of aberrations.

The data acquisition system consists of a pc based A/D data acquisition card housed in a MSDOS computer. The computer samples two differential analog signal inputs, position of the scanning wire and scanning wire current. The emittance is calculated from the positions of where the current peaks go to zero (corrected for the wire diameter) to obtain a 100% current emittance. Figure 2 shows a typical scanning wire current profile and the resulting emittance ellipse fit. As can be seen, the beam profile is sharp and absent of aberrations.

4. Measurements

The measurements were made with the SCECR tuned for the production of highly charged ion species (i.e. O^{6+} or Ar^{12+}), with source parameters (MW power, pressure, etc) then held constant. With the analysis image and object slits at 17 mm x 17 mm, the beam line was tuned for maximum current at the faraday cup for each charge state measured. When ready to make the emittance measurement, the object and image slits were fully opened up to 34 mm x 34 mm. When the slits were opened there was typically less than a 25% increase in the transmitted beam current observed, with little or no current left on the slits.

The 100% emittances for oxygen 1-8+ extracted at 10 kV are shown in Figure 3. Measured emittances were in the range of 40 to 250 mm-mrad. Figure 3 also shows for these ions the normalized emittances. For both the normalized and unnormalized cases, we find that the emittance increases with low Q, but decreases sharply for Q>4+.

The measured emittance for argon 6-14+ at 10 kV extraction voltage are shown in Figure 4. Not all charge states for argon were measured because of device sensitivity and overlap of charge states of oxygen and argon. Measured emittances range from 50 to 175 mm-mrad were measured. Again, the normalized and unnormalized emittance increases with low Q ions and decreases for high Q ions.

For a given charge state, this data can be analyzed to yield emittance vs. intensity, as shown in figure 5 for O^{3+}. The emittance varies smoothly with increasing intensity- aberrations do not contribute significantly to the measured emittance.

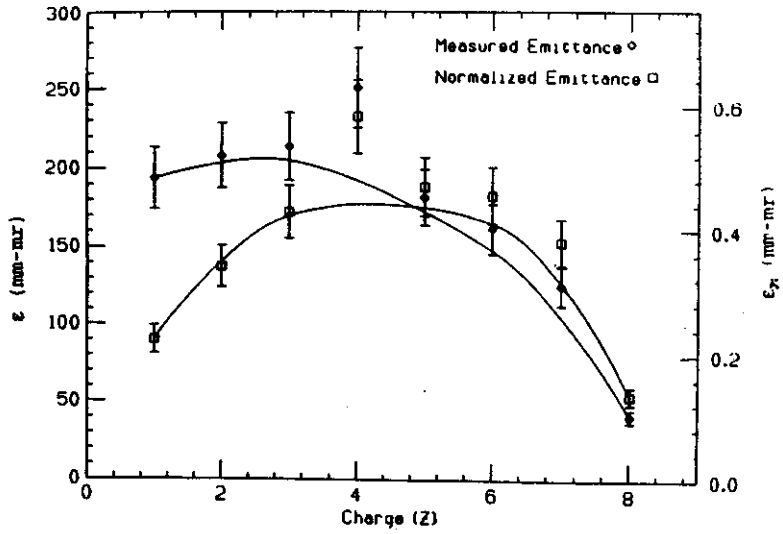

Figure 3: 100% emittances for oxygen 1-8+ extracted at 10 kV.

5. Summary

These initial emittance measurements showed:

1. Clear measurements of the 100% total extracted current emittance at 10 kV were made as a function of charge, for oxygen and argon ions.
2. Aberration free beam envelope intensity profiles with relatively sharp edges were observed in all cases.

There were no high divergence tails observed, as had been reported previously in other measurements[3,4].
3. The emittance for a large range of charge states for oxygen and argon was measured and similar trends for e vs. Q were observed. For low Q, the emittance increases, implying a magnetic field dependence, but for high Q, the emittance decreases. One possible explanation is that the high charge state ions are being produced at an effective smaller radius than the extraction aperture.

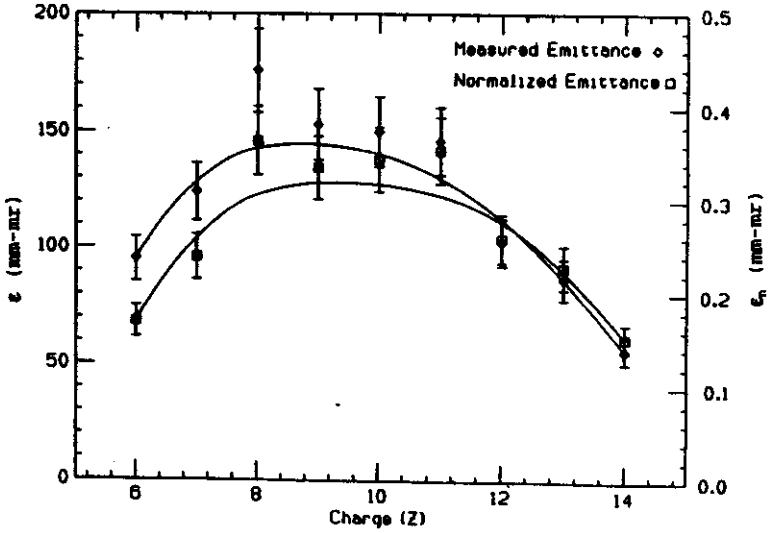

Figure 4. 100% emittances for argon 6-14+ extracted at 10 kV.

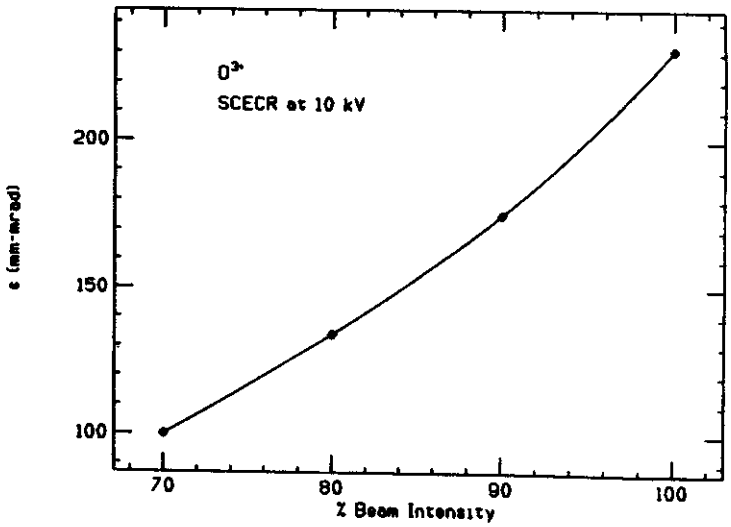

Figure 5: The emittance for oxygen 3+ as a function of intensity.

References

1. Antaya, T. A., 9th International Workshop on ECR Ion Sources, Les Edition des Physique 50, Grenoble France, 707, (1988)
2. Xie, Z. Q., PhD thesis, MSUCP-60, (1989)
3. Clark, D. J., International Conference on ECR Ion Sources and Their Applications, MSUCP-47, 433, (1987)
4. Antaya, T. A., International Workshop on Nonlinear Problems in Accelerator Physics, Berlin, (1992), to be published.

THE SCECR 6.4 GHz HIGH B MODE AND FREQUENCY SCALING IN ECR ION SOURCES

T.A. Antaya and S. Gammino[a]

SCECR 6.4 GHz High B Mode

Since the presentation of the first results of the Grenoble 16.6 GHz ECRIS (Electron Cyclotron Resonance Ion Source) at the Berkeley ECRIS Workshop in 1984 [1], the possibility of $n_e \propto f^2$ frequency scaling has been one of the major driving forces of ECRIS designs for highly charged ions. Several higher frequency sources have been built and they do indeed have very high performance: the 14 GHz ECRIS ICIS at Jülich [2], AECR at LBL [3], ECR4 of Ganil [4] and the 18 GHz Minimafios of Grenoble [5]. Two of these sources, AECR and ECR4, have operated at lower frequency as well with poor results. On the other hand, there is Caprice 2B of Grenoble [6], a 10 GHz source with essentially equivalent performance. There are also very high density singly-charged sources , like the Chalk River ECRIS [7], operating at 2.45 GHz. Given these conflicting results, do we need to raise the frequency to get higher performance, and if so, is this really a signature of the $n_e \propto f^2$ density cut off limit?

In order to help resolve this issue, we built a developmental source, the SCECR, at NSCL. The SCECR was designed to permit the frequency opertion scaling in a single geometry by using a full superconducting coil set to scale the magnetic topology from 5-35 GHz. [8] At the lower end of this frequency range, the wide magnetic range would also permit the study of new regimes of magnetic confinement, like that exhibited in Caprice 2B-type ECRIS. In addition, the SCECR design parameters were based on the optimized RTECR at NSCL[9], so the starting point would be a well known performance. Hence, in one geometry, both frequency scaling and magnetic confinement scaling could be studied, with no instrumental bias toward either mode of operation.

The initial results with the SCECR are that it matches or exceeds the performance (peak charge states and/or intensity), of nearly all other existing ECRIS, but at the low operating frequency of 6.4 GHz. In addition, the SCECR is stable, reproduceable, and has a very high ionization efficiency ($\geq$ 80%). These results have been obtained by raising both the axial and radial magnetic confinement substantially above the design values, while maintaining a normal 6.4 GHz ECRH resonance zone. The frequency scaling argument, while not invalidated by these results, is now much less clear. While at the same time, these results open up the new possibility of high performance, low frequency sources.

The SCECR is shown schematically in Fig. 1. There are five superconducting solenoid coils, clustered 2 and 3, to produce two axial mirrors. These mirrors are split to permit fine mirror ratio adjustment. (This subdivision has in fact allowed the field configuration responsible for the results to be reported here.) The superconducting hexapole resides in the bore of the tandem mirror. The plasma chamber, microwave injection and beam extraction systems are the same as the RTECR. The plasma chamber bore is 14 cm, and the axial mirror-to-mirror length is 50 cm. The field design that follows that of the " 2 mirror " operating configuration of the RTECR. Table 1 summarizes the characteristics of these two magnetic configurations. Figure 2 compares the performance of the SCECR for the optimized field to that of the RTECR for krypton ion production. As can be seen in Fig. 2, there is a large improvement in the performance of the SCECR over that of the RTECR. Yet the SCECR is operating at the same frequency

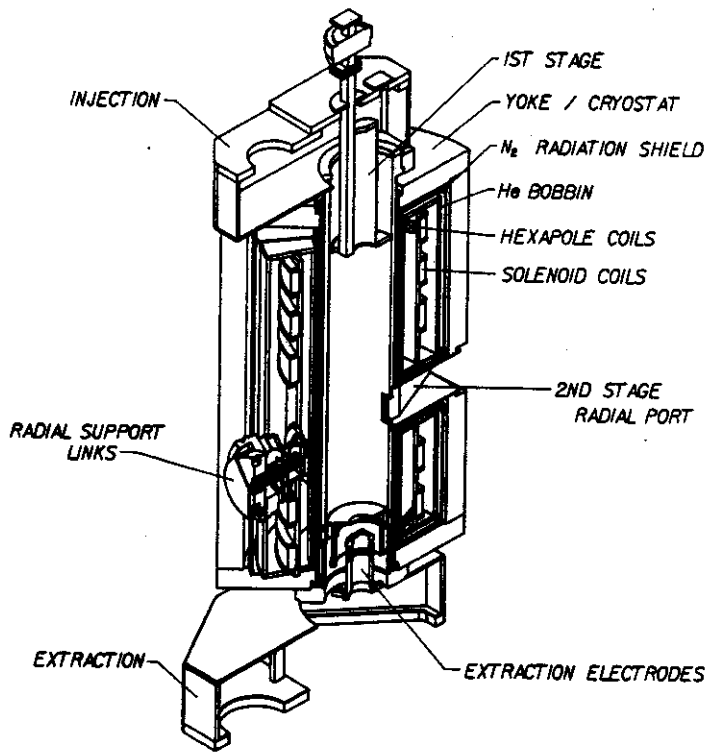

Figure 1: The SCECR is shown in schematic form.

as the RTECR, but with higher peak fields, mirror ratios and a larger confined plasma volume. These differences are summarized in Table 1.

The Classical Frequency Scaling Argument

Since field resonant microwave heating of electrons is the plasma drive in ECRIS, microwave transmission into the plasma is essential under all operating conditions. Assuming a collisionless, non-dielectric and non-magnet plasma (!!!), one can show that there is a maximum allowed plasma density for the propagation of a given electromagnetic wave (of frequency ω_{ECR}) into the plasma:

$$n_{e,max} = \frac{m_e}{4\pi e^2}\omega_{ecr}^2 \tag{1}$$

This relation serves as the basis for the supposed frequency scaling in ECR sources, in the following way. Consider the step-wise ionization of species X from charge state i+ to charge state (i+1)+; thru successive electron impact ionization:

$$X^{i+} + e \rightarrow 2e + X^{(i+1)+} \tag{2}$$

If $\sigma_{i,i+1}(E_e)$ is the cross-section for this reaction, and τ_c is the average ion confinement time in the plasma, one can show that for this step to occur, then:

$$n_e\tau_c \geq < \sigma_{i,i+1}(E_e)v_e >_{v_e}^{-1} \tag{3}$$

That is, the product $n_e\tau_c$ must be greater than a characteristic rate for the atomic process driving the reaction. All other factors being equal, raising the plasma density raises the maximum charge state that

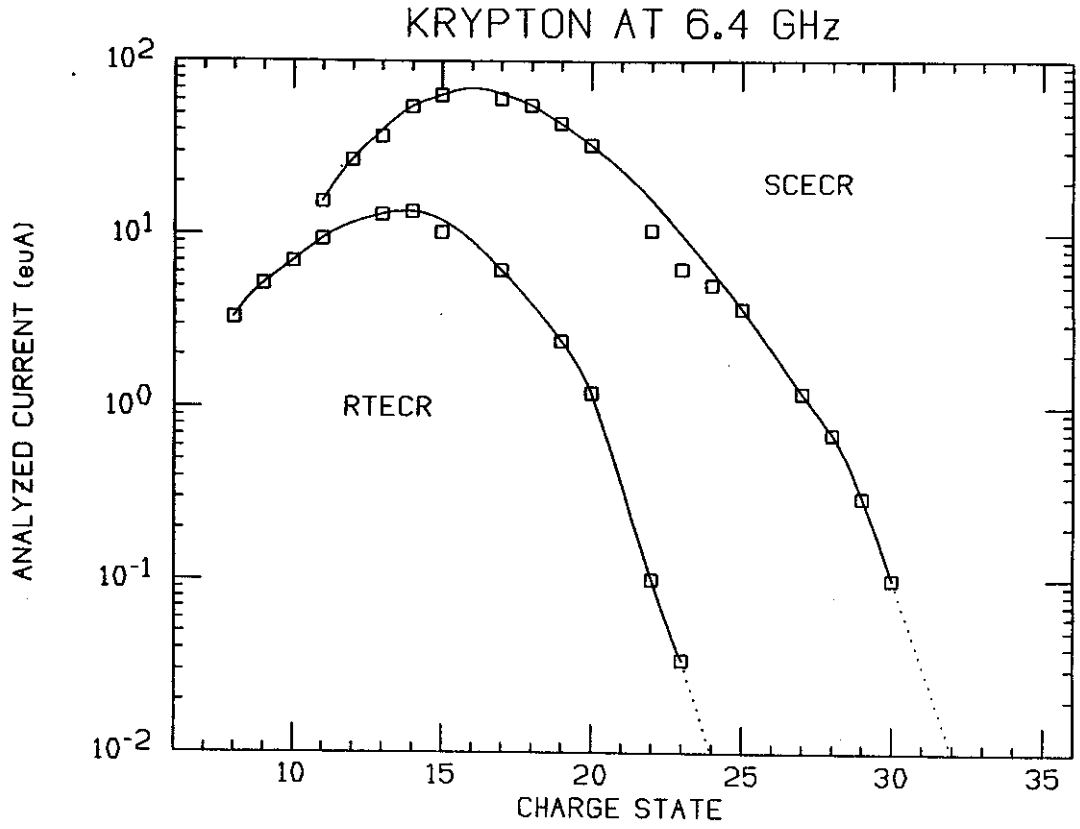

Figure 2: A comparison between the RTECR and SCECR for krypton ion production– both sources are operating at 6.4GHz.

can be produced in an ECR plasma. Since the maximum plasma density $n_e \propto f^2$ by Eq.(6), it follows that raising the ECR frequency is an obvious way to scale up the performance of these ion sources.

Comparison with Higher Frequency Sources

Table 2 makes a comparison between several sources for oxygen and argon ion production. (Limited published data on the dc performance of the 18 GHz Minimafios make it impossible to include this source in comparisons for all species.) As can be seen, the SCECR High B results fit reasonably well into the performance interval of these other sources. That is, there is no evidence that they have substantially higher ion production rates or higher extracted currents, which would be the signature for the frequency scaling effect.

One issue that is often not addressed in comparing source performance is ion source brightness, and we try to address this in Table 2. The total extracted current should scale as:

$$I \propto V^{3/2} a^2 \tag{4}$$

where V is the source bias voltage and a is the diameter of the extraction aperature. (We assume that the extraction gap has been chosen to match the space charge.) Using $V = 10kV$ and $a = 8mm$, the standard extraction parameters of the SCECR, sources with higher voltage or larger extraction areas would be expected to have enhanced extracted current, and this is indicated by the enhancement factor, the last entry in Table 2. The RTECR, SCECR, ICIS and AECR all have the same extraction parameters, and so can be directly compared, while one would expect that the extracted current of the others is enhanced by

	6.4 GHz Design	6.4 GHz Optimized
Injection Mirror Ratio	3	7.2
Extraction Mirror Ratio	2	3.8
Wall Mirror Ratio	1.7	2.9
Mirror peak-to-peak Separation	0.52m	0.65m
Confined Plasma Volume	8L	10L

Table 1: A comparison of design (quasi-RTECR) vs. optimal magnetic field parameters of the SCECR for operation at 6.4 GHz

the extraction parameters and should be scaled by 1/(enhancement). Compared this way, the SCECR and AECR have the highest performance of all ECRIS, but these two sources differ in frequency by a factor of 2.27, or in cut off density according to Eq. (1), by a factor of 5.

A Possible Correct Interpretation of ECRIS Performance

As seen in Figure 2, the performance of the SCECR at 6.4 GHz greatly exceeds that of the RTECR. Yet both sources have the same plasma hardware and the same operating frequency. In fact, peak operating fields of the SCECR are similar to those of the high frequency sources, and this is a clue to why the SCECR performance is higher. The condition for a quiet plasma in a magnetic trap is:

$$\beta = P_{particle}/P_{magnetic} \ll 1 \tag{5}$$

where $P_{particle}$ is the pressure related to the momentum of the particles in the trap. Since it is true that, when comparing temperatures, $T_e \gg T_i, T_o$ in ECRIS plasmas, and the neutral density n_o must satisfy $n_o \ll n_i$ to produce highly charged ions, then the condition expressed in Eq.(11) can be reduced to a condition relating the electron temperature and plasma density to the magnetic pressure,

$$\sum N_e k T_e \ll B^2/2\mu o \tag{6}$$

for a stable, well confined, quiescent plasma. From Eq.(12), one can argue that the one must raise the magnetic field to raise the density. Since the first harmonic resonance is used to heat the electrons in an ECRIS, then raising the field would require raising the frequency (if the minimum field is raised too high). Also, if it is possible to raise the magnetic confinement without raising the frequency, i.e. the SCECR High-B mode, then the same performance gain should be possible at low frequency.

Summary and Conclusions

Our preliminary conclusion is that the performance scaling of ECRIS with increasing frequency is an effect of the increase in magnetic confinement of the plasma. This permits higher n_e and T_e, both of which will result in higher source performance, but enhancing the ion production rate for highly charged ions. There is no evidence at present for the $n_e \propto f^2$ frequency scaling, as one of the highest performance sources, the SCECR, has a low operating frequency relative to other ECRIS. As was shown, the frequency

	RTECR	SCECR	SCECR	RIKEN [1]	CAPRICE [2]	JULICH [3]	GANIL [4]	AECR [5]	AECR	MINIMAFIOS [6]
	6.4 GHZ	6.4 GHZ	6.4 GHZ	10 GHZ	10 GHZ	14.4 GHZ	ECR4	14GHZ	14GHZ	18 GHZ
		low field	high field	biased disk	2 omega	supercon.	high field	no E-gun	E-gun	
O 6+	52	90	840	150	400	135	*	170	475	800
O 7+	12.2	25	185	60	47	50	*	51	131	180
O 8+	1	4	18	6	3	6	*	6	13	*
Ar 11+	12.1	13	170	100	60	30	80	44.5	141	140
Ar 12+	8.1	8	107	40	30	23	36	22.6	78	80
Ar 13+	3.8	5.2	56	15	12	13	13	9.8	34	45
Ar 14+	1.4	1.4	30	8	4	6.3	5	4	17	20
Ar 16+	0.1	0.1	2.1	1	0.3	0.8	0.5	0.28	1.4	1.4
Extr. Aper.	8 mm	8 mm	8mm	10mm	10mm	8mm	6mm	8mm	8mm	8mm
Extr. Volt.	10 KV	10 KV	10 KV	10 KV	20 KV	10 KV	15 KV	10 KV	10 KV	15 KV
Enhancement	1	1	1	1.25	3.53	1	1.38	1	1	1.84

[1] T. Nakagawa, et.al., Proc. of the 11th Int. Workshop on Electron Cyclotron Resonance Ion Sources (ECRIS 11), Groningen, The Netherlands (1993) 208.

[2] G. Melin, et.al., Proc. of the 11th Int. Workshop on Electron Cyclotron Resonance Ion Sources (ECRIS 11), Groningen, The Netherlands (1993) 91.

[3] H. Beuscher, Proc. of the Int. Conf. on the Physics of Multiply Charged Ions and Int. Workshop on ECR Ion Sources, Grenoble, France, les editions de physique 50 (1989) 883.

[4] P. Sortais, et.al., Proc. of the 10th Int. Workshop on ECR Ion Sources, Oak Ridge, Tennessee, CONF-9011136 (1991) 35.

[5] C.M. Lyneis, et.al., Proc. of the 10th Int. Workshop on ECR Ion Sources, Oak Ridge, Tennessee, CONF-9011136 (1991) 47.

[6] C. Barue, et.al., Proc. of the 4th Int. Conf. on Ion Sources, Benshiem, Germany, CONF-910943 (1992) 2844.

Table 2: Several sources are compared for high charge state oxygen and argon ions. An effort is made to estimate brightness: sources with a lower 'Enhancement Factor' have higher brightness.

scaling argument starts from the assumptions of a collisionless, non-magnetic plasma, and therefore may be inappropriate as a scaling argument for the type of plasma found in an ECRIS for highly charged ions.

On the other hand, the magnetic field required in the SCECR to obtain such high performance at 6.4 GHz is not so high that it would not be possible with conventional magnetic technology, using a suitable coil design, though it would have been difficult to achieve in any presently existing conventional ECRIS. Since the cost and difficulty of microwave generators increases dramatically with increasing frequency, this High-B mode operation represents an important new low frequency ECRIS concept, and we expect that some groups will attempt to extend these results to a conventional magnet based ECRIS. At the same time, it is clear that higher frequency operation with a scaling of the High-B mode topology is likely to lead to further significant increases in performance. There are at present two efforts to further explore this regime. The next step in the SCECR program will be to extend these results to 14.5 GHz. To accomplish this, the field of the source must be raised substantially higher than the present operating level.

a. INFN-Laboratorio Nazionale del Sud, VI A. Doria (ang. V.S. Sofia), 95123 Catania, Italy.

References

1. R. Geller, et.al., Workshop on the Sixth International ECR Ion Source, Berkeley, Californai (1985).
2. H. Beuscher, Proc. of the Int. Conf. on the Physics of Multiply Charged Ions and Int. Workshop on ECR Ion Sources, Grenoble, France, les editions de physique 50 (1989).
3. C.M. Lyneis, et.al., Proc. of the 10th Int. Workshop on ECR Ion Sources, Oak Ridge, Tennessee, CONF-9011136 (1991).
4. P. Sortais, et.al., Proc. of the 10th Int. Workshop on ECR Ion Sources, Oak Ridge, Tennessee, CONF-9011136 (1991).
5. C. Barue, et.al., Proc. of the 4th Int. Conf. on Ion Sources, Benshiem, Germany, CONF-910943 (1992).
6. G. Melin, et.al., Proc. of the 11th Int. Workshop on Electron Cyclotron Resonance Ion Sources (ECRIS 11), Groningen, The Netherlands (1993).
7. T. Taylor, Proc. of the 4th Int. Conf. on Ion Sources, Benshiem, Germany, CONF-910943 (1992).
8. T.A. Antaya, Proc. of the Int. Conf. on the Physics of Multiply Charged Ions and Int. Workshop on ECR Ion Sources, Grenoble France, les editions de physique 50 (1989).
9. T.A. Antaya, 7th Workshop on ECR Ion Sources, Jülich, Germany, Jül-Conf-57 (1986).

INITIAL OPERATING TESTS OF THE 8 TESLA MAGNET

Jong-Won Kim

The 8 tesla superconducting cyclotron magnet, designed as a multipurpose test stand [1], was fully assembled in October 1993, and has been tested. Properties of the magnet measured during the initial tests and some notable events are described in this report.

I. Quench accident and its effect on magnet operation

After the magnet was fully assembled and its cryogenic lines connected, the magnet was cooled down to 4 K and then tested. All instruments seemed to be working, so the tests concentrated on operating the coils at currents as high as possible.

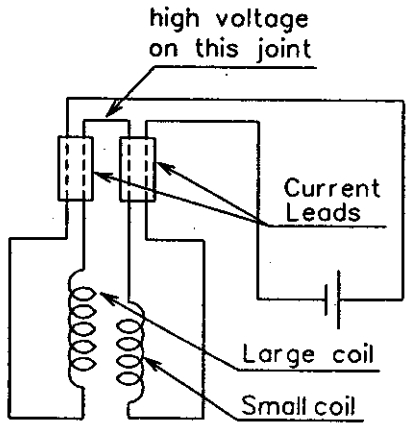

Fig. 1: A circuit diagram of the coils before the quench accident. The large coil and small coil pairs are connected in series.

During the initial operation, the large and small coil pairs were connected in series as shown in Fig. 1. This scheme originated from the idea that by ramping both coils at the same rate, the coils could be tested without being affected by heat generated from relative sliding motion between the small and large coils. However, this connection led to a problem because we failed to consider the quench voltage. When only one of the small or large coil pairs quenches and the other pair stays in the superconducting state, a large voltage is induced at the connection joint between the two coil pairs as noted in Fig.1; this is a worst case scenario with the highest voltage induced. This situation was roughly simulated using the program QUENCH [2], and the voltage estimate is about 500 V after one second. This voltage is much lower than the estimated 2.2 kV at the joint between the pair of large coils [3] during a quench. However, the midplane connection is well insulated with Teflon sleeves, Kapton tape, and G-10 plates to sustain over 2 kV, while the current lead is not designed for any high voltage.

Many instruments listed in Table 1 were damaged due to the energy discharge through poor insulation during the quench. In addition, the large coil now has a short between the lead pair, and between the lead and ground.

Table 1 : Instruments damaged and surviving during the accident

Instruments damaged	Instruments surviving
LHe level sensor (1X)	LHe level sensor (1X)
Temp. sensor (1X)	Temp. sensor (1X)
All lead voltage taps	
All strain gages	

A short in the large coil is critical to magnet operation, and at first it was thought that the large coil needed to be repaired. However, it was soon found that the large coil could be excited with the presence of the short. The short resistance increased to a few ohms from less than 1 ohm after another operation, indicating that the short is relatively weak.

Because of the voltage tap losses on the current leads, the coils have to be operated without monitoring the IR drops on the leads. The liquid helium flow to the leads was kept very high to

ensure no influence from the current leads on the coil tests, resulting in freezing the leads with ice balls. In fact, the relationship between the current lead flow and voltage drop had been measured when the lead was tested in the 50 liter liquid helium vessel, and is given in Table 2, but was not used in the initial magnet tests. Due to the excessive lead flows, the plastic flow meters connected to the leads were frozen, and cracks were developed after a series of thermal cycles. Experiments have been planned to find the proper flow.

Table 2 : Current leads test

Current	100 A	200 A	300 A	400 A	440 A
He flow (SCFH)	14	14	15	18	19
IR drop (mV)	10	22	36	59	83

* He gas flow is the sum of a flow meter pair.

II. Helium leak

After operating the magnet for about a week, a helium leak into the insulation vacuum was detected. It was noticed because of an enormous increase in heat leak; LHe loss became more than 100 l/hr after 2-3 hours without pumping the cryostat chamber. With continous pumping, the helium loss was reduced to 18 l/hr, which barely allowed continuous operation of the magnet with the supply of LHe from the 500 liter dewar connected to CTI 1400 refrigerator with a production rate of 20 l/hr. When the magnet was warmed to room temperature after the initial tests, suspicious Cajon fitting joints in the helium supply/return lines were re-tightened, and the helium leak disappeared.

III. Coil stress measurements

Bonded resistance strain gages were used to measure the coil stresses due to electromagnetic forces. They were attached on the clam shell structure which surrounds the stainless steel wire banding; the clam shell is composed of three solid stainless steel segments with a thickness of 0.6 cm. Our plan was to use the measured stresses on the shell structure, and STANSOL calculations to deduce the coil stress distributions [4].

The first measurement was made on the clam shell of the large coil. The strain reading was almost a constant until the current was ramped to 200 A. When the current was increased to 300 A, the hoop stress on the clam shell increased by roughly 1200 psi. This stress increase is much lower than 5100 psi from the STANSOL calculation in which a complete contact with the banding is assumed. If the contact is loose, the clam shell would be subjected to much lower pressure, as the measurement implies. The STANSOL calculations and measurents are compared as a function of current in Fig. 2.

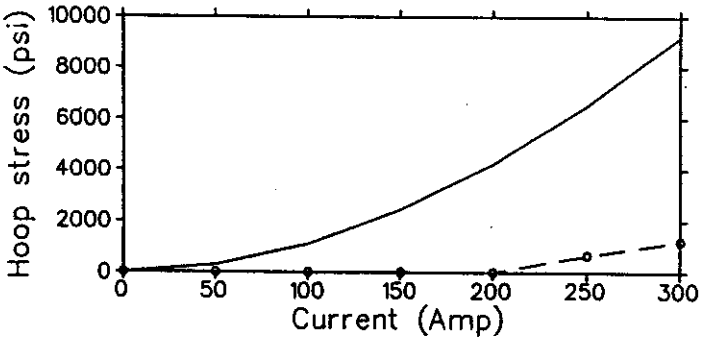

Fig. 2: The hoop stress on the clam shell structure. The solid line is the STANSOL calculation, and the dashed line with circles is the measurements with a strain gage

Since the lead wires of all strain gages were damaged during the accident described in section II, coil stress data beyond that described here could not be obtained.

IV. Quench characteristics

The magnet quenched several times before it was operated near the design currents

(I = 400A). After the quench accident described in section I occured, the small and large coils were independently connected to the two power supplies (Dynapower 500 A/20 V). In the beginning, however, both coils were excited at a similar rate to conform the idea in section I, quenching the magnet repeatedly at currents lower than 300 A as the table in Fig. 3 shows.

To determine which coil initiated the quench, the large coil pair alone was then excited (the small coil pair alone can not be excited without energizing the large coil pair because of the magnetic forces directed away from the median plane). The large coil quenched at 470 A at 4.4 K, which was a much higher current than before; the ratio of operating current to the critical current is approximately is 81% (8.0 tesla on the conductor with 470 A at 4.4 K, while the critical current is 660 A at 8.0 tesla, 4.2 K given by Supercon Inc.).

The next trial was to ramp the small coil with the large coil current maintained at 400 A. The small coil could be operated over 300 A with this method, i.e. in the background magnetic field from the large coil. The background field seemed to produce the large clamping force which suppressed wire motions in the small coil. This particular current ramping path was realized to be a way to reach close to the design currents. The maximum currents at which the magnet was operated were 370 A and 420 A for the small and large coils, respectively, at which the ratio of the operating current and the short sample critical current is 74 %.

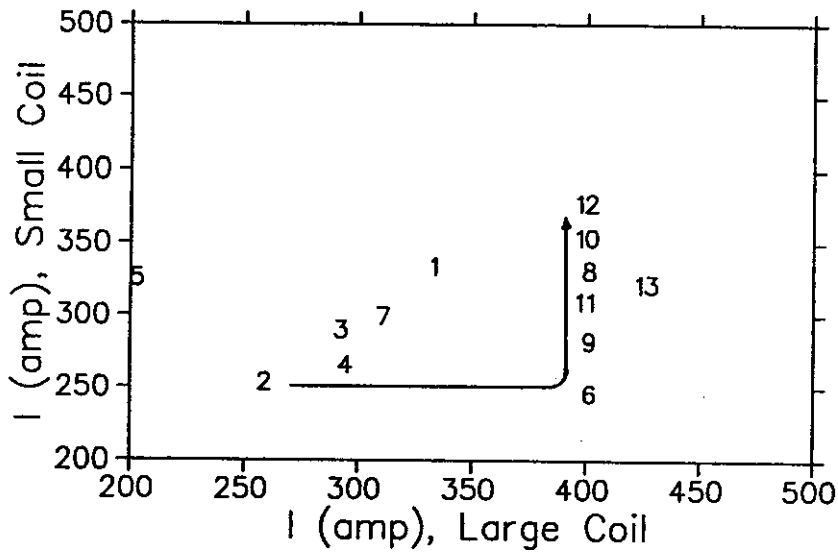

Quench #	Current ramping procedure before a quench
1-3	same rate for both coils (serially connected)
4	similar rate for both coils, large coil to 293 A and small coil to 270 A
5	1)both coils to 208 A, 2)small coil to 323 A
6	1)large coils to 400 A, 2)small coil to 250 A
7	1)both coils to 250 A, 2)small coil to 300 A, 3)large coil to 310 A
8	1)both coils to 250 A, 2)large coil to 400 A, 3)small coil to 330 A
9	1)both coils to 240 A, 2)large coil to 400 A, 3)small coil to 285 A
10	1)both coils to 240 A, 2)large coil to 400 A, 3)small coil to 352 A
11	1)both coils to 240 A, 2)large coil to 400 A, 3)small coil to 310 A
12	4.2 K, 1)both coils to 240 A, 2)large coil to 400 A, 3)small coil to 375 A
13	1)both coils to 240 A, 2)large coil to 420 A, 3)small coil to 325 A

Fig. 3: The quench history of the 8 tesla magnet displayed as a time sequence. The current ramping procedures of individual quenches are described in table. A particular current ramping path to reach higher currents is shown by an arrow in the figure.

V. Conclusion

The initial magnet tests were aimed at understanding the magnet properties and at achieving magnetic fields that were as high as possible. The highest field was 8.2 tesla in the magnet gap at 4.4 K, when the currents were 370 A and 420 A for the large and small coils, respectively.

The quench characteristics of the magnet, which is an important factor to assess the 8 tesla coil performance, were studied. However, basic coil properties such as the dependence on the current ramping path and the

cause of the present magnet quenches were not thoroughly understood.

Further tests are planned with better equipment such as computer data acquisition and dump resistors to quickly de-energize the magnet.

References

1. J. Kim, et al.,Construction of 8 T magnet test stand for cyclotron studies, IEEE Trans. on Applied Superconductivity, V.3, No,1, 266 (1993)
2. M. Wilson, program QUENCH, Rutherford Laboratory Report, RHEL/M151 (1968)
3. J. Kim, Ph.D. Thesis, Michigan State University
4. N.E. Johnson, Stress analysis of inhomogeneous superconducting solenoids, Adv.Cryo. Eng. V.22, 490 (1976)

INSTALLATION AND OPERATION OF THE SUPERBALL IN THE S2 VAULT

D. P. Sanderson, T. Glasmacher, J. Ottarson, U. Schroeder[a], J. Toke[a], X. Zhao[a], S. Baldwin[a] and D. Agnihotri[a]

In December of 1993, the first experiment was carried out using the University of Rochester Superball in the S2 Vault. The Superball is a large five section neutron detector with approximately 4500 gallons of liquid scintillator. During 1993, construction and installation were completed on the detector.

A 24 foot steel track was grouted to the floor of the vault with angle iron guides aligned to the beam axis. The five detector units were gently dropped onto the track. It is a tribute to the manufacturer[1] that very little adjustment was necessary to position the bore of these large welded vessels to the beam axis. Initially, the tanks were filled with water to check for deformations and leaks. Since the tanks could not be dried with a vacuum pump, the residual water was removed by pressure spraying liquid scintillator across the inner surfaces. This operation served to remove any remaining residue from the construction and welding operations. After purging for several hours with dry nitrogen, the tanks were filled with gadolinium doped liquid scintillator.[2]

With such a large volume of hazardous liquid, safety was a concern. We worked out a detailed plan with the University's Office of Radiological, Chemical, and Biological Safety and the local fire department. The detector is surrounded by a steel dam which would contain the entire volume of the largest of the detector units. The interior surfaces of the dam and floor are coated with an epoxy paint which does not dissolve when exposed to the scintillator. The worst case scenario would have been the catastrophic failure of a photomultiplier window. Such a failure would have emptied the unit within a few minutes. We feel that this scenario is covered in our precautions. During filling, two persons wore chemically resistant suits with organic vapor respirators. The presence of combustible fumes was monitored to confirm that all of the vapors were removed from the building. The safeguards prevented the scintillator vapors from being detected outside the vault during the transfer of eighty-two 55-gallon drums of liquid to the detector.

If one of the superball units must be drained for maintenance, a non-sparking diaphragm pump moves the liquid scintillator to a maintenance tank in the vault. Any leakage would be detected immediately by the combustible gas detector in the vault.

In order to mount charged particle detectors around the target, a fixed scattering chamber was fabricated. The chamber is surrounded by the tanks of the superball. A cryopump is at floor level and a turbo pump is mounted immediately ahead of the chamber on the beamline. The turbo travels with the first section of superball, so a tube compression vacuum joint separates it from the chamber. A small computer in the vault provides an interface to the laboratory's interlock control system. All cabling to the chamber enters radially along the main seam of the superball.

Once the 52 photomultiplier tubes were in place, the ball was ready to detect neutrons. Test began with a ^{252}Cf fission-neutron source. Trains of electronic pulses from the tubes contain information on neutron multiplicity and total kinetic energy. The superball delivers event by event angular information on the neutron yield. The source tests and the first beam tests using 28 MeV/nucleon ^{136}Xe proved that the instrument met design specifications.

In early 1994, the commissioning experiments will be run. We are presently designing and constructing an adaptation to install the MSU Miniball inside the Superball's internal scattering chamber.

a. The University of Rochester

References

1. Fab-Alloy, Inc., Jackson, MI.
2. National Diagnostics, Inc., Manville, NJ.

Figure 1: The University of Rochester Superball.

SUMMARY OF EXTRACTION STUDIES OF 250 MEV PROTON CONVERSION OF THE K500 CYCLOTRON

Lung-Sheng Lee and Henry Blosser

Three conceptual extraction systems are explored to work with 250 MeV protons in the K500 converted superconducting synchrocyclotron for use in cancer therapy. The goal is to study possible solutions to problems in the extraction system and to demonstrate the feasibility of such a machine.

The coil current setup in the proposed K250 proton synchrocyclotron is listed in Table 1. The extraction channels proposed here are analogous to those of the K500 cyclotron, the general features of which are extensively reported in Fabrici's paper (N.I.M. 184, 301, 1981).

In brief, the $\nu_r = 1$ excitation extraction system employs a first harmonic bump to make the orbits drift to the right asymptotes as the $\nu_r = 1$ stop band approaches. The method of regenerative deflection uses two magnetic disturbances, a regenerator (a positive gradient bump) and a peeler (falling fringe field), to produce a $\cos 2\theta$ field perturbation, and therefore induces radial oscillations with exponential increasing amplitude. As for precession extraction, a small bump is used to produce a coherent precession of the desired amplitude as the beam accelerates through the $\nu_r = 1$ resonance. As a result of this precession, post-resonance acceleration gives radial separation needed to clear the septum.

This superconducting synchrocyclotron has an output proton energy of about 250 MeV and should have an external beam current in the range of 5 to 30 nA, which marginally meets the requirements for its purpose. Some important parameters of this machine are given in Table 2.

The resonances encountered in the extraction region and their characteristics are summarized in Table 4. The width and strength of the stop band are proportional to the driving term and the energy gain per turn measures how fast the resonance is traversed. For slow resonance traversal, we expect that the amplitude gain is roughly proportional to the square of the driving force and inversely proportional to the energy gain per turn. Furthermore, our studies show that the resonance crossing will introduce beam distortions and have strong dependence on initial amplitude, field derivatives, and field imperfections. In summary, for synchroncyclotrons with their intrinsically low energy gain per turn, the beam quality is very sensitive to both the field imperfections and initial amplitudes for resonance traversal.

The Z^4 and Defiz800 codes are used to perform the orbit tracking and extraction efficiency calculations for different conditions. The assumptions were :

- A monoenergetic beam starts at E = 240 MeV.
- Initially uniform rectangular phase grids inside the projected "beam eigenellipses".
- Constant energy gain is assumed in the Z^4 calculations.

In order to see the influence of several crucial parameters (initial beam quantity, energy gain per turn, septum thickness and aperture of electrostatic deflectors) on extraction efficiency and for comparison among these three mechanisms, calculations have been done with one parameter changed in turn while keeping the others fixed. The results are summarized in Table 3. The parameters $A_i (i = r, z)$ are betatron oscillation amplitudes, B_1 the net first harmonic bump amplitude, E_1 the energy gain per turn, t the septum thickness, A the aperture of the electrostatic deflectors, Δr the turn spacing at the head of the septum for initially centered particles, ϵ_{entry} the channel entry efficiency, ϵ_{ext} the extraction efficiency, and zloss the total vertical loss in %.

Table 1: Coil current settings.

Coil	Current (ampere)
Large main coil	700
Small main coil	180
Trim coil 1	0
Trim coil 2	0
Trim coil 3	-100
Trim coil 4	-200
Trim coil 5	-300
Trim coil 6	-300
Trim coil 7	-300
Trim coil 8	-300
Trim coil 9	-200
Trim coil 10	-100
Trim coil 11	0
Trim coil 12	100
Trim coil 13	100

Table 2: Parameters of the K250 proton synchrocyclotron

		unit	Comment
Beam			
type of ions	H^+		
output energy	~ 250	MeV	
internal current	30	nA	$V_{dee} = 15kV$
internal current	60	nA	$V_{dee} = 30kV$
external current	5 - 30	nA	
Magnetic structure			
number of sectors	3		
spiral angle constant	4.407	deg/inch	
average field at extraction	3.591	tesla	
average field at center	3.314	tesla	
hill gap	2.5	inch	
valley gap	~ 22	inch	
RF system			
dee voltage	15 (30)	kV	
resonating system	2 dees coupled		
harmonic number	h=1		
synchronous phase angle	138.2	degree	$E_1 = \frac{2}{3} q \cdot V_{dee}$
acceleration time	0.53	ms	$V_{dee} = 15kV$
acceleration time	0.26	ms	$V_{dee} = 30kV$
modulation frequency	1.0	kHz	
Central region			
type of source	P.I.G.		
slit size	0.33×0.95	mm^2	
phase acceptance	20	degree	assumption
capture efficiency	0.2	%	assumption

Table 3: Summary of extraction calculations

$\nu_r = 1$ excitation extraction							$E_f \sim 243$ MeV	$E \sim 159$ kV/cm		
initial conditions										
A_r (mil)	A_z (mil)	total orbits	B_1 (g)	E_1 (keV /turn)	t (mil)	A (mm)	Δr (mil)	ϵ_{entry} (%)	ϵ_{ext} (%)	zloss (%)
30	20	1725	1.2	10	10	5	60	83.30	17.80	6.03
30	20	1725	1.7	20	10	5	58	81.68	19.36	5.45
30	20	1725	1.2	10	1	5	60	92.00	19.54	6.38
30	20	1725	1.2	10	10	10	60	88.88	32.70	8.81
50	40	3404	1.2	10	10	5	60	39.75	7.76	58.84
50	40	3404	1.7	20	10	5	58	43.95	9.75	51.59
Regenerative extraction							$E_f \sim 247$ MeV	$E \sim 96$ kV/cm		
initial conditions										
A_r (mil)	A_z (mil)	total orbits	E_1 (keV/turn)		t (mil)	A (mm)	Δr (mil)	ϵ_{entry} (%)	ϵ_{ext} (%)	zloss (%)
30	20	1748	10		10	10	105	92.30	41.77	0.00
30	20	1748	20		10	10	101	90.78	52.00	0.00
30	20	1748	10		1	10	105	99.65	42.06	0.00
30	20	1748	10		10	5	105	90.72	21.15	0.00
50	40	3255	10		10	10	105	75.42	22.09	18.04
50	40	3255	20		10	10	101	91.64	37.36	1.14
Precession extraction							$E_f \sim 249$ MeV	$E \sim 144$ kV/cm		
initial conditions										
A_r (mil)	A_z (mil)	total orbits	E_1 (keV/turn)		t (mil)	A (mm)	Δr (mil)	ϵ_{entry} (%)	ϵ_{ext} (%)	zloss (%)
30	20	1694	20		1	5	10	81.88	23.02	10.80
30	20	1694	10		1	5	5	41.44	6.26	51.12
30	20	1694	20		10	5	10	34.83	4.25	10.33
30	20	1694	20		1	10	10	82.23	31.70	10.80
50	40	3441	20		1	5	10	50.77	11.48	41.96

Table 4: Summary of resonances encountered in the extraction region.

Resonance energy and corresponding stop band width							
resonance in ext. region	$\nu_r = 1$ excitation ex. (B_1 = 1.2 g)		regenerative extraction		precession extraction		driving force b
	E (MeV)	ΔE (MeV)	E (MeV)	ΔE (MeV)	E (MeV)	ΔE (MeV)	
$\nu_z = 1/2$	240.81	0.14	240.77	0.14	240.58	0.26	dB_1/dr
$\nu_r = 2\nu_z$	241.13		241.19		241.0		field deri. & ampli.
$\nu_r = 1$	243.25	1.14	243.11	0.22	243.19	0.62	B_1
$\nu_r = 2/2$			246.8				cos2θ gradient bump
$\nu_z = 1$	249.86	0.14			249.46	0.46	B_1
$\nu_r + 2\nu_z = 3$	251.13				250.68		field deri. & ampli.

Characteristics	$\Delta A \propto f\left(\frac{b^2}{E_1}\right)$ & amplitude dependence & distortions
$\nu_z = 1/2$	causes growth of the axial amplitude
$\nu_r = 2\nu_z$	both radial and vertical amplitude growth depend on initial beam quality, on how fast the stop band is passed, and on the field shape
$\nu_r = 1$	(1)off-centre drift of beam (2)introduces beam distortions
$\nu_r = 2/2$	(1)achieved by a positive gradient bump (regenerator) and a neg. grad. bump (falling fringe field, peeler) (2)characterized by exponential growth of radial gain
$\nu_z = 1$	produces vertical loss
$\nu_r + 2\nu_z = 3$	final energy limit

The results in Table 3 are well explained by the following arguments and comments: (1) In general, the field imperfections produced by extraction devices could not be pinned down completely by a first harmonic bump with fixed phase due to the scalloping of the orbits. Therefore the field imperfections which are canceled only over a limited range at resonance radius is not enough to restore the orbits to the stable state. (2) It seems that the radial position of M1, owing to its proximity to the internal beam and its large azimuthal width, has significant influence on how successfully the field imperfections in the vicinity of $\nu_r = 1$ might be set off. (3) As the septum thickness reduces, the channel entry efficiency rises; the extraction efficiency should increase, too. (4) it is obvious that the larger the aperture of the electrostatic deflectors, the larger the acceptance of the extraction system, and the bigger the external current. (5) we may expect that the poor initial beam quality will result in low extraction efficiency due to the resonance traversal. (6) Increasing the dee voltage (usually implying larger energy gain per turn) will raise the current extracted from the ion source, enhance the space charge limit, and decrease the amplitude growth due to resonance crossing or increase the acceptance of the resonance. In general, we will end up with higher extraction efficiency and larger output current by increasing the dee voltage.

For synchroncyclotrons with their intrinsically low energy gain per turn, the precession extraction is never employed in reality. And the electric field strength, which puts a limit on the maximum aperture of electrostatic deflectors, required in the $\nu_r = 1$ resonant extraction scheme is the primary limiting factors to achieve high extraction efficiency. In conclusion, the regenerative extraction system is a promising candidate for the proposed K500 converted synchrocyclotron because it is easy to handle and gives better results than the other two methods.

The turn numbers obtained from this technique and the transportable emittances is given in table 1 in the second line.

Time evaluation

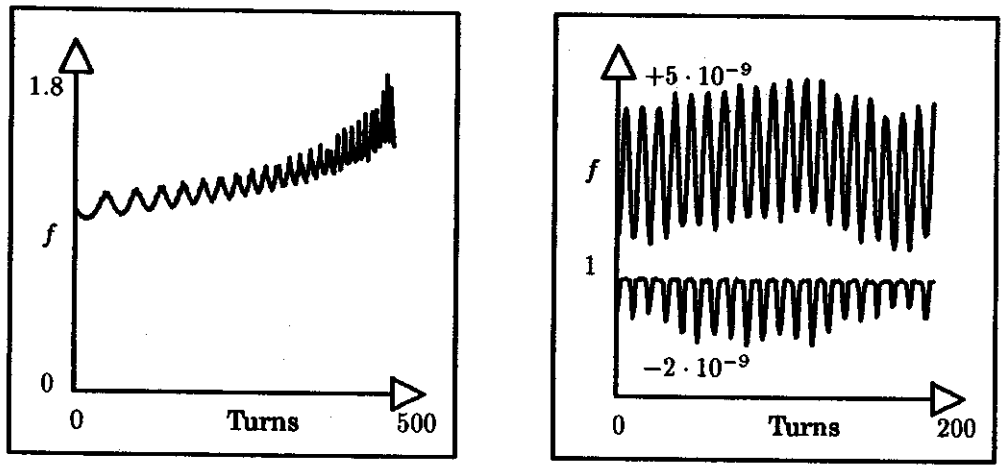

Figure 2: a: slow increase of the pseudo invariant of motion over many turns, b: periodic change of the pseudo invariant of motion after relatively few turns.

Figure 2a shows how close the pseudo invariants are to invariants of motion. Over many turns the quantity of f changes but it always oscillates around a mean which grows very slowly. The normal form method, however, bounds the growth of the pseudo invariant by considering the biggest growth that can happen in one application of the map. As demonstrated in figure 2b, the biggest growth that can be generated by N applications of the map is usually much bigger than N times the biggest growth that can happen during a single turn. Therefore it is advantageous to consider the maximum growth that can occur when the map is applied M times where M corresponds to the number of map applications that leads from one waist in figure 2b to another.

In the third line of table 1 shows the guaranteed stable turns for the desired emittances and the guaranteed stable emittances of the Indiana ring for certain optimized settings of magnet parameters and for a certain particle energy.

Parameter dependence

Since neither particle energy nor the magnet parameters are known exactly, we analyzed the dependence of stability on certain parameters. We computed the map as a function of a parameter of interest and then scanned not only through the interesting region of phase space, but also through the interval in which the parameter could lie in reality.

Table 1 shows in its fourth line the number of stable turns and the stable emittances for an energy variation of $\pm 0.3\%$, which is a typical energy spread of the beam in the Indiana ring.

The field setting of all dipoles was varied by random factors of relative strength 0.1% . The last line of the table contains the number of turns particles will at least move around the ring for any setting of the magnets in this range.

We belive that the described method gives a very reliable lower bound on the numbers of stable turns. To make completely rigorous statements about guaranteed bounds, several steps have to be

Method	turns for needed emittances	emittances for needed turns
Simplest application	15191870	0.51 πmm mrad
Divided phase space	103644000	0.82 πmm mrad
Multi–turn maps	3076246000	1.91 πmm mrad
Energy as parameter	16606040	0.08 πmm mrad
Fields as parameter	1148088000	1.42 πmm mrad

Table 1: Lower bounds on the turns of particles for initial emittance of 2π mm mrad and lower bound on the stable emittances for 3700000000 turns obtained by various variations of the normal form method. To limit the computation time, we evaluated 7^n points for n relevant phase space dimensions.

performed in a more rigorous way. Especially, it will not be sufficient to approximate the maximum of δ by scanning. Interval arithmetic methods which guarantee a global maximum have to be used [9,10]. Utilizing this guaranteed optimization is the subject of another paper [11].

References

1. N. N. Nekhoroshev, An exponential estimate of the time of stability of nearly integrable Hamiltonian Systems i. Uspekhi Mat. Nauk, 32(6): English Translation: Russian Math. Surveys 32(6) 1, 1977
2. G. Turchetti, Nekhoroshev stability estimates for symplectic maps and physical applications, Springer Proceedings in Physics 47:223, 1990
3. A. Bazzani, S. Marmi, and G. Turchetti, Nekhoroshev estimate for isochronous non resonant symplectic maps, preprint, University of Bologna
4. R. L. Warnock, R. D. Ruth, W. Gabella, and K. Ecklund, Methods of stability analysis in nonlinear mechanics, SLAC–PUB 4846, 1989
5. R. L. Warnock and R. D. Ruth, Stability of orbits in nonlinear mechanics for finite but very long times, Nonlinear Problems in Future Accelerators, W. Scandale (Ed.), World Scientific, 1991
6. R. L. Warnock and R. D. Ruth, Long–term bounds on nonlinear Hamiltonian motion, SLAC–PUB 5267, 1991
7. G. H. Hoffstätter and M. Berz, Survival times of particles in storage rings, Annual Report, NSCL/Michigan State University pp. 221-225, 1992
8. M. Berz, Differential algebraic formulation of normal form theory, M. Berz, S. Martin, and K. Ziegler (Eds.), IOP Conference Series 131:77, 1992
9. E. R. Hansen, Global optimization using interval analysis – the one–dimensional case, J. Optim. Theor. and Appl., 29(1979), 331–334
10. E. R. Hansen, Global optimization using interval analysis – the multidimensional case, Numerische Mathematik, 34(1980), 247–270
11. M. Berz and G. H. Hoffstätter, Exact bounds on the long term stability of weakly nonlinear systems applied to the design of large storage rings, Interval Computations, 1994, to appear

RIGOROUS STABILITY ESTIMATES

G. H. Hoffstätter and M. Berz

Abstract

The normal form method is used to give completely rigorous lower bounds on the number of turns which particles survive in a storage ring when the motion is described by a Taylor map. This can be achieved by computing the necessary invariants of motion with nonlinear normal form theory and performing the required global optimizations with interval arithmetic. Conventional interval arithmetic optimization turns out to be by far to inefficient for the complex optimization problems evolving from the normal form method. The concept of interval chains will be introduced which is faster by many orders of magnitude for the special functions that have to be optimized.

Introduction

The normal form method of long term estimates was used by several people in the past and is lined out in the accompanying report [1]. Nonlinear normal form theory yields pseudo invariants of motion f which are polynomials of order n^2 if the Taylor map $\vec{M}$ has order n. The deviation of being invariant under application of $\vec{M}$ is described by the deviation function δ.

$$f(\vec{M}) = f + \delta \,. \tag{1}$$

The deviation function δ has only contributions of orders higher than n. For weakly nonlinear problems and high expansion orders n, the contribution of δ is very small and due to (1), f is an approximate invariant of the map $\vec{M}$.

In the region of multidimensional phase space described by

$$\{\vec{z} | r_{min} < f(\vec{z}) < r_{max}\} \,, \tag{2}$$

the global maximum $\overline{\delta}$ of δ has to be found. It can then be guaranteed that the number of turns N_{max} which particles survive in the storage ring is certainly bigger than $N_N = (r_{max} - r_{min})/\overline{\delta}$. For the reasoning behind this statement, please refer to the literature given in [1]. Figure (1a) shows the structure of the function δ which has to be maximized for the PSR II lattice. The optimization has to be performed in a four dimensional space; we can only depict a two dimensional section.

Interval arithmetic is a means to obtain an interval $G(I)$ which contains all possible values of a function g on an interval I [2].

$$G(I) \supseteq g(I) = \{g(x) | x \in I\} \tag{3}$$

The upper bound $\overline{G}$ of the interval G is then a guaranteed upper bound of the function g on the interval I. Using interval arithmetic, the global maximum $\overline{\delta}$ can be rigorously bound to garantie the following estimate:

$$N_{max} \leq N_N \leq N_I = \frac{r_{max} - r_{min}}{\overline{\delta}} \,. \tag{4}$$

If the interval I is big, interval arithmetic tents to over–estimate $g(I)$ substantially. Therefore it is often necessary to divide the interval I into many subintervals I_i and find the maximum of all the maxima on the I_i. Figure (1a) shows the function δ on a section of four dimensional phase space. The

relevant region in phase space had to be divided into 10^{18} interval blocks in order to reduce blow–up to a useful amount. Figure (1b) shows a section of phase space on which the maximum of δ is bound by interval arithmetic on many interval blocks. The substantial interval blow–up that occurs when $\delta = f(\vec{M}) - f$ is being evaluated is due to cancellation of the contributions up to order n. Although it is known that these contributions vanish, they still cause blow–up during their computation. The deviation function δ is a polynomial of order n^2, which typically is around 100. The blow–up caused by the computations of all orders higher than n is less critical than the low order blow–up, due to the weakly nonlinear structure of the problem.

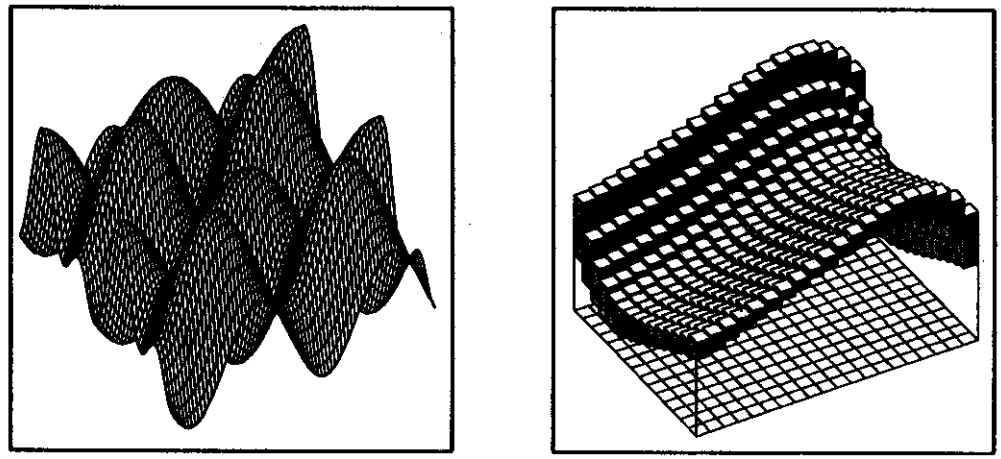

Figure 1: a: The deviation function δ. The maximum $\overline{\delta}$ of this function has to be found. In this example the function varies between $-0.5 \cdot 10^{-6}$ and $0.5 \cdot 10^{-6}$. b: δ bounded by intervals on a small part of phase space.

Maximizing the deviation function with interval chains

The concept of interval chains takes advantage of the knowledge that δ has no contributions up to order n. An interval chain I consists of a finite sequence of intervals I_i, $i \in \{0, \ldots, n+1\}$:

$$J = (J_0, J_1, J_2, \ldots, J_{n+1}) \tag{5}$$

where J_i is called the ith order of the interval chain. With a special arithmetic [3,4] one can obtain an interval chain with intervals J_i, $i \leq n$ that contain all contributions to a given polynomial of order i. J_{n+1} contains all contributions to the polynomial of orders higher than n. In the case of the polynomial δ, J_{n+1} contains all function values, whereas the lower orders of the interval chain contain all the blow–up due to low order cancellation. Thus, the bound of the function value and all blow–up due to lower order computations are strictly separated.

But even with these simplifications, the resulting objective functions have a tendency to exhibit interval blow–up because of complexity, while the bounds of the function have to be determined rather tightly in order to guarantee large numbers of stable turns.

The results in the next section were obtained by choosing 630 intervals for the examples with one degree of freedom and 1000188 for the example with two degrees of freedom. Without the concept of interval chains a realization af the described method was virtually impossible. For examples with two degrees of freedom approximately 10^{12} times more intervals would have been needed for similar results.

Order of Invariant	Interval Bounding (guaranteed)	Interval Chains (guaranteed)	Conventional Rastering (optimistic)
3	11252	743,667	849,195
4	11252	743,667	849,195
5	11306	876,059,284	982,129,435
6	11306	876,059,284	982,129,435
7	11306	432,158,877,713	636,501,641,854
8	11306	432,158,877,713	636,501,641,854

Table 1: Predictions of the number of stable turns as a function of the order of the polynomials describing the normal form transformation for the physical pendulum $d^2/dt^2\phi + \sin(\phi) = 0$ for a time step of t=1 and an amplitude of 1/10 rad. Because of energy conservation, the map is known to be permanently stable for any amplitude.

Results

Using the technique discussed in the previous section, several nonlinear systems were studied using the interval chain rastering methods to provide upper bounds for the invariant defects. In order to get a feeling for the quality of these upper bounds, the numbers were compared with approximations for the maximal invariant defects obtained by a rather tight rastering in real arithmetic. Because of the large number of local maxima, this method proved to be the most robust noninterval way to estimate the absolute maxima of the functions involved. Lower bounds on the number of stable turns obtained by conventional intervals are given in the tables 1 to 3 in order to illustrate the usefulness of interval chains. When conventional intervals were used, the deviation function was simplified as much as possible by accounting for cancellations up to second order analytically. The number of conventional intervals and the number of interval chains used in the bounding are equivalent. In all of the examples below, the choice of r_{max} is given, and r_{min} was chosen half as large.

As the first example to check the method, we used a one–dimensional physical pendulum. This is a good test case since energy conservation requires the nonlinear motion to be stable. Table 2 shows the results of the stability analysis for this case. As is to be expected, the number of stable turns predicted increases with the order and hence accuracy of the approximate invariants. While the approximate scanning method can take full advantage of this increased accuracy, the interval bounding method shows a saturation at 11306 turns. This asymptotic behavior is connected to the size of the intervals because of the unavoidable blow–up of intervals. The blow–up in third order dominates the calculation, causing the higher order improvements to not materialize. The method of interval chains takes care of all the low order cancellations and consequently the estimate is much better.

As another example, we chose the Henon map, which is a standard test case for the analysis of nonlinear motion because it exhibits almost all of the phenomena encountered in Hamiltonian nonlinear dynamics. These include stable and unstable regions, chaotic motion, and periodic elliptic fixed points. The Henon map can even serve as a very simplistic model of an accelerator under the presence of sextupoles for chromaticity correction. The results of these calculations are shown in table 3. Similar to the previous case, the number of predicted turns increases with order. In the case of interval bounding, the number of periodic turns shows asymptotic behavior limited by blow–up. Again the superiority of strict bounding with interval chains is obvious.

In the final example, we study a realistic accelerator, the Los Alamos PSR II. The same data are shown as for the two previous, more academic examples. To limit the calculation time, the intervals used

Order of Invariant	Interval Bounding (guaranteed)	Interval Chains (guaranteed)	Conventional Rastering (optimistic)
2	895	891	1,086
3	1736	9,926	11,450
4	1668	54,016	65,667
5	1674	678,725	809,612
6	1670	3,389,641	4,351,679
7	1671	42,640,927	52,474,387
8	1671	192,650,961	263,904,035

Table 2: Predictions of the number of stable turns for the Henon map at tune 0.13, strength parameter k = 1.1, and starting position of .01 as a function of the order of the polynomials in the normal form transformation.

Order of Invariant	Interval Bounding (guaranteed)	Interval Chains (guaranteed)	Conventional Rastering (optimistic)
3	179	16,137	38,385
4	179	18,197	38,857
5	173	309,356	560,309
6	173	347,312	613,135
7	171	925,531	2,184,998
8	171	1,004,387	2,248,621

Table 3: Predictions of the number of stable turns as a function of order of the approximate invariant for the Los Alamos PSR II storage ring for the motion in a phase space of 100 mm mrad.

for the optimization were 5 times as wide as the intervals used for the previous two tables.

References

1. G. H. Hoffstätter and M. Berz, Refinement of the normal form method for long term stability estimates, Annual Report, NSCL/Michigan State University, 1993
2. E. R. Hansen, Global optimization using interval analysis – the multidimensional case, Numerische Mathematik, 34(1980), 247–270
3. M. Berz and G. H. Hoffstätter, Exact bounds on the long term stability of weakly nonlinear systems applied to the design of large storage rings, Interval Computations, 1994, in print
4. M. Berz and G. H. Hoffstätter, Computation an application of Taylor polynomials with remainder bounds submitted to Interval Computations

FINITE DIFFERENCE METHOD FOR CALCULATING MAGNETIC FIELD COMPONENTS OFF THE MEDIAN PLANE USING MEDIAN PLANE DATA

Dong-o Jeon

Various orbit codes such as the Z^4 Orbit Code[1] and the Equilibrium Orbit Code[2] require evaluations of field derivatives using only discrete measured midplane field data. Taking derivatives sometimes loses significance due to the amplified noise contained in data from various sources including measurement errors and truncation errors. In order to overcome this difficulty, new finite difference schemes[3] to evaluate derivatives of data both in one-dimension and two-dimension were recently developed and tested using a magnetic field where analytical expression of the field can be derived. Some of the results are given later.

In this report, detailed description of the new schemes as differentiators will not be presented. But the basic idea is to improve the frequency responses[4] of the following differentiators by combining them with the filters in ref. [3]

$$x'_n = (x_{n+1} - x_{n-1})/2\Delta, \tag{1}$$

$$x''_n = (x_{n+1} + x_{n-1} - 2x_n)/\Delta^2, \tag{2}$$

where Δ is the step size of mesh and x_n is the functional value at the nth point. The resultant first-order and second-order differentiators are eleven-point formulas while the above ones are three-point formulas. The only difference between the differentiators in one-dimension and those in two dimension is that the partial differentiators in two-dimension provide suppression of high frequency signals in the orthogonal direction as well (refer to the "vertical filter" in ref. [3]), while taking derivatives in one direction. In order to evaluate higher order derivatives, a suitable combination of the first-order and the second-order differentiators should be chosen. The result turns out to be independent of the order of application since the differentiators are LSI (Linear Shift Invariance)[4] and FIR (Finite Impulse Response)[4] operators.

First of all, the ν_z and ν_r for a field with $q/A = 0.25$ and a nominal final energy 40 MeV/u are computed as functions of energy using the Equilibrium Orbit Code (hereafter will be called "EO Code") which uses the newly proposed differentiators (hereafter will be called "new EO Code") and compared with those obtained from the EO Code using the following differentiator in (3) (hereafter will be called "old EO Code")

$$x'_n = (x_{n+1} - x_{n-1})/2\Delta, \tag{3}$$

$$x''_n = (x_{n+2} + x_{n-2} - 2x_n)/4\Delta^2. \tag{4}$$

It should be pointed out that the EO Code uses only first order derivatives while the Z^4 Orbit Code makes use of (3,4). Figure 1 shows two different plots of ν_z obtained from the new EO Code and the old EO Code respectively. For the plots of ν_r, similar results are observed, even though they are not presented here.

As an independent test of the new differentiators, we applied them to construct off-median plane magnetic field components, which requires the evaluation of derivatives of various orders. In doing orbit calculations for cyclotrons, it is sometimes necessary to construct off-median plane field components when only a discrete median plane map of the magnetic field is given (in the case of cyclotrons, data are usually measured on a polar mesh). Assuming median plane symmetry and using a fourth-order vector potential,

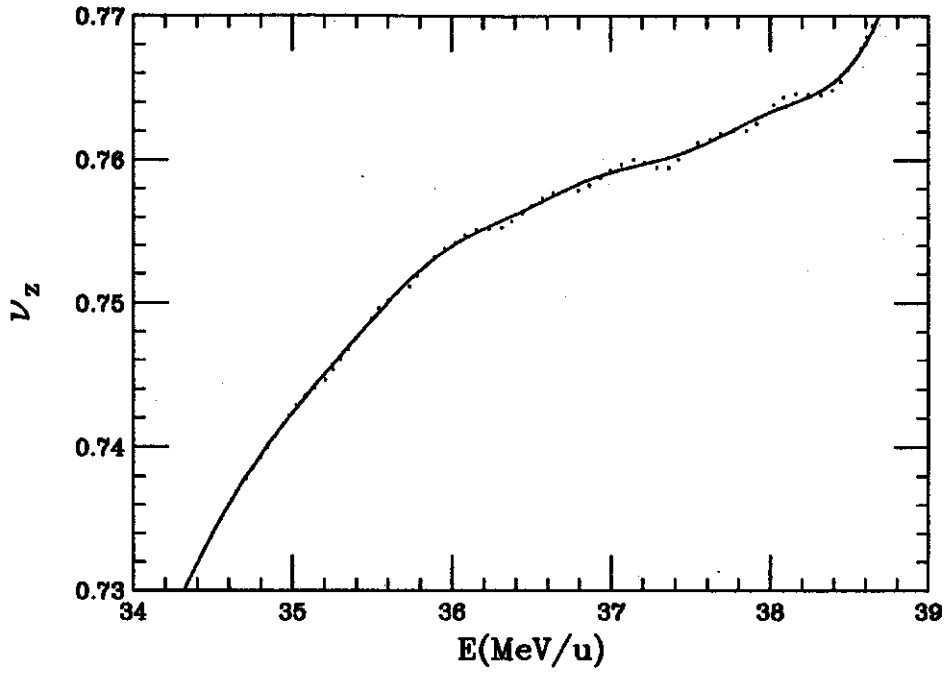

Figure 1: This shows two plots of ν_z for a magnetic field with $q/A = 0.25$ and a nominal final energy 40 MeV/u as functions of energy obtained from the two different Equilibrium Orbit Codes one of which uses new differentiators and the other uses the differentiator in (1). The ν_z plot obtained using the new differentiators is depicted in a solid line and is apparently more smooth than that derived using the differentiator in (1) depicted in a dotted line.

the components of the magnetic field off the median plane[1] are given by:

$$B_z = B(r,\theta) - \frac{z^2}{2!}\nabla_2^2 B(r,\theta) + \frac{z^4}{4!}\nabla_2^4 B(r,\theta), \tag{5}$$

$$B_r = \frac{\partial}{\partial r} C(r,\theta,z), \tag{6}$$

$$B_\theta = \frac{\partial}{r\partial\theta} C(r,\theta,z) \tag{7}$$

where B_z, B_r and B_θ are magnetic field components in cylindrical polar coordinates, and where

$$C(r,\theta,z) = zB(r,\theta) - \frac{z^3}{3!}\nabla_2^2 B(r,\theta),$$

and $B(r,\theta) = B_z(r,\theta,z=0)$, $\nabla_2^2 = \frac{\partial^2}{\partial r^2} + \frac{\partial}{r\partial r} + \frac{\partial^2}{r^2\partial\theta^2}$. Here, ∇_2^2 is the two dimensional Laplacian operator. Of course this truncated series easily can be extended to any order desired while satisfying $\nabla \cdot B = 0$.

We tested the new differentiators in ref. [3] to evaluate $\frac{z^2}{2!}\nabla_2^2 B$ and $\frac{z^4}{4!}\nabla_2^4 B$ using a magnetic field where analytical expressions for magnetic field components are available. This magnetic field is produced by two semi-infinite saturated iron bars[1,3] whose cross-section is square with the length of sides 4 cm. The gap between the two iron bars is 2 cm and the internal saturation field $B_{sat} = 21.4\ kG$. Table I shows the new differentiators perform better than the old differentiators in (3,4) when discrete midplane field data with step sizes $\Delta x = \Delta y = 0.1$ cm are used. For comparison, the second-order term and the

fourth-order term evaluated at $z = 0.5$ cm in (5) are used. $rms(D)$ is the root mean square value of the difference between the analytical term and the corresponding numerically estimated term.

Table I

	Old Differentiators	New Differentiators
Terms for comparison	$rms(D)$ (kG)	$rms(D)$ (kG)
$\nabla_2^2 B \times 0.5^2/2!$	5.34×10^{-3}	3.60×10^{-4}
$\nabla_2^4 B \times 0.5^4/4!$	3.79×10^{-3}	5.98×10^{-4}

Clearly the new differentiators are about ten times more accurate compared with the old ones, which is natural because the low frequency response of the new differentiators are better than those of the old ones.

Similar calculations are carried out using a magnetic field which is a summation of the above magnetic field and noise generated by random number generation within $\pm 1.0 \times 10^{-4}$ (kG), which is very small compared with 12.6 kG the maximum value of the field. The comparison results are listed in Table II.

Table II

	Old Differentiators	New Differentiators
Terms for comparison	$rms(D)$ (kG)	$rms(D)$ (kG)
$\nabla_2^2 B \times 0.5^2/2!$	5.40×10^{-3}	0.682×10^{-3}
$\nabla_2^4 B \times 0.5^4/4!$	4.48×10^{-3}	1.74×10^{-3}

As can be observed in Table II, the new differentiators behave better than the old ones even under the influence of noise, which is natural because the new differentiators suppress high frequency signals more effectively than the old ones.

As a conclusion of all these tests, the new differentiators prove to be more effective compared with the differentiators in (3,4). Owing to the enhanced accuracy for low frequency signals and suppression of high frequency signals of the new finite difference methods for evaluating derivatives, we were also able to design an orbit code that can take into account the effects of z^6 or z^8 terms, which is an extension of the Z^4 Orbit Code.

References

1. M. M. Gordon and V. Taivassalo, Nucl. Instr. and Meth. A 247 (1986) 423.
2. M. M. Gordon, Particle Accel. 16 (1984) 39.
3. D. Jeon, J. Comput. Phys. in press
4. J. G. Proakis and D. G. Manolakis, Introduction to Digital Signal Processing (Prentice Hall, Englewood Cliffs, New Jersey, 1989)

THE DESIGN OF A FOURTH ORDER ACHROMAT

Weishi Wan and Martin Berz

Based on a recently developed analytical theory of arbitrary order achromats it has been possible to design a fourth order achromat for the first time. According to the theory, the minimum number of conditions required for a fourth order achromat with an arbitrary forward cell are five for the first order, four for the second order and fifteen for the third and fourth orders respectively [1] [2] [3] [4]. Similar to one of our third order achromat designs, the system is a circular machine with mirror symmetry [5]. The first half is the forward cell (F), while the second half forms the reversed cell (R). An achromat is achieved after two turns. Three of the first order conditions for this system (FRFR) are to zero $(x|x)$, $(a|a)$ and $(a|\delta)$. The other two are $(y|y)$, $(b|b)$ or $(y|b)$, $(b|y)$. Since the first order layout of each cell is symmetric about its own center, which implies that $(x|x) = (a|a)$ and $(y|y) = (b|b)$, the conditions can be reduced to three if we zero $(x|x)$ and $(y|y)$ or to four if we zero $(x|x)$, $(y|b)$ and $(b|y)$. In our design, ten quadrupoles are used in each cell which give five free knobs (Figure 1). Four of them are used for cancelling the four terms above while one is left for optimizing the first order solution.

There are four sextupoles in each cell to correct second order aberrations, all of which have to be placed inside the dispersive region because all the second order aberrations left are chromatic ones. This is also true for the decapoles, but not for the octupoles. By placing the fifteen octupoles and fifteen decapoles carefully, a fourth order achromat requiring very weak multipole strengths was obtained (Table 1 and Table 2).

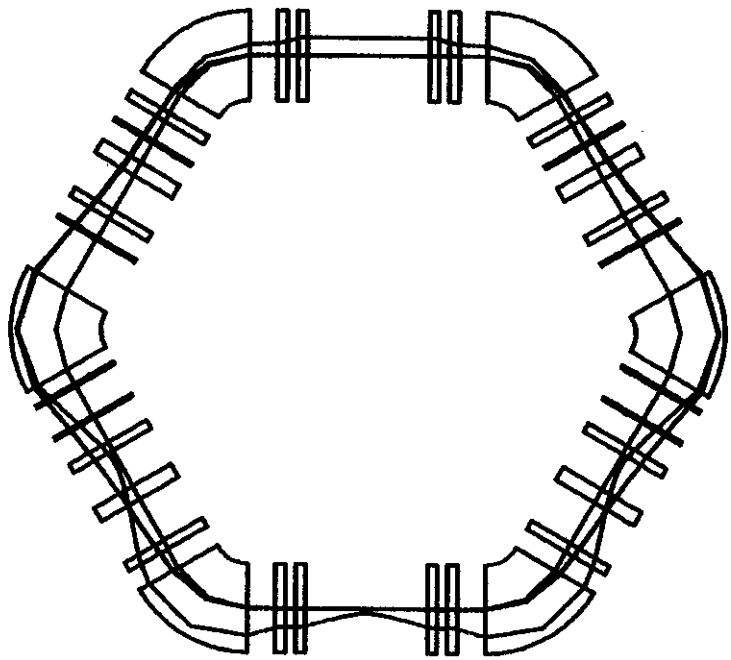

Figure 1: Layout, beam envelope and dispersive ray of the achromat. Circumference: 147.35 m; Emittance: 20π mm mrad; Dispersion: 0.6%

Strengths of the Multipoles (Aperture 10cm)			
Quadrupoles		Sextupoles	
Gradient (kG/cm)	Field (kG)	Gradient (kG/cm^2)	Field (kG)
0.277788	1.38894	-0.114852E-02	-0.287130E-01
-0.273114	-1.36557	-0.184780E-03	-0.461950E-02
0.881770E-01	0.440885	0.101651E-02	0.254127E-01
-0.282065E-01	-0.141032	-0.941644E-03	-0.235411E-01
-0.361497E-01	-0.180748		

Table 1: The field strengths of the quadrupoles and sextupoles

Strengths of the Multipoles (Aperture 10cm)			
Octupoles		Decapoles	
Gradient (kG/cm^3)	Field (kG)	Gradient (kG/cm^4)	Field (kG)
0.865187E-04	0.108148E-01	-0.184214E-03	-0.115134
-0.730041E-04	-0.912551E-02	0.993688E-04	0.621055E-01
0.118558E-03	0.148198E-01	0.267539E-03	0.167212
-0.101019E-03	-0.126274E-01	0.353274E-03	0.220796
0.474184E-04	0.592730E-02	-0.577517E-03	-0.360948
-0.663923E-05	-0.829904E-03	-0.153650E-03	-0.960314E-01
-0.132363E-04	-0.165454E-02	0.764958E-03	0.478099
0.466092E-04	0.582615E-02	-0.433794E-03	-0.271121
-0.849342E-04	-0.106168E-01	0.405756E-03	0.253597
-0.515629E-05	-0.644536E-03	-0.843814E-03	-0.527384
0.280953E-04	0.351191E-02	0.538596E-03	0.336623
0.125900E-03	0.157375E-01	0.369327E-03	0.230830
-0.423299E-03	-0.529124E-01	-0.128477E-03	-0.802978E-01
0.245393E-03	0.306741E-01	-0.177871E-03	-0.111169
0.796716E-04	0.995896E-02	0.207354E-03	0.129596

Table 2: The field strengths of the octupoles and decapoles

References

1. W. Wan and M. Berz, in preparation
2. W. Wan, E. Goldmann and M. Berz, *Proc. Comput. Accel. Phys. Conf.* (1993). AIP Conf. Proc. No. 297, p143, 1994.
3. W. Wan, E. Goldmann and M. Berz, *Proc. Int. Workshop Nonlinear Problems in Accelerator Phys.*, Berlin (1992). M. Berz, S. Martin and K. Ziegler (Eds.), IOP Conf. Series No. 131, p201, 1993.
4. E. Goldmann and M. Berz, *NSCL Annual Report* 232 (1991).
5. W. Wan and M. Berz, *Proc. 1993 Particle Accelerator Conference*, p155. *NSCL Annual Report* 210 (1992).

S800 PROGRESS REPORT

A. Zeller, B. Sherrill, S. Bricker, J. DeKamp, R. Fontus, T. Jones, C. Magsig, L. Morris, D. Pendell, P. Johnson, J. Caggiano, H. Hilbert, D. Sanderson and R. Swanson

Progress continues on several fronts on the S800 construction. A description of the beamline magnet development is given in a separate report. Prototype detector work is also described separately. All holes in the yoke steel for the first dipole have been drilled and brackets for mounting the complete dipole assembly on the carriage were attached.

The bobbin was installed into its liquid nitrogen shield and the whole assembly was cold shocked by running liquid nitrogen through the shield. During the test the coil and bobbin assembly reached 110K. After warming up, the bobbin was checked and found to be leak tight. The trim coils were installed onto the pole tip assembly and tested with current. The bobbin and nitrogen shield were then insulated and inserted into the cryostat. After all accessible welds were made, the cryostat-pole tip assembly was flipped over as one unit so the welds could be completed. The whole cryostat was then checked for leaks. The now complete assembly awaits installation onto the carriage, which will happen in early 1994.

The track was delivered, but was found to unacceptable due to many surface cracks and a nonuniform surface hardness layer. The causes were traced to improper heat treating of the central hardened zone. It was then returned to the vendor for repairs. An acceptable track was delivered at the end of the year and installed. The carriage was also completed and installed. Installation of the dipole on the carriage is underway.

Debugging of the dipole mapper continues. Additionally, preparations to analyze the map data is underway. Small test maps have been obtained which verify that the optical sensors work. The mapper will be installed after the dipole has been tested.

The iron yokes for Q1 and Q2, the large quadrupoles at the front of the spectrograph, have been ordered. Delivery is scheduled for late spring. Conductor for the quads has been delivered and end forms have been designed. Test winding of the coils will begin once sufficient beamline quadrupole coils have been wound.

The plan is to have the spectrograph operational by the end of 1995.

SUPERCONDUCTING BEAMLINE QUADRUPOLES AND DIPOLES PROGRESS

J.C. DeKamp, C.T. Magsig, L. Morris, R.T. Swanson, and A.F. Zeller

The superconducting quadrupole triplet cryostat assemblies for the beamline to the S800 spectrograph[1,2] are now in the early stages of construction. A test cryostat for the S800 beamline quadrupole magnet[3] was completed and a magnet assembly successfully tested. A spare quadrupole triplet and a spare dipole cryostat for the A1200 beamline[4] have been completed. Two quadrupole doublets, one for the A1200 upgrade[5] in February, 1994 and one for the S800 beamline were completed and tested. The S800 beamline dipoles are presently under construction.

S800 Beamline Quadrupole Magnet Testing

The magnet test cryostat was assembled with the first S800 magnet assembly inside and tested in early April, 1993. Each coil is random wound with 3300 turns of 0.5 mm dia. wire having a 3.4:1 Cu to NbTi superconductor ratio. There is 13,000 ft. of wire in each coil. Each quad on the S800 beamline will have it's field setting referenced to a cryogenic hall probe chip. As the hall probe cannot be placed in the beam area, another suitable location had to be found where there was good resolution from low field to high field. The magnet assembly was fitted with cryogenic hall probes at two locations, the first at the center of the poletip end, and the second against the side of the poletip on the axial center. A third hall chip was on a line of peak field at a radius of 2" on the axial center to use as a reference. The maximum operating current of 43A was reached with the third set of test coils which achieved a current of 44.7A after 10 quenches. End form modifications and a slightly heavier insulation (polyesteramid or formvar varnish) on the wire had helped to eliminate problems with shorted turns which were present on some of the first two sets of coils tested. Testing showed the second location, on the side of the poletip, as best for the hall chip location as shown in Figure 1. The magnet tested with the first coils from the production wire batch reached a maximum current of 48.5A, needing 4 training quenches to achieve at least 43A as shown in Figure 2. The approximate field gradient curve up to 40A is shown in Figure 3. A picture of the assembled quadrupole magnet is shown in Figure 4.

S800 Beamline Quad Triplet Cryostats

The design of the LHe vessel is complete but the shield and vacuum vessel still remain to be detailed. Progress is steadily being made and detailing should be complete by July, 1994. Parts are being ordered or manufactured as the design is completed. The LHe vessel heads have been machined for the cold bore tube and associated flange. The bore tubes for the LHe vessel, LN2 cooled heat shield, and vacuum container are in house as well as the cryogenic valves, instrumentation, and pressure reliefs. The cryomonitors have also been fabricated. All parts needed to complete the LHe vessel/ magnet assemblies and LHe vessel support should be in house by June, 1994. All the conductor for the coils was recieved by August, 1993 and coil winding is making good progress with 35 of the 60 coils needed for the 5 quad triplet magnet assemblies complete. Magnet steel machining has again started after being interrupted to work on other projects being related to the S800 spectrograph. Five of the magnet yokes and 9 poletip sets are complete. The remaining 13 yokes and 9 poletip sets are 50% complete. This includes 3 extra steel assemblies to be used for a spare triplet assembly.

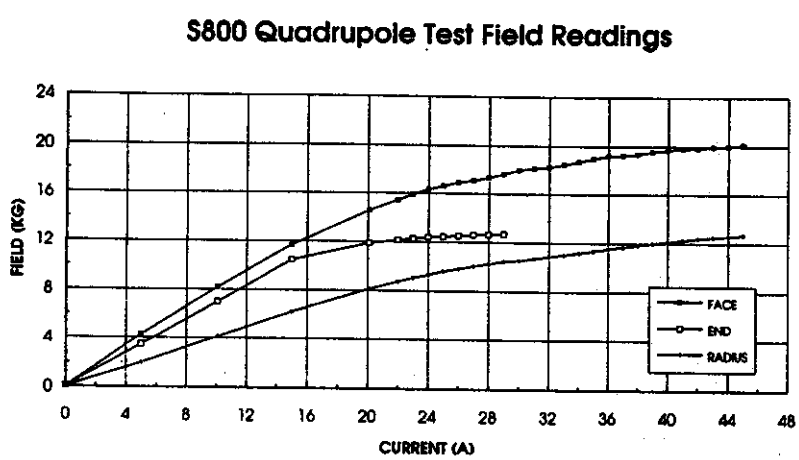

Figure 1: Field readings vs. hall chip location for S800 beamline quadrupole.

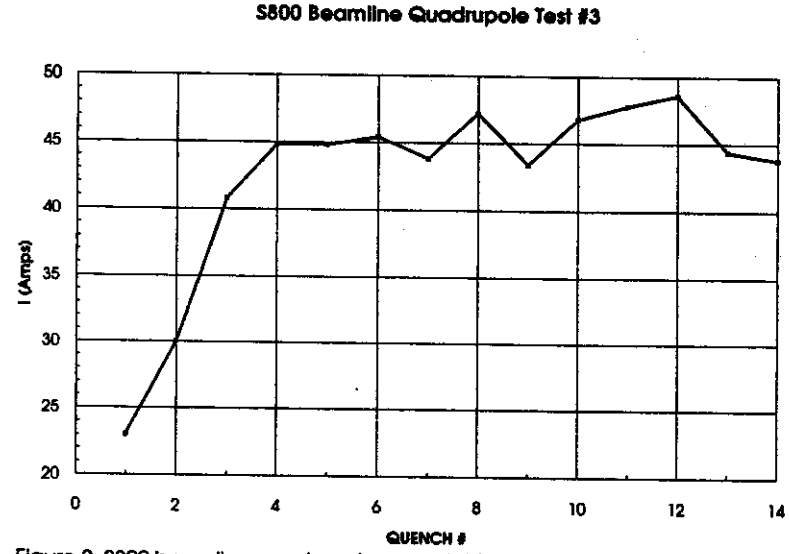

Figure 2: S800 beamline quadrupole quench history.

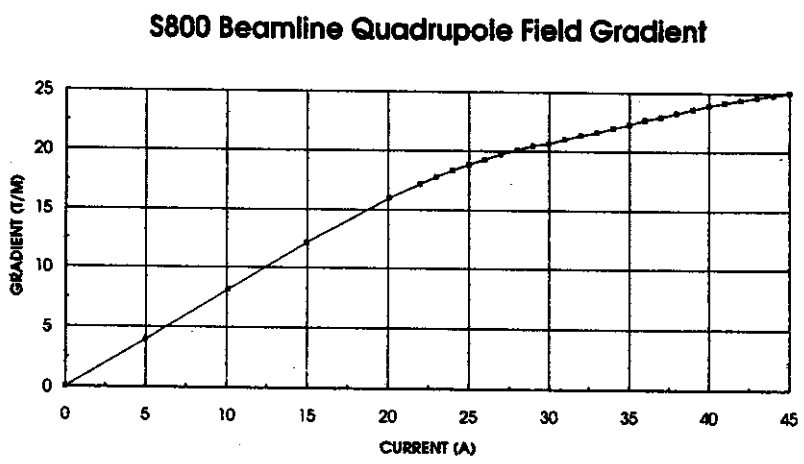

Figure 3: Field gradient calculated from hall chip readings at a radius of 2".

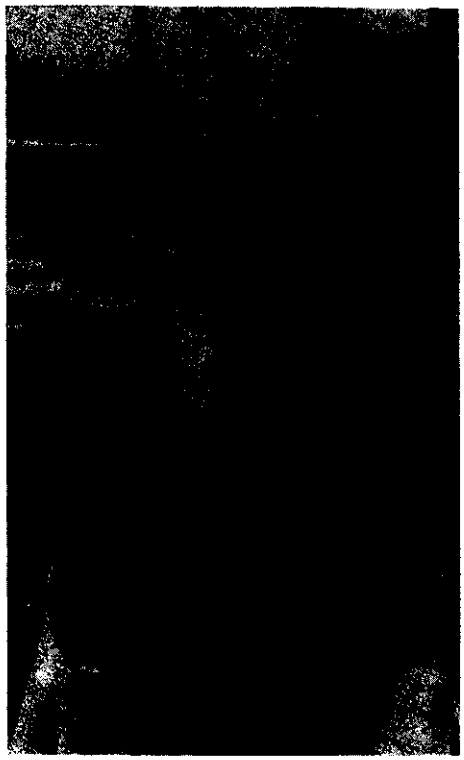

Figure 4: The S800 beamline quadrupole sitting in the LHe container bottom of the test cryostat.

Standard Beamline Quadrupoles Progress

A spare quadrupole triplet cryostat assembly for the A1200 was completed and tested. This will reduce downtime in case of a failure of one presently installed. Two doublets were also completed and tested, one of them new and one rebuilt due to a coil with turn-to-turn shorts. The rebuilt doublet had it's coils shimmed to the magnet steel differently than magnets previously built. Previously shims were placed on the sides of the coil facing the poletip first and than fitting the radial shims against the yoke steel as well as possible. The coils were then shimmed against each other thus restraining them radially and circumferentially. This resulted in the shimmed sides against the poletip being tight but the radial shims against the yoke not being tightly clamped . This made the current achived in the coil more dependent on the coil stiffness in the radial direction. This is the same direction as the highest overall coil forces. It was noticed that all of our half length quads in the 3 A1200 triplet cryostats built to date achieved 19-20A. As the coil is shorter, it also has a higher stiffness. The rebuilt doublet coils had their radial shims applied first and then were shimmed against each other making the radial shims tight. The shims against the poletip were fit last since there is no overall coil force in this direction, the shims are only there to keep the coil positioned evenly around the poletip. Testing of the rebuilt doublet showed both magnets trained to 20A. This is about 2-3A higher than the current usually achieved. Only a few other full length quads of the 65 constructed have achived 19A and never 2 in the same cryostat. This shimming order will now be used in future quads constructed. This doublet will be installed in the A1200 target upgrade in Feb. 1994. A small He leak to the insulation vacuum in the newly built doublet was noticed upon cooldown during it's testing, making it's heat load high. It is now out of it's vacuum container and being leak checked. This doublet is to be installed on the beamline to the S800 spectrograph.

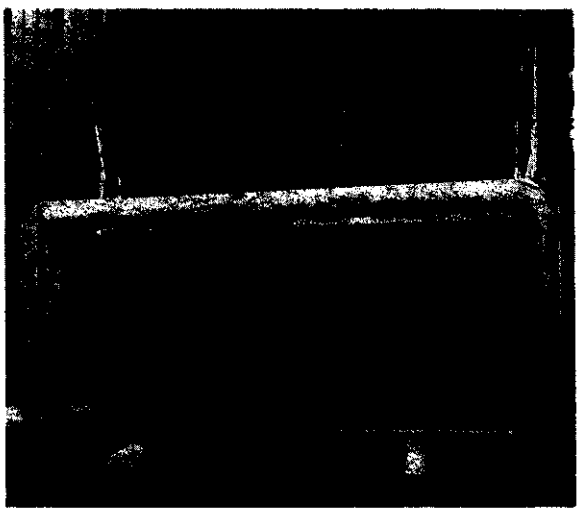

Figure 5: Completed S800 beamline dipole coil bobbin assembly.

Figure 6: S800 beamline dipole LHe container assembly.

Superconducting Beamline Dipoles Progress

The S800 beamline dipole magnets have their design complete, all parts needed are in house, and construction is progressing well. The coils for all 4 dipoles have been wound and 2 bobbins have their coils installed and are completely welded. The other 2 bobbins are welded to the point where coil assembly can be started. A complete coil bobbin assembly is shown in Figure 5. All of the LN_2 containers are welded and soldered to the thermal shield heat sink plates. The LHe containers are partially welded with current leads, safety vent pipes, and partial feedline assemblies attached as well as the LHe level sensors installed as shown in Figure 6. The thermal shields have been fitup and preassembled and the upper vacuum boxes and bobbin vacuum walls are welded as much as can be done prior to assembly of their inside contents.

References

1. A.F. Zeller et al., "S800 Progress Report", MSU Annual Report (1992), p. 182.
2. A.F. Zeller et al., "Construction of a Superconducting Spectrometer Dipole Magnet", Advances in Cryogenic Engineering 37, Part A, 417(1992).
3. J.C. DeKamp et al., "Superconducting Beamline Quadrupoles and Dipoles", MSU Annual Report (1992), p. 170.
4. J.C. DeKamp et al., "Superconducting Beamline Magnet Construction and Operation", MSU Annual Report (1990), p. 204.
5. J.S. Winfield, D.J. Morrissey, B.M. Sherrill, and J.A. Winger, "Status of the A1200", MSU Annual Report (1992), p. 179.

PROTOTYPE DRIFT DETECTOR FOR S800 SPECTROMETER

J. Yurkon, D. Swan, B. Sherrill, D. Morrissey, and M. Steiner

The S800 Spectrograph design places heavy requirements on the design of the focal plane detector system. To fully utilize the capabilities of the S800 Spectrograph, the detectors need to have 0.2mm FWHM resolution in the Y axis, and 0.4mm FWHM in the X axis over a focal plane area of 15cm by 50cm. It must also have low differential non-linearities and high rate capabilities for a broad range of particles.

The Multi Wire Drift Counter has been used successfully for many years in High Energy Physics. It has high rate capability due to its segmentation, and drift detectors are known for their high resolution. With heavy ions though, there may be problems due to the higher production of delta electrons. This is because one normally triggers on the arrival of the first electron at the anode wire in order to achieve good linearity with the standard non-optimal drift field of a MWDC shown in Fig. 1. Ionization produced by

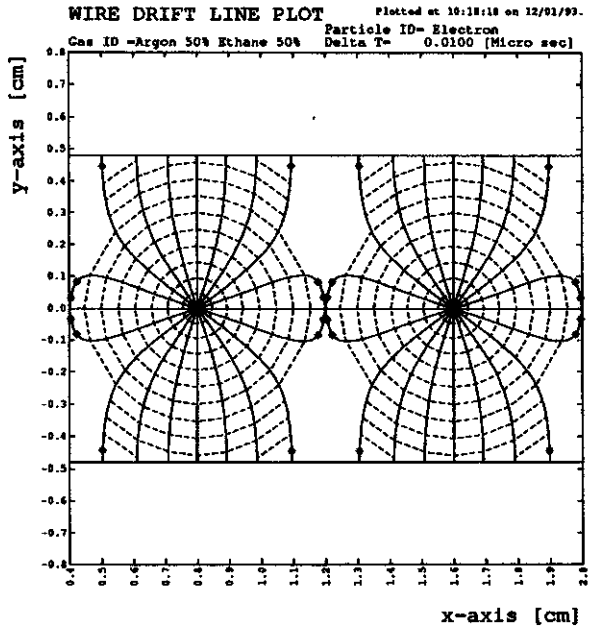

Figure 1: Drift Field in MWDC.

the delta electrons could cause a false pretrigger, hence degrading the resolution.

We decided to test a prototype MWDC to see how well it would perform with heavy ions. We based the design on the one at Los Alamos by Chris Morris. It has a nice feature that uses delay lines to reduce the number of channels of electronics. The difference signals from the delay line determines which anode wire had a hit and the sum gives the drift time to the anode wire. Thus only two TDCs are needed for each axis instead of one for each wire. The side of the anode wire where the track was located is determined by looking at the induced charge on the cathode wires that seperate the anode wires. The physical layout of the drift detector is shown in Fig. 2.

Fig. 3 is a plot of the X readout of the detector versus X position obtain from a silicon PSD, for ^{6}He and fragments. The drift detectors works well for these lighter beams as is demonstrated by the good correlation between the two detectors. The holes in the spectrum are at the field wire locations and are

the result of limitations in the calibration of each cell. Fig. 4 is a typical spectrum for an argon beam showing the problems that can occur from delta-electrons. This is a worst case setup. That is, heavy ions and triggering on first electron arrival. This spectrum should be just a strait line. However, when a delta electron produces ionization nearer to the anode wire than the track of the main particle, it causes the TDC to trigger early. The closer the main track to the wire, the smaller the time window in which this can occur. This is the reason for the bowtie shape. There are some artifacts in the spectra not due to the detector due to the left/right ambiguity being calibrated for only one wire. The ghosts away from the main line are due to delta electrons triggering anode wires that are not near the main track. This effect can be reduced by setting a threshold that is larger than the events produced by delta electrons, but smaller than the signal from the main track of ionization. However, this causes a deterioration in the linearity of the detector since were are now including electrons that drift along the longer curved paths in the detector, rather than only accepting the first arrivals which take a strait line near the center of the counter. Fig. 5(a) is a X-T correlation plot made with Garfield for our detector with a 50/50 argon/ethane gas fill at 760 torr and normal operating bias. Fig.5(b) is a measured X-T plot for ^{6}He ions which demonstrates the good linearity of the detector. The particle track in the simulation was incident at 0 degrees. The plot shows minimum drift time of the electrons from the track, to the anode wire, as a function of position. The lower curve shows the departure from non-linearity. We have tested the counter with oxygen, argon, and fragmented beams. It has also been used successfully in several experiments. However, it is difficult to use because of the calibration of essentially many seperate detectors and the careful setup need to reduce the associated problem with delta electrons. Fig. 6 is from an oxygen run and shows the image of a mask with two 1/16 inch diameter holes separated by 0.197 inches. The measured resolution was about 360 μm.

Table 1 shows the number and current status or our Multiwire Drift Counters.

Number	X and/or Y	Field Wire	Anode Wire	Location	Assembled
1	X&Y	76 μm Al/Cu/Au	12.5 μm W	NSCL	Yes
1	Y	76 μm Al/Cu/Au	25 μm W	NSCL	Yes
1	X&Y	76 μm Al/Cu/Au	12.5 μm W	CMU	No
1	X&Y	76 μm Al/Cu/Au	25 μm W	NSCL	No

Table 1: Status and Number of MWDC Detectors.

We will probably build a version of a MWDC for the S800 for those experiments which require very high counting rates.

We will be investingating other types of detectors in the near future. Amongs these are Cathode Readout Drift Detectors like the one used with SMART at Riken, and SPEG at GANIL. Also, we will investigate readout methods such as the individual readout and the delay line readout used for SMART and SPEG respectively.

References

1. S800 Workshop on Focal Plane Detectors, Eds. J. Bartlett and B.M. Sherrill, MSUCL-877.
2. Garfield, a drift-chamber simulation program, Rob Veenhof, CERN.

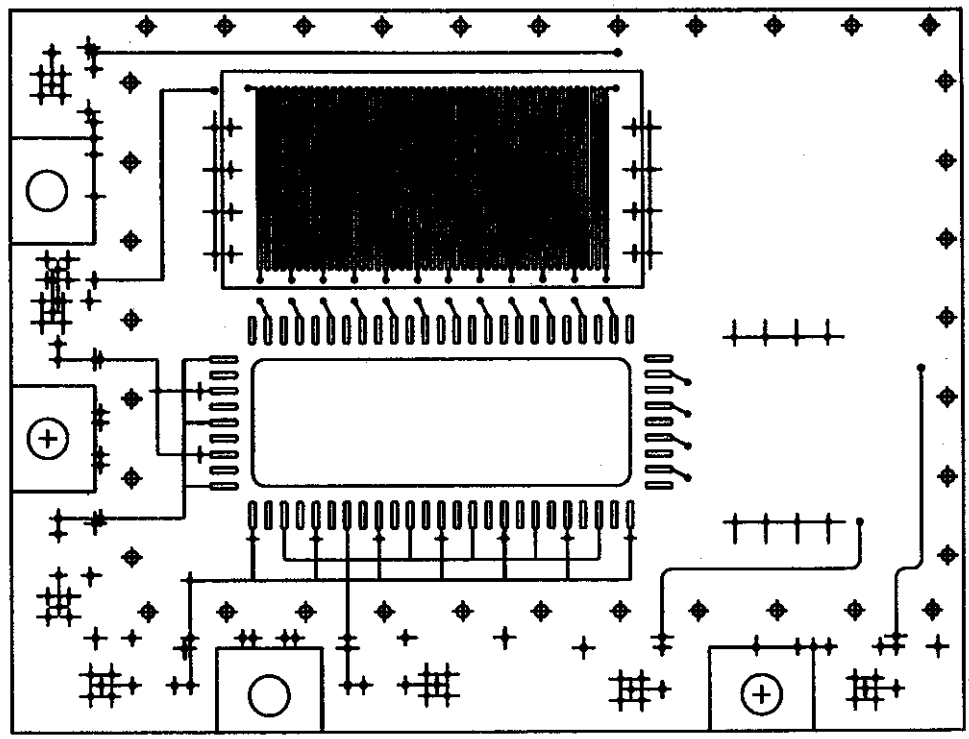

Figure 2: Drift Detector PC Board.

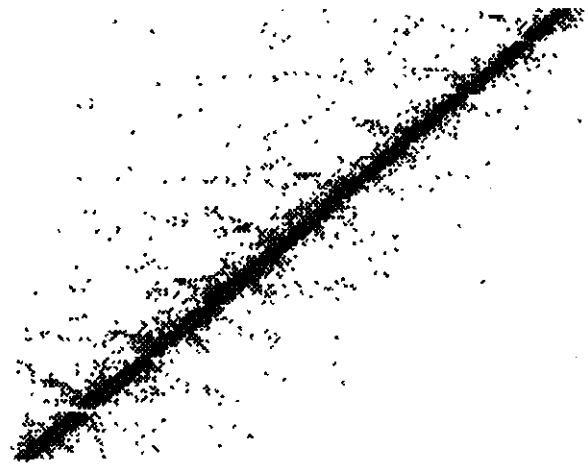

Figure 3: X MWDC vs X Silicon for ^{6}He.

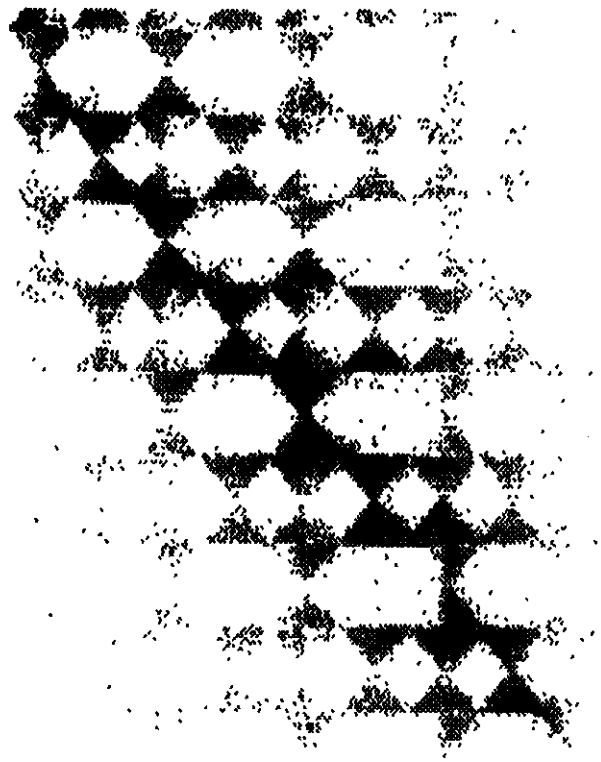

Figure 4: X MWDC vs X Silicon PSD.

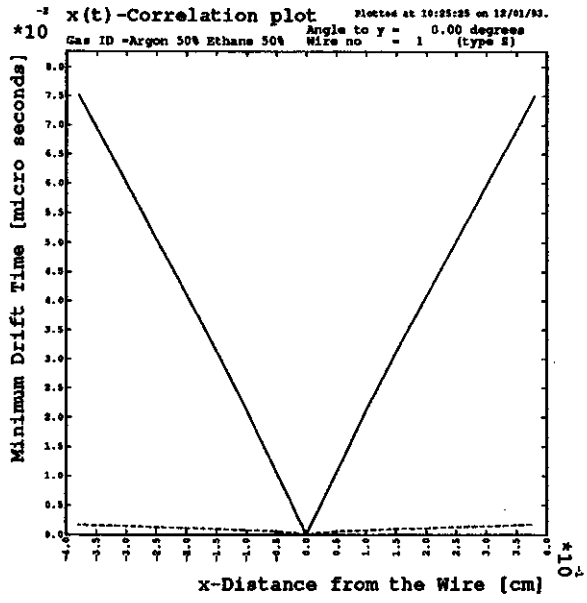

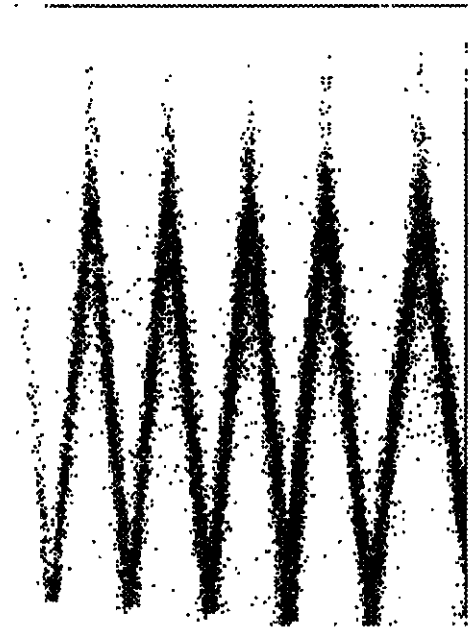

Figure 5: (a) X-T Correlation Plot, (b) ^{6}He X-T Correlation Plot.

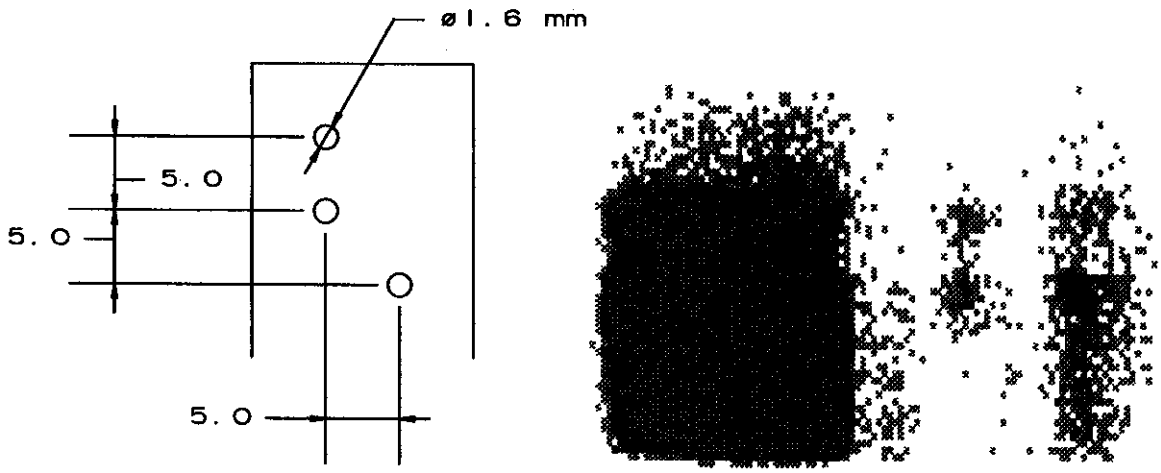

Figure 6: (a) Layout of Mask, (b) Image of Mask.

THE XAMINE DISPLAY PROGRAM

Ron Fox, and the experimentalists of NSCL

1 Introduction

This article describes the construction and status of a new NSCL histogram display package called Xamine. This package was co-designed by the experimentalists at NSCL and the computer group. A series of functional prototype pre-releases have been made available to the user community and are converging on an initial release.

Prior to the development of Xamine, NSCL used a display package called the AEDTSK (also developed at NSCL). This program was originally written to run on an Advanced Electronic Design AED-512 color display terminal. It was ported to DEC UIS when that became available and made to run on X11 using the UISX portability tool.

AEDTSK communicated with an independent histogramming process via shared memory and mailboxes. AEDTSK communicated with the user via a pointer and single letter commands (heritage of the AED-512 days). As X11 and Motif became widely available, the user interface of the AEDTSK rapidly became dated. As RISC processors came into fashion, the dependence of AEDTSK on a proprieatary package such as UIS made it essential to begin a move towards a native X11 display program which was capable of running under VMS and several forms of UNIX.

Instead of another port of AEDTSK, we decided to incoroporate a few years of feedback on user interfaces and AEDTSK functionality and develop a new program. We called this program Xamine.

Section 2 will describe the functionality and philosophy of Xamine, while a final section describes the current status and availability of the program. Section 3 will describe how Xamine was developed.

2 Description

This section describes the functionality of Xamine. Xamine was written using X11 and the Motif widget toolkit. The Motif toolkit provides a canned set of user interface primitives like buttons, sliders, dialogs, menus and so on. Motif also provides a set of objects which allow you to group these primitives into any desired arrangement.

Xamine is implemented as a single "main window." The main window is shown in figure 1. At the top of the main window is a menu bar. All of Xamine's functionality can be reached through the menus that drop down from the menu bar.

The large area in the middle is the spectrum display area. This area can be subdivided into a grid of panes. Each pane can display a spectrum. Panes have display attributes which affect the way the spectrum shown in the pane is displayed. For example, a pane can have the *log* attribute turned on, in which case the counts axis will be logarithmic. The pane configuration, content descriptions and attributes can be saved to file and restored.

Just below the spectrum display area is an optional status bar. When it is enabled, the status bar continuously displays the coordinates of the cursor in spectrum number, channels and counts.

Below the status bar, Xamine displays a set of button boxes with the most frequently used functions. This allows many function to be performed without accessing the menus.

Xamine's user interface paradigm is "sticky object" "verb". One of the panes is considered the selected pane (the selected pane is chosen by clicking in it with the mouse). All operations which must have a pane as a target (e.g. put spectrum in pane) operate on the selected pane.

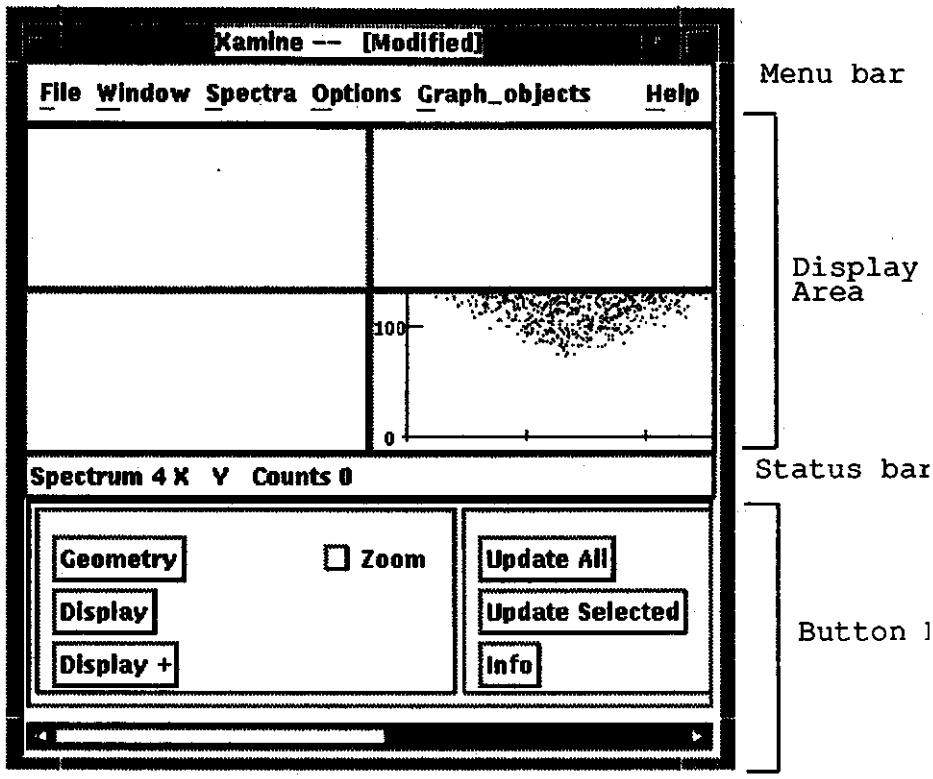

Figure 1: Xamine's main window

2.1 Prompting for input

Some Xamine functions require further input. These are prompted for by dialogs. There are essentially two kinds of dialogs, non graphical and graphical. All dialogs have help buttons which provide a description of what the dialog is prompting for and operating instructions. Thus to a large extent, Xamine is self documenting.

A non graphical dialog accepts data which are not spectrum coordinates. For example, figure 2 shows a dialog which alters the number of panes which will be displayed.

A graphical dialog accepts points on a spectrum. For example a 2-d spectrum expansion accepts an expansion rectangle. Graphical input dialogs accept input either with the mouse (clicking in the spectrum), or by typing in the coordinates with the keyboard.

2.2 Graphical objects

Xamine supports several kinds of graphical objects. Graphical objects are annotations which are displayed on a spectrum. There are two major classes of graphical objects, those which Xamine interprets and those which the histogramming client interprets. Histogram interpreted objects are currently called *gates* since that's what they're typically used for.

Xamine provides the following graphical objects which it interprets locally:

Marker A marker is a point. It has position, a name and an identifier. Markers are typically used to note changes in position relative to a previously known fixed point.

Summing Region Summing regions designate regions of integration. On a 1-d spectrum a summing region is a pair of limits. On a 2-d spectrum, summing regions are arbitrary closed contours. Graphical fill algorithms are used to support quick integrations inside the most pathological of summing regions.

Markers and summing regions are accepted using graphical input dialogs. The set of markers and summing regions can be saved to file and read back in.

Xamine provides gate graphical objects. Gate graphical objects are accepted by Xamine and then passed to the client histogrammer, then forgotten. The client can request the display of gate graphical objects if it decides to accept them. The following gate graphical objects are available:

Cuts A 1-d upper/lower limit pair.
Bands An arbitrary polyline in a 2-d spectrum.
Contours An arbitrary polygon in a 2-d spectrum.

Gates also have names and identifiers.

2.3 Color

Xamine supports both monochrome and color display servers. Color is largely used in the intensity to color rendition mode of 2-d spectra. Users indicated a desire to be able to control both the set of colors used and the linearity of the color table.

User definable color tables are supported via a color table editor. The color table editor is an X/Motif application which allows the user to set the red green and blue intensities of each color cell in the color table. The user can also set the upper and lower limits in terms of percentage of full scale. This allows for arbitrary curves through the color table as well as user selectable colors.

Xamine's selection of a color table depends on both the existence of user defined color tables and the color resources of the X-server that is displaying Xamine's windows.

For a monochrome X-server, color 2-d renditions are disabled. Any color renditions within window files are transparently converted to scatter plots.

For a color X-server, the concept of a family of color tables is used. Xamine can handle systems with as few as four free colors and supports a maximum of sixty-four colors. Xamine determines how many free colors are available after Motif has allocated its color set and then loads the appropriate color table from the colortable family.If a user has defined a logical name (environment variable in UNIX) called XAMINE_COLORTABLE_DIR to point to a directory, then that directory will be searched for the appropriate member of the color table family when Xamine is loaded. If no appropriate color table file is found there, then Xamine will check the user's home directory. If no color table file is found in the user's home directory, then a complete family of default color tables is used to select a default color set.

3 Development

The development of a program with a graphical user interface poses both technical and ergonimical challenges. On the one hand developers must learn an d program to, in this case, the Motif user interface toolkit, and X11. On the other hand, programmers must take careful account of the work habits and desires of the potential usr community to ensure that the program will encourage productivity.

3.1 Co-development

The functional specifications of Xamine were derived in cooperation with the user community. Functional pre-releases were used to gather feedback about user interface features and to give the user community some experience with the possibilities and issues involved in graphical user interfaces.

This process is called co-development. In classical development, there is an initial period of interaction between the development group and the "customer" during which functional specifications are produced and reviewed. Once the customers and developers have signed off on these specifications, development procedes and the customer sits back and waits for the product. By contrast in co-development, the developers engage in dialog with the "customers" throughout the development process.

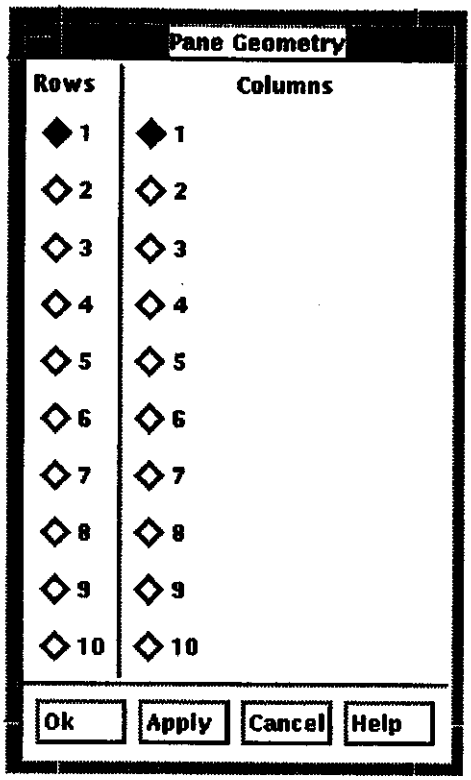

Figure 2: Xamine's geometry prompt dialog

Co-development recognizes that real world specifications are likely to be a moving target. Co-development makes use of functional prototyping to place partial implementations of the product in the customer's hands early in the development process to allow them to find and locate specification problems. These problems result in further discussions which feed back into features present in later prototypes.

3.2 Implementation issues

Xamine is a program which is a clear case for object oriented development. The Motif and Xt toolkits are object-like. Xamine manipulates spectra with well defined operations. Each spectrum displayed has several display attributes. Polymorphism can be used to clean up the code normally associated with attribute handling. Given these considerations, Xamine was implemented largely in C++.

Classes were defined to encapsulate the Motif toolkit widgets. In addition, classes were defined to describe and manipulate the display panes that display spectra. Finally, the spectrum region itself was defined using an object oriented strategy. Each dialog that Xamine produces is an instance of a specialized class which is derived from a generic user defined dialog class.

Object oriented development made the release of functional prototypes much easier than classical programming methods might have. It was easy to substitute alternate functionality without altering any of the rest of the program.

An example may be appropriate here. Xamine display panes have several attributes. When displaying a spectrum two of the more important attributes are the display rendition (e.g. scatter plot, box plot or color plot), and the reduction method used to display many channels in few pixels (e.g. sample, summed, or averaged). In addition, the axes may be oriented normally or flipped.

"Normal" coding for this would involve a bunch of conditional checks either to chose an appropriate

loop to display the channels or multiple condition checks within the loop itself. Using polymorphism, the method used is to create samplers and drawer objects. A set of conditional checks choose and instantiate a sampler and choose and instantiate a drawer. There is only a single loop. Each pass through the loop invokes the sampler method to sample a channel, and invokes a drawer method to draw a channel.

3.3 Portability

In today's fast changing computer market, a program which can only run on a single vendor's hardware does not provide sufficient strategic flexibility. Therefore, Xamine was written to be as portable as possible. Xamine functional releases are developed on SUN-OS 4.1.3. When a functional release point is reached, it is ported first to Ultrix 4.3 and then to Open VMS/VAX. Recently a port to Open VMS/AXP was completed. We anticipate that ports to OSF/1 will soon follow.

As each functional release is written, the upcomming ports are anticipated. Where possible common features are used, and where necessary, draft conditionalized code is produced to be debugged during the port. This procedure has been very successful. Xamine functional releases are usually available on all platforms within a week of SUN-OS code freeze.

4 Status and availability

Xamine has now been used for several months in off-line applications and, as of early May, for a couple of weeks in the on-line environment. The present release level of Xamine is X0.5 indicating that it is still at the functional prototype level.

While only a functional prototype, all of the functionality of the AEDTSK is present as are some extensions. Xamine is already proving to be a valuable and convenient tool. By retaining a high degree of programmatic compatibility with AEDTSK, it was possible to port the NSCL histogramming packages to run with Xamine in a very short time (one day at most). Counting M.S.U., Xamine is in use at four institutions.

I continue to solicit user input in order to improve what is already provided as well as to guide the development of new functionality. Xamine's portability insures that it has a long lifetime.

Xamine is available via anonymous ftp from rudolf.nscl.msu.edu (35.8.32.110). The program is distributed in source form (involving modules in C++, C and Fortran). The program files are in the directory pub/daq. Xamine.tar.Z is the compressed tar archive of the sources and build files. Xamine*.ctbl is a sample colortable family, while Xamine_pgm.ps and Xamine_user.ps are programming and user guides for Xamine respectively (postscript format). If you need assistance installing Xamine or have comments about Xamine, then please send E-mail to fox@nscl.nscl.msu.edu

A TRANSPUTER BASED MULTINODE DATA ACQUISITION FRONTEND FILTER

A. Vander Molen

The 4π Detector data acquisition system has been based on a single T-800 transputer. The orginal design called for a multi-node transputer farm to do real-time data filtering [1]. The frontend has now been upgraded to include this feature and has been used in several experiments.

One limiting factor in data taking is that some of the digitize data are undesired(noise, background, unidentifiable particles,etc.). This inturn results in a lower event rate that what could be achieved given the data rates are constrained by the data transfer bandwidth of the system. Currently the limits are 20 Kiloevents/sec. due mainly to ADC deadtime or 480 kilobytes/sec. due to tape writing limits. Not all undesired data can be filtered by hardware especially in the 4π Detector where a "single" gate is used. To remove undesired data in realtime and to add the capability of sophisticated filters a parallel processing frontend was designed and built for the 4π Detector.

The transputer network can be software configured but a fixed tree-like structure was chosen. See figure 1. The data is acquired in the same fashion as the past but the data is then sent in 500 Kbyte blocks to one of three nodes for processing. Each node then processes the data in parallel. Because the blocks of data are random data load balancing occurs naturally. The data processing can be either "unfiltered" or "filtered" depending on the menu selection chosen at the beginning of each run. The output is standard NSCL buffers but the buffer type number is changed for "filtered" buffers. The experimenter can then take "filtered" and "unfiltered" data and process them accordingly.

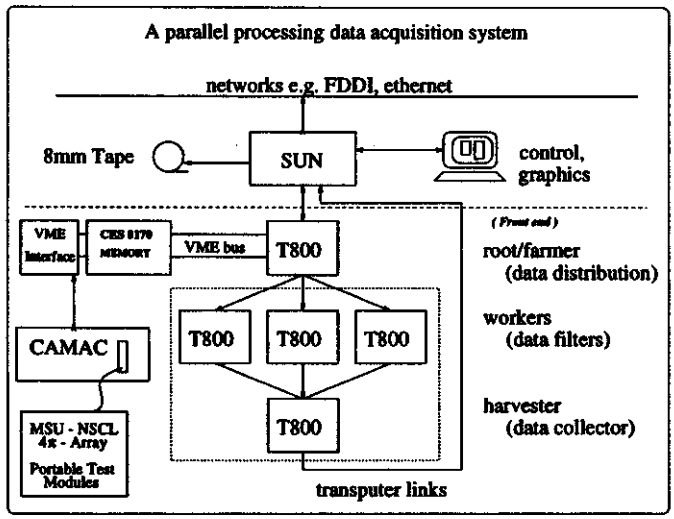

Fig. 1. The NSCL 4π detector data acquisition system. The orgininal system is the system outside the dash lined box. The components inside the box are the filter nodes.

The current data filter removes data produced by crosstalk by requiring an associated time signal. This filter has reduced the data set by a factor of two to three but the overall benefits are experimentally dependant. All the experiments benefit from the reduced noise on tape and the increased online data

processing but some experiments actually have shown an increased event rate due to less data being sent to tape; the current limiting factor. When the data event rates are low and the event size is small the filter has no effect on the rates but at high event rates or large events the limiting factor is the data to tape rate. Under these conditions the data to tape is reduced and therefore the event rate will go up. Experimentally both these extremes were seen. Further gains (30 %) could be achieved by removing reduntant data ID headers. Currently the data format is the same for "unfiltered" and "filtered" data to reduce the impact on analysis code. Future code will change this in concert with changes in the analysis software.

The software was written in such a way that other filters can be easily incorporated into the code. Such filters as true multiplicity cuts as opposed to hardware hit multiplicity, topology requirements, energy and momentum cuts are some of the filters proposed for the next generation. The current 5 node system shows a 20 % idle time. If more CPU cycles are required to handle more sophisticated algorithms in realtime the fourth node, the harvester, could have a parallel filter process incorporated in the code or more nodes can be easily added until realtime is achieved.

References

1. A Transputer Based Parallel Processing Frontend Data Acquisition System, A. Vander Molen, R. Au, R. Fox, and S. Hannuschke. IEEE Trans. Nucl. Sci., Vol.41, No. 1 pp 80-82

NSCL PEAK SENSING ADC

Albert McGilvra

Overview

The NSCL Peak Sensing Analog-to-Digital Converter (PSADC) is a single wide CAMAC module with eight 16-bit (64K channels) inputs. The module has an ECL data port that is FERA (LeCroy Fast Encoding and Readout ADC) compatible.

Each input is 0 to 10V full scale and has an individual threshold setting. The usable resolution is about 14-bits or 16K channels. The input pulses can have a rise time from 0.1uS to 10uS, however, performance is optimized for 1uS. The throughput is 150K-samples/sec per input or 1.2M-samples/sec total. The smallest pulse that can be digitized is aproximately 20mV. The differential non-linearity is 0.4% of one channel (or 0.06 ppm of full scale) with the Gatti sliding scale turned on and is 100% of one channel with it turned off. The Gatti sliding scale adds an anolog offset to the pulse amplitude and then subtracts it digitally. This spreads each channel over a range of 256, thereby reducung the differential non-linearity by a factor of 256.

The PSADC module has three major sections: the analog section, the readout section, and the control section.

The Analog Section

The analog section consists of eight input channels. Each channel consists of a peak detector circuit, a sample-and-hold chip, a "sliding-scale" summer, an ADC chip, one-eighth of an octal eight-bit DAC chip for threshold control, and one-half of a PLD (Programmable Logic Device) chip for control of the peak detector circuit.

The peak detector circuit takes the time derivative of the incoming pulse. A positive peak will cause the derivative to cross zero in the negative going direction. The derivative signal goes to a zero cross comparator. The output of the comparator triggers the sample-and-hold chip which holds the peak value.

The peak value then goes to a the sliding-scale summer where a random voltage is added to it. This random value is later subtracted in the digital domain. This doesn't affect the final digital code that represents the pulse but it does spread the digitization over several codes inside the ADC chip thereby statistically reducing the differential non-linearity of the module.

After having a random voltage added to it the peak value goes to the ADC chip where it is digitized. The ADC chip is an Analog Devices AD7884 16-bit ADC with 5.3 uS conversion time.

Before a pulse can get digitized two conditions must be met. First, it has to occur during the gate and second, it must surpass the threshold voltage. . The threshold DACs set this voltage below which pulses are ignored. The input pulse is compared to the threshold voltage and the output of this comparator goes to the peak detector control PLD chip. The PLD chip latches the comparator output if a peak has been detected and the gate is open. This latch is called the "valid data" bit. The valid data bit in turn disables the peak detector so that once a valid peak is detected no further peaks will disturb the sample-and-hold chip before the ADC chip has a chance to digitize.

The peak detector control PLD also tells the ADC chip when to start digitizing. It does this with the "conversion start" bit. The "conversion start" bit is only asserted after a valid peak has been detected and the sample-and-hold chip has had time to settle.

The Readout Section

Data can be readout via the CAMAC bus or the ECL port. The ECL port is a fast data port that can readout a 16-bit word in 120nS. If the ECL port is enabled then the ECL readout will be completed before the CAMAC port is enabled to read out. There are three ECL readout modes: sequential, compressed, and 12-bit mode. There are four CAMAC readout modes: sequential, compressed, 12-bit, and random access.

The sequential mode is simply a sequential readout of each channel starting with channel 0 and ending with channel 7. If a channel does not have valid data then it will read all 0's, if it has an overflow then it will read all 1's. The sequential readout format is illustrated in figure 1.

The compressed mode is also a sequential readout but only the channels with valid data (data that exceeded the threshold) are read out. The 16-bit data from each valid channel is read out in two transactions. The most significant byte (MSB) is read out first, followed by the least significant byte (LSB). The Word Count (WC) is the number of words following the header, 0 indicates 16 words. The 0 in bit position 8 of the header indicates standard 16-bit compressed mode (a 1 indicates 12-bit mode). The compressed readout format is illustrated in figure 2.

The 12-bit mode is similar to the compressed mode but each 16-bit data word is truncated to 12-bits so that it can be read out in one transaction instead of two. The 1 in bit position 8 of the header indicates 12-bit mode. The 12-bit mode is illustrated in figure 3.

The random access mode is available only on the CAMAC port. In this mode the CAMAC port individually addresses the channel to be read out. The data format is the same as the sequential mode.

	Bit#
	15 14 13 12 11 10 9 8 7 6 5 4 3 2 1 0
First Word :	Data for Channel 0
	:
	:
Last Word:	Data for Channel 7

Figure 1. ECL and CAMAC Sequential Readout Format

	Bit #				
	15	14 13 12 11		10 9 8	7 6 5 4 3 2 1 0
Header:	1	Word Count		0 0 0	Virtual Station Number
Word 1:	0	Ch Addr	0	0 0 0	MSB of Data
Word 2:	0	Ch Addr	0	0 0 0	LSB of Data
	:	:	:	:	:
	:	:	:	:	:
Word WC-1	0	Ch Addr	0	0 0 0	MSB of Data
Word WC	0	Ch Addr	0	0 0 0	LSB of Data

Figure 2. ECL and CAMAC Compressed Readout Format

	Bit#			
	15	14 13 12	11 10 9 8	7 6 5 4 3 2 1 0
Header:	1	WC	0 0 0 1	Virtual Station Number
Word 1:	0	Ch Addr	12-Bit Data	
	:	:	:	
	:	:	:	
Word WC	0	Ch Addr	12-Bit Data	

Figure 3. ECL and CAMAC 12-Bit Readout Format

The Control Section

The control section contains the CAMAC registers and implements overall module control. The CAMAC registers consist of the virtual station number (VSN) register, the control register, eight threshold registers, a sliding scale register, and eight data registers

The control register contains eight bits, these are: ECL port readout enable; ECL port data compression enable; ECL port data truncated to 12-bits; CAMAC data compression enable; CAMAC sequential readout enable; CAMAC data truncated to 12-bits; CAMAC LAM enable; and sliding scale enable.

There are CAMAC commands implemented to read and write all of these registers except the sliding scale register which can only be read. There are also commands to clear the module and self-test the module. The self-test command generates a gate and a 5V pulse which is applied to all inputs. This pulse can then be read out to check overall operation of each channel.

ANOMALOUS ENERGY LOSS OF HEAVY IONS IN MATTER

J.A. Caggiano, W. Benenson, B.M. Sherrill, M. Steiner, and B.M. Young[a]

The energy loss of an ion due to its passage through matter is normally taken to be independent of the charge state of the ion. Unexpectedly, recent measurements at the NSCL and at GANIL[1] in France have indicated that energy loss of heavy ions through matter can depend on the final emerging charge state even if the material is thick enough for the charge state distribution to reach equilibrium.

Two short experiments were performed last summer to measure charge state distributions of stripped heavy ions needed for the coupled cyclotron design. In the first experiment, ^{129}Xe and ^{238}U beams at 50 MeV/u and 20 MeV/u, respectively, were stripped with thin aluminum foils (4.1 mg/cm^2 for the ^{129}Xe, and four foils in the range of 0.3 to 2.0 mg/cm^2 for the ^{238}U). The charge state distributions were recorded at the second dispersive image of the A1200 spectrometer using Parallel Plate Avalanche Counters (PPACs). For the second experiment, ^{238}U ions were degraded in aluminum targets to energies of roughly 6, 7, and 10 MeV/u. The first section of the A1200 spectrometer was used to separate the degraded ions. These ions were subsequently stripped at the second dispersive image of the A1200 and allowed to pass through the second portion of the A1200. The charge state distribution of the ions was recorded at the focal plane with PPACs. Once their charge state distributions were known, the final energies of the emergent ions were determined. The method for charge state state determination is discussed in a separate report[2].

While analyzing this data, it was found that the energy loss depends upon emergent charge states in a non-linear manner. First this dependence was thought to have been due to the systematic dependence of the effective magnetic field on the NMR measurements of the spectrometer dipoles. However, the A1200 spectrometer has been found to act predictably over the range in question, so this effect can be corrected. The mass of the ion is also corrected for loss of mass due to electron stripping. After all corrections are accounted for, it still appears that the energy loss has a small but significant non-linear dependence on emergent charge state. Figure 1 and Figure 2 show the results for the xenon and uranium beams, respectively. Note that a second order polynomial fits the uranium data reasonably well, indicating that this effect is possibly quadratic in nature.

The energy loss of an ion depends on its velocity dependent effective charge, $\frac{dE}{dx} \propto Z_{eff}^2$. Hence, it is possible to extract an effective charge for each of the data points. Figure 3 is a plot of Z_{eff} vs Q_{meas}. A semi-empirical prediction was also made using formulae outlined in Ref. 3. Note that the predictions differ substantially from our measurements. An approved experiment is being planned to measure this effect[4] systematically and carefully and attempt to trace its origins, and to investigate this discrepancy.

a. Physics Department - Wright Nuclear Structure Laboratory, Yale University, New Haven, CT.

References

1. H. Gauvin, R. Bimbot, J. Herault, B. Kubica, R. Anne, G. Bastin, and F. Hubert, *Stopping Powers of Solids for ^{84,86}Kr, ^{100}Mo and ^{129,132}Xe Ions at Intermediate Energies (20-45 MeV/u) and the Charge State Distributions at Equilibrium*, Nuclear Instruments and Methods B47 (1990) 339-350.
2. J.A. Caggiano, W. Benenson, B.M. Sherrill, M.Steiner, and B.M. Young, *Charge State Determination of Partially Stripped Heavy Ions*, NSCL Annual Report, 1993.
3. F. Hubert, R. Bimbot, and H. Gauvin, *Range and Stopping-Power Tables for 2.5-500 MeV/Nucleon Heavy Ions in Solids*, Atomic Data and Nuclear Data Tables 46 (1990) 1-213.

4. J. A. Caggiano, W. Benenson, J. A. Brown, B. M. Sherrill, and M. Steiner, *Measurement of Energy Loss Dependence on Outgoing Charge State*, proposal submitted to the NSCL Program Advisory Committee and approved as experiment # 93039.

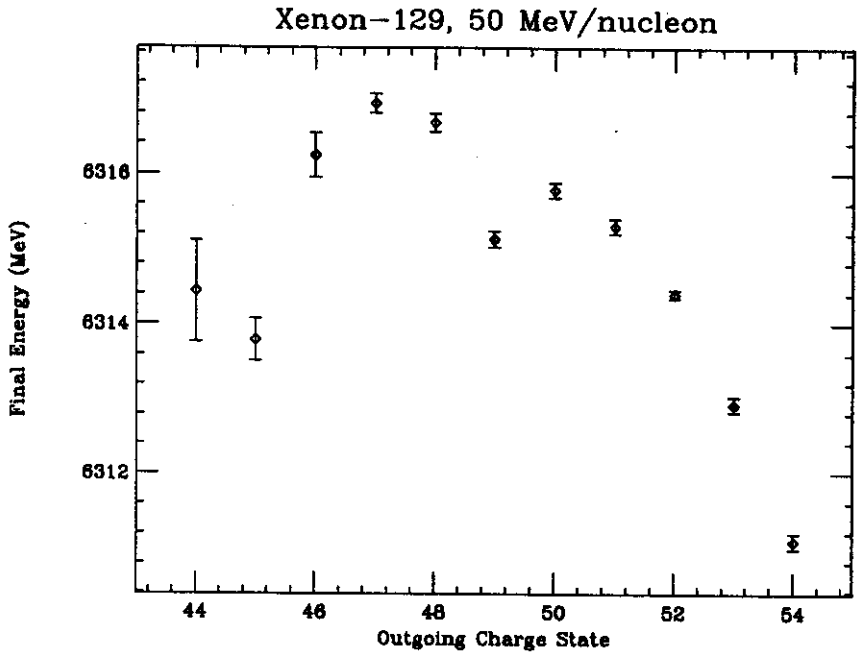

Figure 1: Final energy versus exiting charge state for ^{129}Xe at 50 MeV/nucleon on a 4.1 mg/cm^2 Al target. The maximum in the charge state distribution occurs at Q/e=52. The mean energy loss was 0.76 MeV/nucleon.

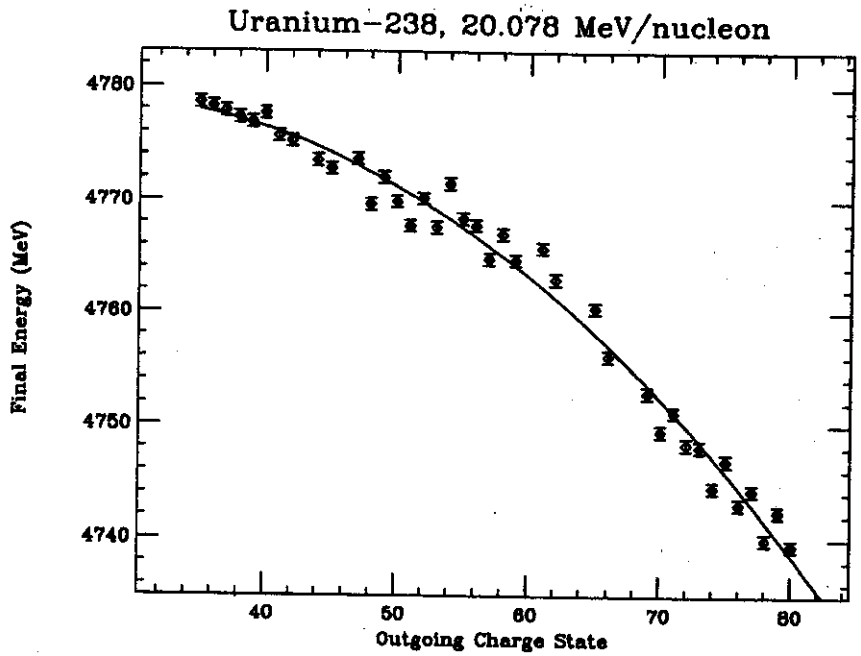

Figure 2: Final energy versus exiting charge state for ^{238}U at 20 MeV/nucleon on a 0.3 mg/cm^2 Al target. The fit was made with a second order polynomial. The mean energy loss was 0.12 MeV/nucleon. Two maxima occur in the charge state distribution because the foil was less than equilibrium thickness. The maxima occur at 49 Q/e and 72 Q/e.

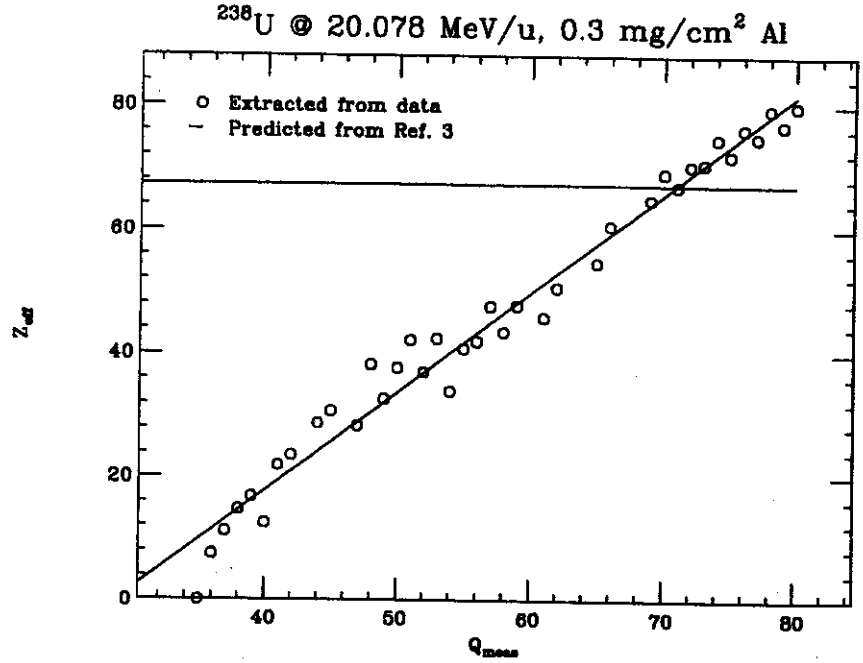

Figure 3: Effective charge, Z_{eff}, as a function of measured emerging charge state, Q_{meas}. A straight line fits the data reasonably except for the nonlinear approach to zero. The discrepancy between our values and semi-empirical predictions from Ref. 4 clearly indicates the need for further investigation.

CHARGE STATE DETERMINATION OF PARTIALLY STRIPPED HEAVY IONS

J.A. Caggiano, W. Benenson, B.M. Sherrill, M. Steiner, and B.M. Young[a]

While studying the coupling of the K500 and the K1200 cyclotrons at the NSCL, it became necessary to be able to predict with confidence charge state distributions of medium-energy (<20 MeV/A) heavy ions after passing through a foil. For ions with sufficient energy and low Z, charge state distributions are easy to calibrate because fully stripped ions can be made and easily identified. However, heavy ions such as gold and uranium are difficult to strip fully in the required energy range. When making a measurement of the charge state distribution, one needs a method to determine the charge state preferably on-line.

If the energy of the particle is well known, then determination of the charge states should be trivial. However, the energy of a heavy ion beam after emerging from a cyclotron or after being degraded isn't known well enough for these purposes. For each measurement, i.e. one charge state at one field setting, it is then not possible to determine the charge state *and* the energy of the ion. If a series of measurements are conducted, then it *is* possible to determine the charge state using a statistically rigorous process, and energy determination follows trivially. A method has been developed to do this at the NSCL. The process is relatively simple and can be done on-line. It only requires position information from position-sensitive detectors, a magnetic field measurement, and a guess at the charge states of the corresponding peaks.

The theory is simple. The bending radius of the particle passing through a uniform magnetic field is a function of its momentum, charge, and the magnetic field, $\rho = \frac{p}{Bq}$. When observing these particles on detectors following the magnetic field region, the transverse horizontal position, x, of the particles on the detector is also proportional to the bending radius in a linear fashion (assuming that the detectors are small). Consequently, plotting 1/Bq vs. x will yield a straight line provided that the charge states are correct. With enough data points, it is possible to perform a statistical analysis of the data using the linear correlation coefficient, r, to determine the correct charge state. By simply maximizing r or minimizing the reduced χ^2, it is possible to determine which set of charge states are correct.

The above concepts are implemented in a simple FORTRAN program, which performs three basic functions. First, it reads a file of data points, and calculates the quantity 1/Bq. Second, it calculates a correlation coefficient and reduced χ^2 for an initial guess at charge states. Last, it cycles through charge states, starting at 4 less than the guess and ending on 4 more than the guess, for a total of nine. For these nine statistical analyses, one 3x3 file in Topdrawer format is generated which will display all nine sets of data points and the straight line fit through the data points. The program also tells the user which charge states are correct, in relation to the set of guessed ones.

Figure 1 illustrates the output of the program when applied to a 50 MeV/A ^{129}Xe beam stripped with a 4.1 mg/cm^2 aluminum foil. In this particular case the original estimate of charge states was correct. This is a nice test of the program since this particular beam can be fully stripped. Figure 2 illustrates a more complicated case, 20 MeV/u ^{238}U, degraded to 9.92 MeV/u and stripped with a carbon foil. Notice that, for each beam, r is a maximum and χ^2 is a minimum for the correct set of charge states. Also note that the transition through the correct charge states is quite dramatic in both cases, indicating the power of this relatively simple technique.

Some sample charge state distributions have been measured and are illustrated in Figure 3. The A1200 spectrometer was used to separate the ions after stripping through a thin foil, and Parallel Plate

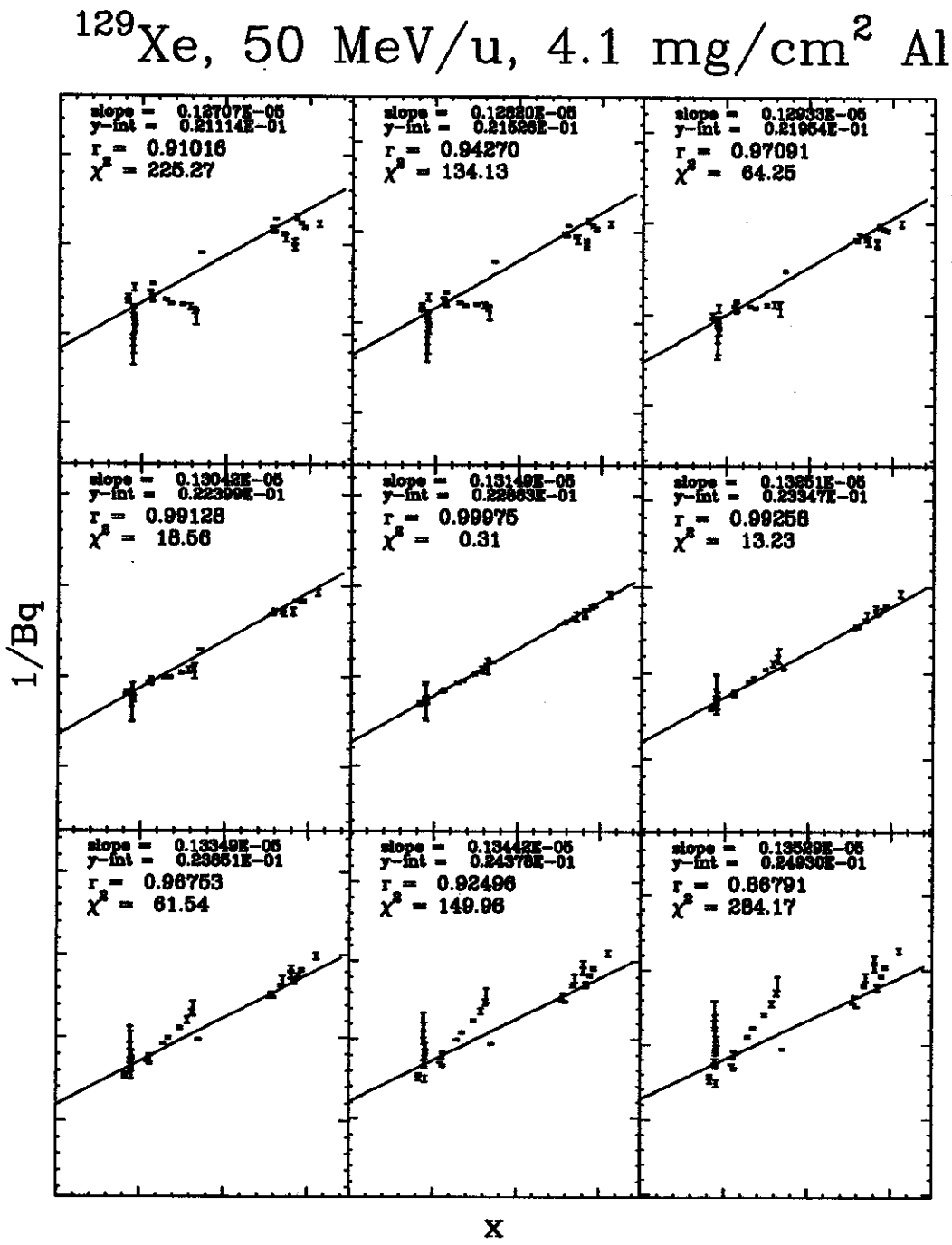

Figure 1: Statistical results from analysis with nine different charge state guesses for a 50 MeV/u ^{129}Xe beam stripped with a 4.1 mg/cm^2 aluminum foil. The abscissa is the channel on the detector; the range covered is 200-900 and the total span of the detector is 1024 channels. The center frame are the results from the correct guess at charge states.

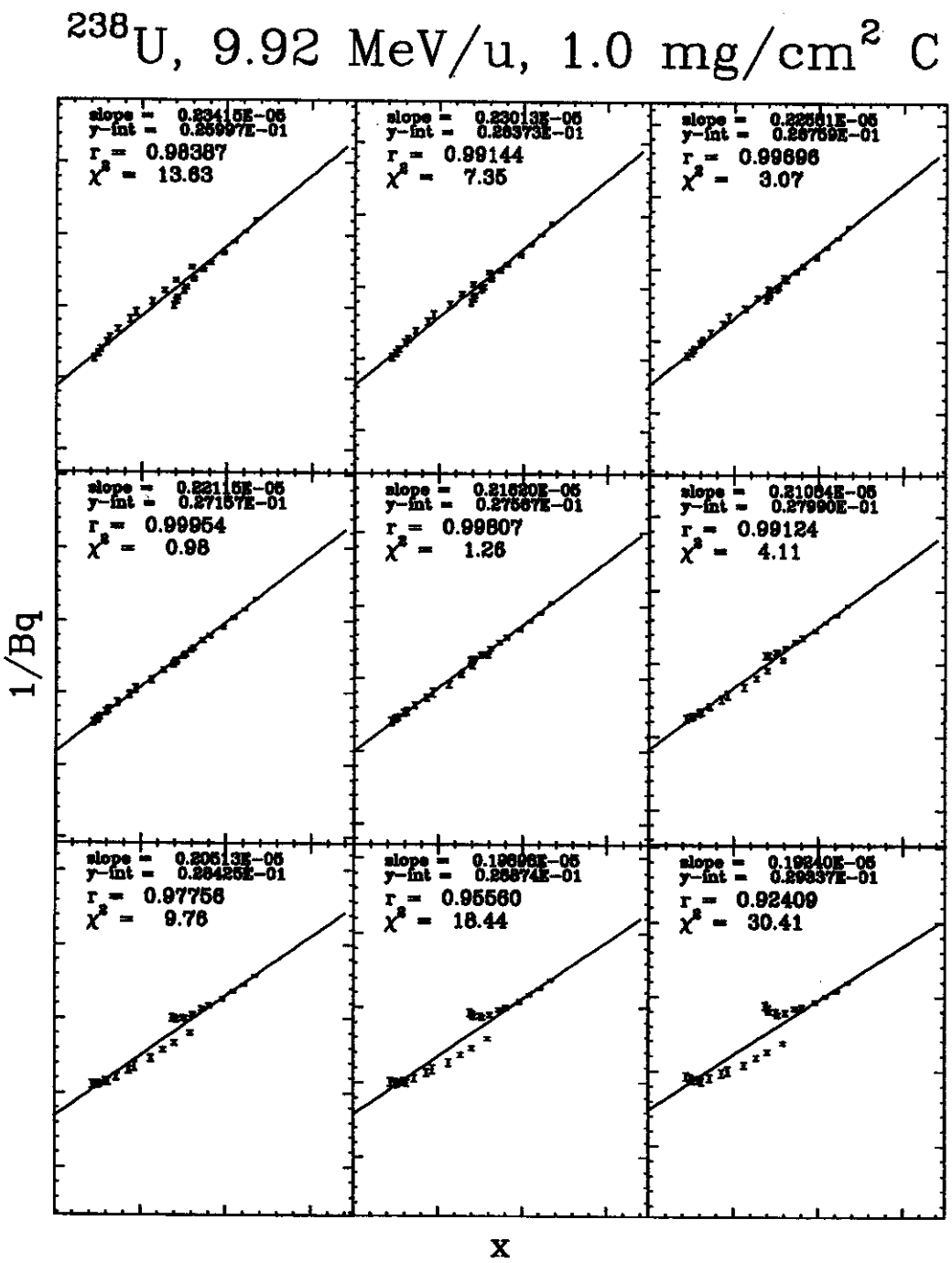

Figure 2: Statistical results from analysis with nine different charge state guesses for a 9.92 MeV/u ^{238}U beam stripped with a 1.0 mg/cm^2 carbon foil. The abscissa is the channel on the detector. The range covered is 200-900; the total span of the detector is 1024 channels. The center left frame is the result from the correct set of charge states.

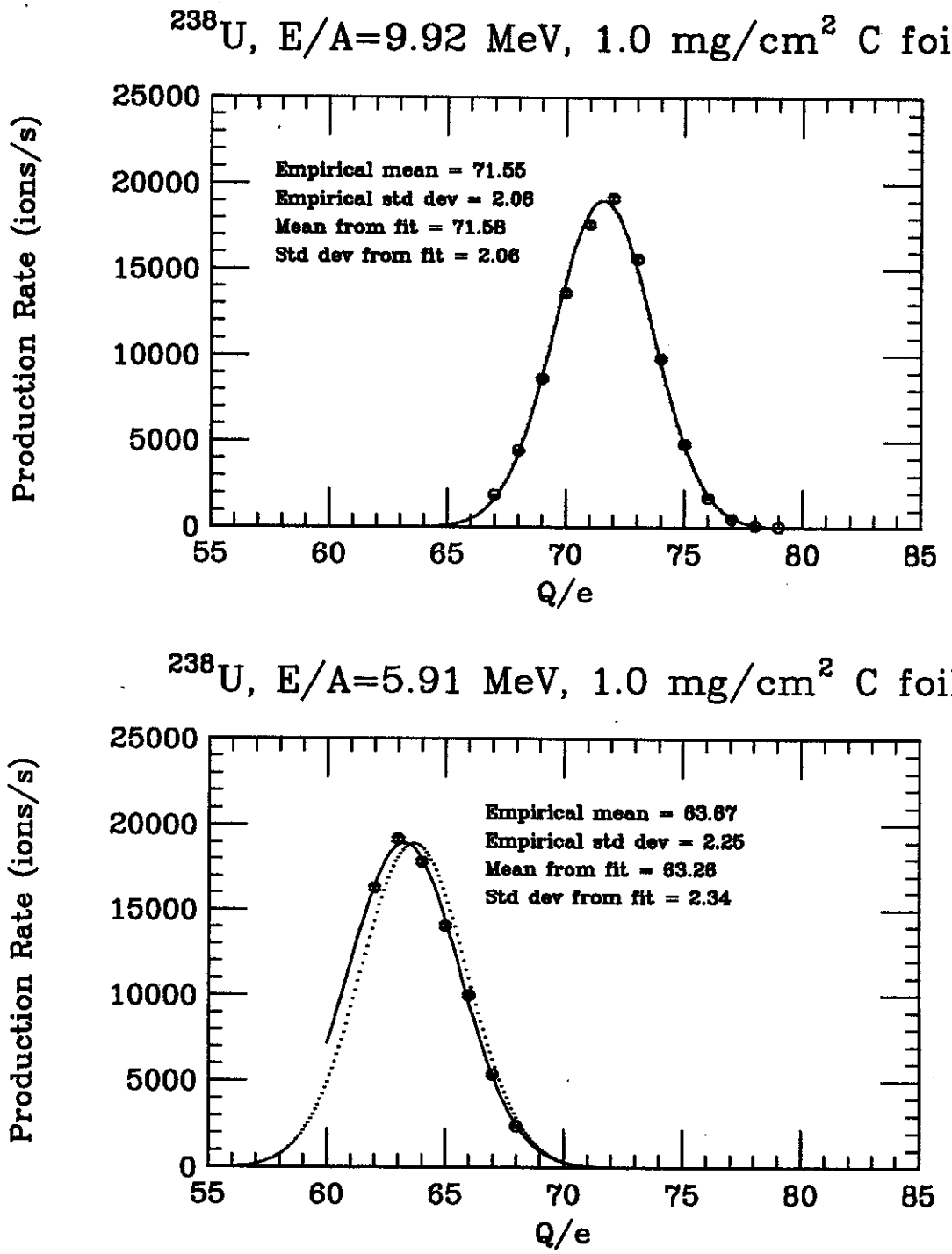

Figure 3: Experimental data for charge state distribution measurements taken at the NSCL in the summer of 1993 for ^{238}U at 9.92 MeV/u (top) and 5.91 MeV/u (bottom) on 1.0 mg/cm^2 carbon foils. The solid line is a gaussian fit and the dotted line is the empirical prediction of the GANIL group[1]. The values for peak position, Q, and standard deviation, d, are calculated using this formula.

Avalanche Counters (PPACs) were used to count the ions arriving at the focal plane of the spectrometer. It is interesting to compare these distributions with empirical predictions. Recently, a GANIL group[1] has evaluated a large quantity of data and established a fitting procedure that agrees very well with our experimental results. The fit assumes a pure gaussian charge state distribution of the form

$$F(Q) = N\, e^{(Q-\bar{Q})^2/2\,d^2}$$

where Q is the charge state, $\bar{Q}$ is the mean charge state, d is the standard deviation, and N is a normalization constant that can be freely chosen. The mean charge state is given by

$$\bar{Q} = \bar{Q}_p(1 - e^{(-12.905+0.2124Z-0.00122Z^2)})$$

where Z is the atomic number of the projectile and $\bar{Q}_p$ is given by

$$\bar{Q}_p = Z(1 - e^{-83.275\beta/Z^{0.447}})$$

where β is the projectile's velocity with respect to that of light. The standard deviation is given by

$$d = \sqrt{\bar{Q}_p(0.07535 + 0.19\,Y - 0.2654\,Y^2)}$$

and $Y = \bar{Q}_p/Z$. Figure 3 shows our results and comparison with the GANIL formulas. The empirical formulas predict the charge state distributions quite well, which strengthens our confidence in this technique.

a. Physics Department - Wright Nuclear Structure Laboratory,Yale University, New Haven, CT.

References

1. E. Baron, M. Bajard, and Ch. Ricaud, *Charge Exchange of Very Heavy Ions in Carbon Foils and in the Residual Gas of GANIL Cyclotrons*, Nuclear Instruments and Methods, A328 (1993) 177-182.

GAS FLOW IN THE A1200 PPAC DETECTORS

C. F. Powell, D. Swan, and D. J. Morrissey

The A1200 Fragment Separator relies on measurements of an ion's postion in order to determine its momentum, and to purify a beam of radioactive nuclei. In applications involving high count rates and good position resolution, Parallel Plate Avalanche Counters (PPAC's) are typically used. These detectors were built specifically for the A1200, and their design has been described in [1]. The PPAC's have proven to be reliable and accurate, with position resolution ~1.5 mm. In an effort to improve this resolution, studies of gas flow through the PPAC's were made.

An effect that has often been observed in the use of these detectors is large asymmetry of output signal amplitudes. This has been seen for a single ion between two dimensions of the same detector, and also between pairs of detectors. The effect is most noticeable at the A1200 focal plane and at intermediate image 2, where two PPAC's have their gas flow connected in series. Because the gas pressure is specified at the inlet of the first PPAC, a large pressure drop might cause a decrease in output signal size, particularly in the second detector. In order to determine whether variations in signal size are due to the pressure gradient or to normal manufacturing differences, the pressure drop was measured under a variety of conditions.

The first tests were done on a single PPAC in a test vacuum chamber (Figure 1). The pressure controller was set to 3,4,5, or 6 torr, and pressures at both the inlet and outlet of the PPAC were measured as a function of the gas flow rate (Figure 2). The inlet pressures remain fairly constant at all flow rates, indicating a large gas conductance between the pressure controller and the PPAC inlet. The outlet pressures, on the other hand, drop noticeably with increasing flow rate. At the maximum flow rate tested, 0.4 SCFH, the pressure drop across the PPAC is about 0.3 torr. This corresponds to a gas flow conductance of ~45 cm^3/s for a single PPAC. Calculation of conductance for the 0.125 inch ID tubing used to connect the PPAC to the manometer gives C=140 cm^3/s [2], a negligible flow resistance compared to the PPAC.

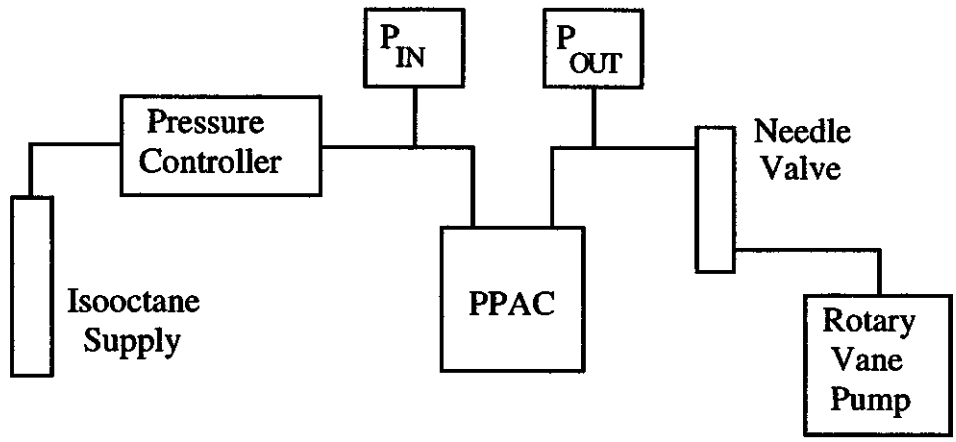

Figure 1: Schematic diagram of the setup for measuring the pressure drop across a PPAC at various pressures and flow rates.

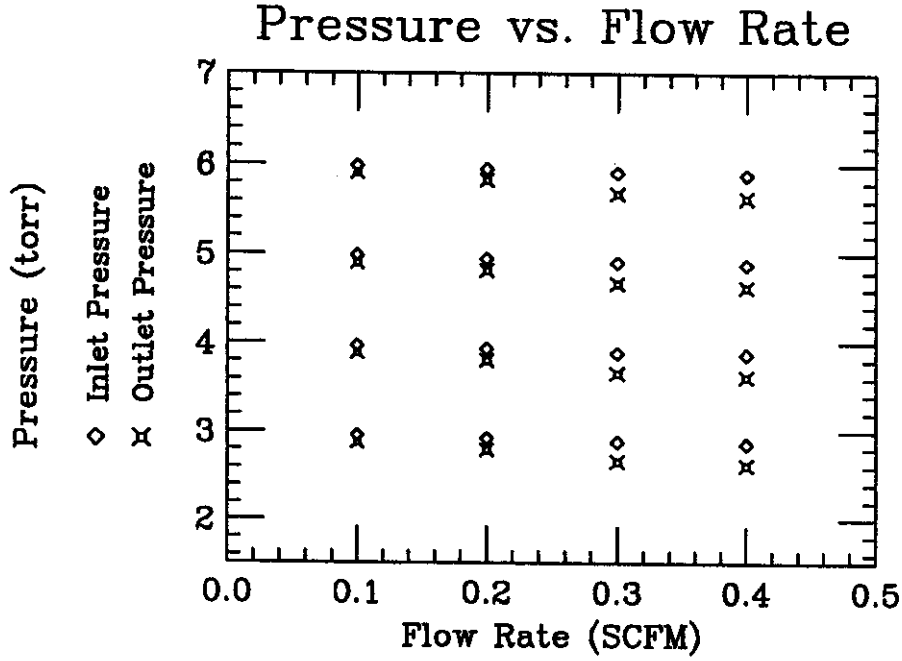

Figure 2. Inlet and outlet pressure of a single PPAC for various pressure controller and flow rate settings.

A second measurement was made at the A1200 focal plane using two PPAC's with gas flow connected in series. The outlet pressure was again measured as a function of gas flow rate. The observed pressure drop is consistent with an additive resistance from two individual PPAC's, with a total pressure drop across both PPAC's of ~0.6 torr.

Under experimental conditions, the A1200 PPAC's are typically operated at ~5.0 torr and ~0.2 SCFH gas flow. This pressure and flow rate correspond to a pressure drop of ~0.35 torr, a 7% effect. This pressure drop is noticeable, but probably not significant enough to cause the large differences in signal output sometimes seen (up to ~50%). This pressure gradient across the PPAC might be large enough, however, to cause significant bowing of the center and/or readout foils of the PPAC. This bowing of the foils will cause distortion of the electric field and variations in charge collection. Further studies, including modifications to PPAC design, are currently underway to try to maximize the gas flow conductance, therefore minimizing any bowing in the windows. Initial efforts have centered on adding new flow holes around the center foil, and have increased the conductance of a single PPAC to ~58 cm^3/s. In the meantime, flow rates should be set as low as can be tolerated in order to equalize charge collection.

References

1. D. Swan, J. Yurkon, and D. J. Morrissey, *Nucl. Inst. Meth.*, in press (1994).
2. J. F. O'Hanlon, *A User's Guide to Vacuum Technology*, 2nd ed., Wiley, New York, 1989, p. 30.

DEVELOPMENT AND USE OF A TIME PROJECTION CHAMBER FOR THE STUDY OF MULTI-PARTICLE DECAY PROCESS OF PROTON-RICH NUCLEI

D. Bazin[a,*], V. Borrel[b], E. Kashy[c], M. Lewitowicz[a], A.C. Mueller[b], F. Pougheon[b], M.-G. Saint-Laurent[a], O. Sorlin[b], J. Yurkon[c]

The principle of the Time Projection Chamber (TPC) is illustrated in fig. 1. The detector we have constructed consists of a large volume of gas in which a uniform electric field is created, associated with a Muti-Wire Proportional Counter (MWPC). An energetic charged particle moving in the gas produces electron-ion pairs along its path. The electrons drift towards the MWPC where they ignite an avalanche, inducing a signal on the wire (Anode). Because this signal is primarily caused by the motion of charges (principally the positive ions) in the vicinity of the wire, an induced signal of opposite polarity can be observed away from the avalanche site. This offers the possibility of reading-out two coordinates by placing strips perpendicular to the wires (Cathodes), as shown on the figure. The name TPC originates from the way the 3rd coordinate is deduced, i.e. by measuring the drift time of the electrons provided they have a constant velocity. A grid is placed above the anode wires in order to keep the drift electric field as homogeneous as possible. In addition, a set of equally spaced copper bands are printed on the circuit boards which surround the gas volume. Their potential is set by a chain of resistors to keep the field gradient constant.

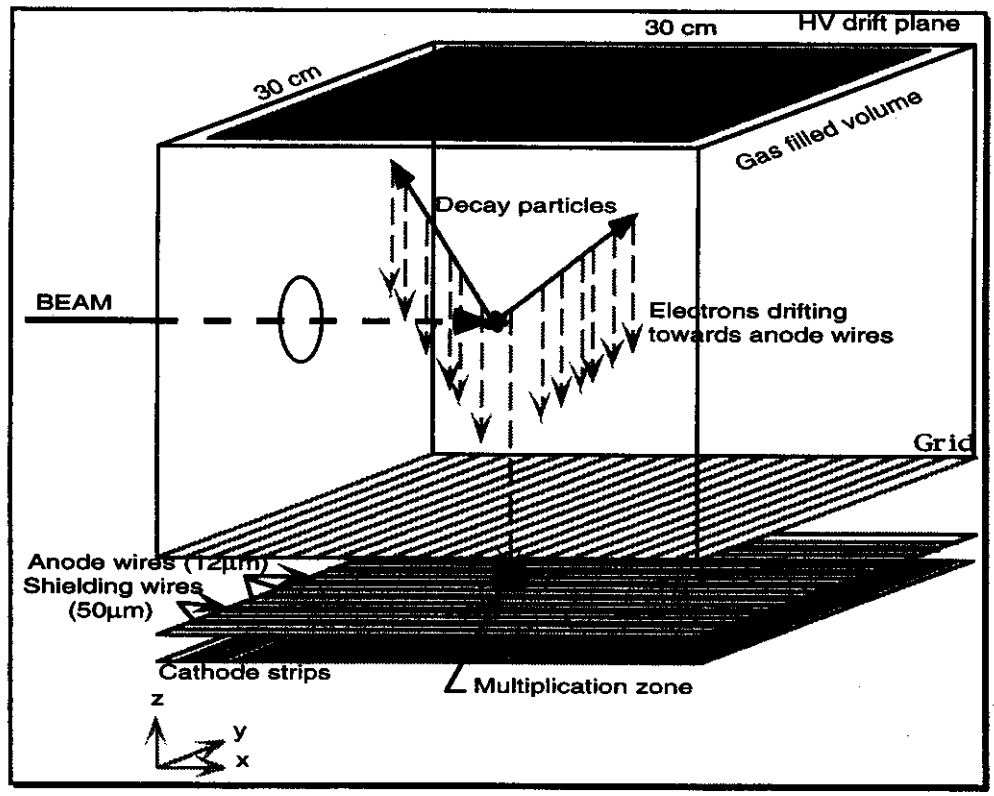

Figure 1: Schematic diagram of the TPC

The anode wires have a diameter of 12µm for high multiplication gain at high pressure and a spacing of 3/8" (about 1cm). They are interlaced with 50µm wires ("Shield wires") which are

maintained at ground potential to shield the anode wires from one another. Those thicker wires are all connected together and provide a direct measure of the total energy deposited in the detector, as they see an induced signal for each avalanche occurring on the anodes.

Each of the 32 anode wires and 32 cathode strips is connected to a voltage preamplifier via a motherboard mounted directly on the anode/cathode boards. Both the very short distance between the wires/strips and the preamplifiers and the HF shielding provided by the chamber in which the TPC is placed reduce the noise level down to the residual white noise of the preamplifiers.

Because there can be more than one avalanche on a given anode wire in the same event (when two tracks are above each other for instance), the drift time of the electrons was measured using multi-hit TDCs which can stack up to 16 hits on the same channel. However, the charge collected on each wire and strip was integrated over the whole length of the event (about 5μs) with QDCs.

The TPC chamber was used in a recent experiment with an ^{22}Al radioactive beam produced in the LISE spectrometer[1] at GANIL. The purpose of the experiment was to search for ß-delayed ^{2}He (or diproton) emission. Search for this process has already been done for decay from the ground state of predicted 1p-unbound but 2p-bound nuclei such as ^{39}Ti[2] or ^{45}Fe[3] as a direct tunneling emission similar to a-decay, but this new kind of radioactivity hasn't been found yet. A diproton emission can also occur from a 2p-unbound excited state, such as those populated by ß-decay of proton-rich nuclei. ß-2p decay has been observed[4] from the Isobaric Analog State (IAS) of ^{22}Mg following the Fermi ß-decay of ^{22}Al. A Further investigation[5] on this particular nucleus couldn't show any diproton component in the two-proton decay mainly due to poor statistics. One signature of a diproton decay is the angular correlation between the two protons after ^{2}He is released from the nucleus, using the combination of its well defined separation energy and the fixed energy of the decay.

The use of a TPC to detect such a correlation offers the advantage of an efficiency close to 4π, as opposed to more standard techniques involving silicon detectors. Another interesting feature is the reduction of the energy deposited by the ß-particle due to the uniform thickness provided by the cubic volume of gas, whereas a silicon detector has a very inhomogeneous spacial thickness distribution because of its construction. In fact, no track attributed to ß particles was observed during the experiment, which indicates as expected that their energy loss was very small, below the noise level. The gas used to operate the TPC was a purified mixture of 80% CF_4 - 20% Isobutane at 300 mbar. This choice is mainly determined by the range of the most energetic protons to be detected. CF_4 and Isobutane were chosen for their high stopping power and CF_4 in particular for its high drift velocity, allowing one to operate the detector at a lower pressure in order to reduce the electron recombinations as much as possible. The measured drift velocity is 1.8 cm/μs.

An example of a ß-delayed two proton decay is shown on fig. 2. The incoming ^{22}Al nuclei were first identified by TOF-energy loss through a silicon detector ahead of the TPC, then slowed down from their initial energy of 70 MeV/u by successive aluminum foils, before being implanted in the gas volume of the TPC. The very strong signal produced by the stopping of the nuclei was used to determine the vertex of the decay, indicated as circles on the figure. The time difference between the prompt signal of the silicon detector and the implantation signal recorded on the TPC provided a calibration of the drift velocity of the electrons. Using the standard single-implantation technique was justified by the production rate of ^{22}Al (3 pps), as compared to its half-life (70ms). After each implantation, the beam was stopped for a period of 150ms to observe the decays.

As shown on the figure, the TPC produces 2 time projections, one on the anodes and the other on the cathodes. Those projections on 2 perpendicular planes are used to reconstruct the particle trajectories in 3D space. Unfortunately, as it appears in this example, the cathode signals were too

close to the noise level, and either didn't provide any valuable time information or simply did not trigger the CFDs. The reasons for this behavior are now understood and will be explained below. Figure 2 shows the results of the automatic one-track and two-tracks fits which detects the two-proton events. The bar-histogram shown on the anode axis represents the energy loss collected on each fired anode. The Bragg curves of two protons going in opposite directions is clearly visible. The solid line

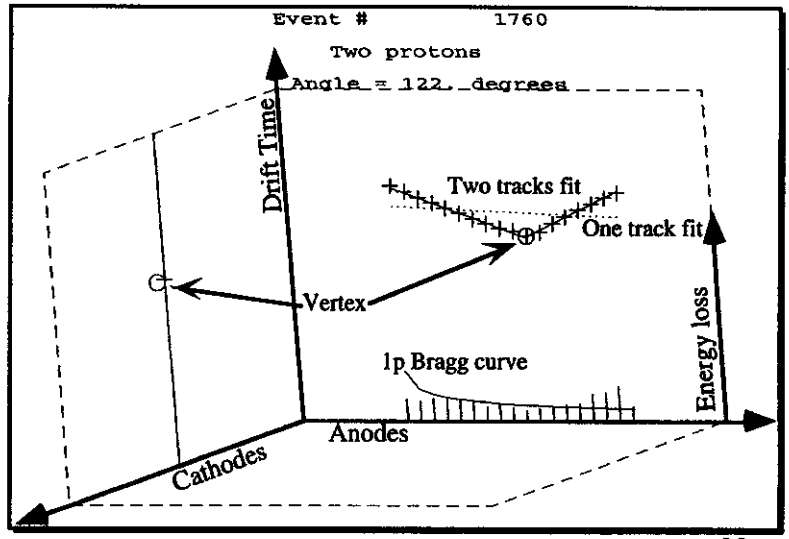

Figure 2: Example of a ß-delayed two-proton decay from ^{22}Al

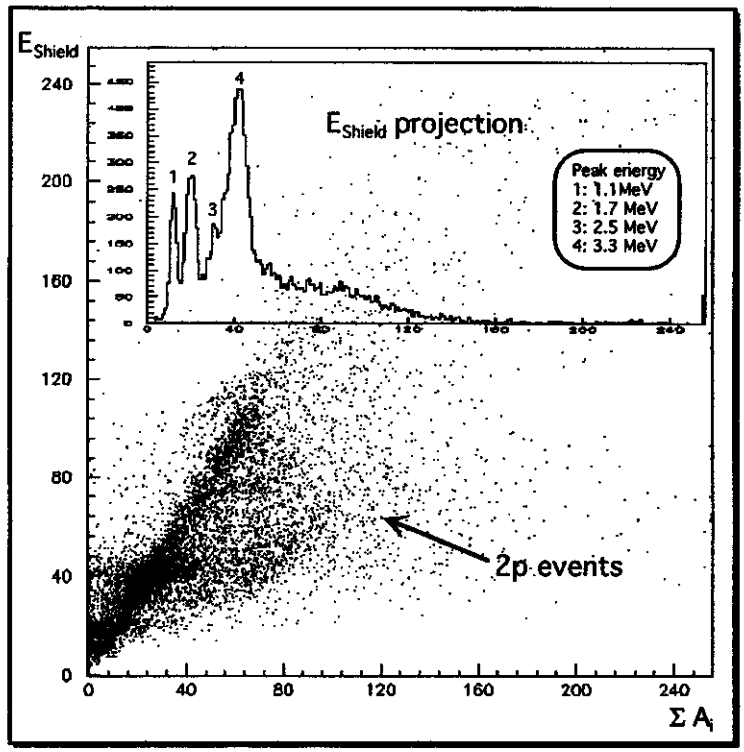

Figure 3: Total energy as measured on the Shield wires vs. the sum of individual energy losses recorded on each anode wire. The inset shows the E_{Shield} projection where structures appear at low energy.

is the calculated one-proton Bragg curve which is used by the analysis program as an additional criteria to select two-proton events. The angular correlation due to a diproton emission should still appear on a projection of the tracks, although smeared by the lack of complete information on the direction of the particles. The analysis of this anode-projected angle distribution is still in progress.

The next figure, (fig. 3) shows the behavior of the energy measurements of the TPC. Although there is a clear correlation between the energy measured on the Shield wires and the sum of energy losses of each fired anode, this correlation gets smeared out as the energy increases. More specifically, the energy measured as a global induced charge on the Shield wires is smaller for higher energies. This could be due to variations of the field configuration near the edges of the MWPC, which become important as the tracks get longer since the energy deposited peaks near the end of the Bragg curve. As a matter of fact, after visually selecting two-proton events and replotting them on this spectrum, it appears that most of them are located on the region where the E_{shield} energy is underestimated, which seems to corroborate an effect due to the spacial extend of the tracks. This feature was then used to pre-select two-proton events before their analysis by the fitting program.

In the inset of fig. 3 is plotted the E_{shield} projection of the spectrum where structures appear at low energy. The energy calibration was deduced from a measurement on ^{31}Ar for which the main ß-p and ß-2p peaks are well known. The energy resolution obtained is 0.57 MeV. The four peaks observed in the spectrum have been identified as the one-proton decay of ^{22}Mg excited states (6.59 , 7.21, 7.94 and 8.55 MeV respectively) to the ground state of ^{21}Na. The range of 3 MeV protons in 300 mbar of CF_4 is about 15 cm, therefore it is not surprising to see no structures above this energy, since the implantation sites are roughly located near the center of the gas volume.

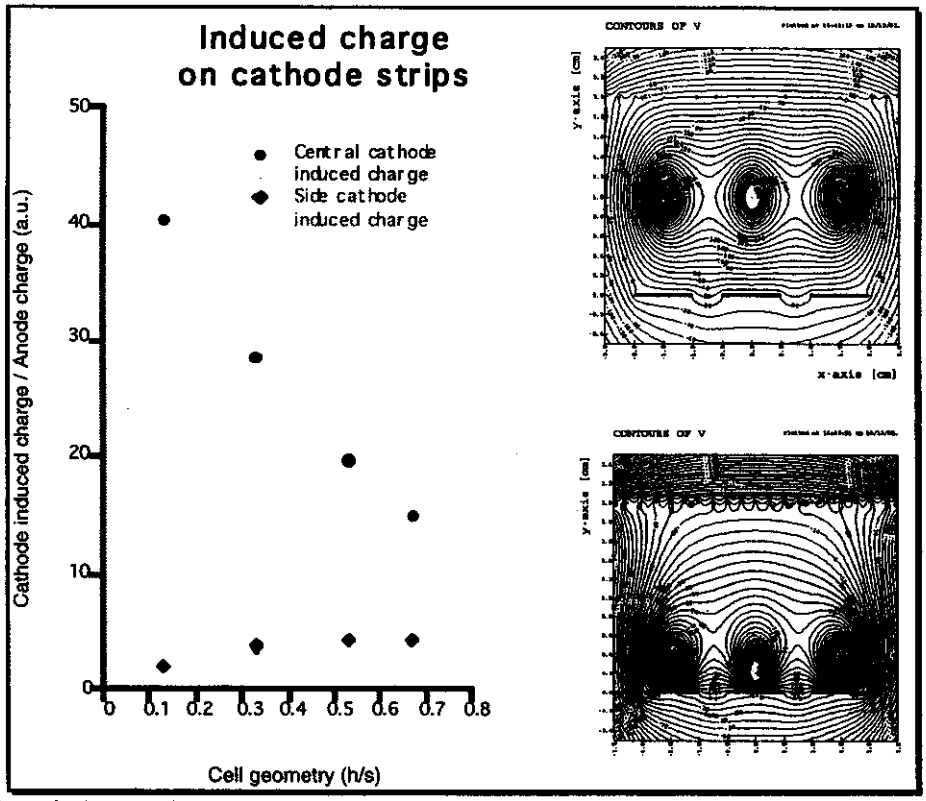

Figure 4: Induced charge simulations as a function of cell geometry. The two field contour plots show the cell configuration for the extreme cases h/s=0.67 and h/s=0.13.

Simulations of the electrostatic field in the MWPC have been done using the GARFIELD[6] program from CERN. The induced charge collected on the cathode strips was analyzed in a simple configuration of 3 wires on top of 3 strips, as shown on the field contour plots in fig. 4. The simulations were performed inducing an avalanche on the central wire only, in order to observe how the induced charge is distributed to the cathode strips. The plot shows the normalized cathode induced charge as a function of cell geometry for the central cathode (circles) and the adjacent ones (diamonds), where h is the distance between anodes and cathodes, and s the step between anodes. From the actual geometry of the TPC's MWPC of h/s=0.67 to the most compact geometry of h/s=0.13, the induced signal on the central cathode increases by a factor of 2.5 whereas the contribution to adjacent cathodes decreases by roughly a factor of 2. These results are clearly in favor of a compact geometry , which not only improves the signal/noise ratio, but also reduces the timing smearing which originates from the mixing of induced charges due to different multiplications. The effect of this smearing is to stretch the rise time of the signal (depending on the vertical orientation of the track) and make all cathodes signals alike, which destroys the vertical information provided by the timing. The modifications involved in changing the cell geometry of the MWPC are relatively minor, and will be soon undertaken, after which some tests using an a-source should show the expected improvements.

a: GANIL, BP 5027, 14021 CAEN Cedex, FRANCE
b: IPN Orsay, BP 1, 91406 ORSAY Cedex, FRANCE
c: NSCL, MSU, East Lansing, MI 48823-1321, USA
*: On leave at NSCL, MSU, East Lansing, MI 48823-1321, USA

References

1. R. Anne et al., Nucl. Instr. and Meth. **A257** (1987)215-232.
2. C. Détraz et al., Nucl. Phys. **A519** (1990)529-547.
3. V. Borrel et al., Z. Phys. **A344** (1992)135.
4. M. D. Cable et al., Phys. Rev. **C30** (1984)1276-1285.
5. R. Jahn et al., Phys. Rev. **C31** (1985)1576-1578.
6. Garfield, a drift-chamber simulation program, CERN Program library entry W5050, Copyright Rob Veenhof, 1989.

TESTS OF A FLASH-ADC SYSTEM FOR PARTICLE POSITION MEASUREMENTS

C. F. Powell, D. Swan, A. M. Vander Molen, and D. J. Morrissey

The A1200 fragment separator uses Parallel Plate Avalanche Counters (PPAC's) in order to measure the positions of energetic ions at the second intermediate image and at the focal plane. The design of these detectors has been described in [1]. With standard linear electronics (preamp/shaping amp/ADC) the position resolution is typically ~1.5 mm. In an effort to improve this resolution and in order to learn more about the operating characteristics of the PPAC's, a new style of detector readout was incorporated into the NSCL data acquisition system. These electronics utilize a flash-ADC (FADC) in order to record pulse shapes. It is hoped that this additional information about the detector signal will allow improved position determination.

Linear signals from the A1200 PPAC's are typically processed with an integrating preamplifier, shaping amplifier, and a 12-bit peak-sensing ADC. Reconstruction of the linear charge division is performed online in software in order to determine position in the x and y dimensions. A test station was set up with the standard electronics in parallel with a FADC system, allowing side-by-side comparison of the two measurement techniques. 5.5 MeV alpha particle were used to generate signals in the detector, and the position resolution is observed by placing a mask over the PPAC entrance window.

The new acquisition system feeds the four outputs of the PPAC into a slightly modified A1200 PPAC preamp. The gain of the preamps was reduced, and circuitry was added to zero the DC offset of the output. The preamp output was split, with one output going directly to the FADC, the other into a shaping amplifier in order to generate a fast logic signal to gate the acquisiton electronics. A Struck DL401 Flash-ADC was used for analog-to-digital conversion at a rate of 100 MHz. This FADC has 8 bits of resolution from ~0 to ~250 mV. The DC level was measured every 10 ns in each of four input channels for a total duration of 10 ms. Special care was taken to minimize electronic noise in the system. This is important in a DC sensitive system with such small gain. A noise level of ~1-2 mV was typically attained.

The FADC digitizes the signals from the preamp, and four traces of voltage versus time are obtained for each event. Traces for a typical alpha-particle event are shown in figure 1. The data were collected in a standard NSCL-MASH system and put into the standard buffer format. These traces are then written to disk for offline analysis and position determination.

Offline position determination can be performed in several different ways. The entire trace can be integrated and the area used in the charge division calculation. Alternatively, the height of the peak can be used, or various fits can be made to the shape of the peak. Each of these methods was tested to determine which gave the best position resolution. Another analysis technique used was smoothing of the voltage versus time traces with the technique described by Savitzky and Golay [2]. It was thought that smoothing the traces would minimize effects of electronic noise in the system.

Side-by-side comparisons of the two acquisition systems were made, with various methods used to compute position from the FADC data. Very little change in position resolution was seen among the different calculational techniques. Smoothing of the traces did improve resolution slightly, however. Figure 2 shows a comparison of data from the conventional electronics with data from the FADC. The two-dimensional histograms reproduce the mask that is placed over the entrance window of the detector. The one-dimensional histograms show intensities along the x and y axes for

each system. The widths of these peaks and the known hole sizes determine the position resolution. The conventional electronics give a position resolution of ~1.4 mm, while the FADC data corresponds to the slightly poorer resolution of ~1.8 mm.

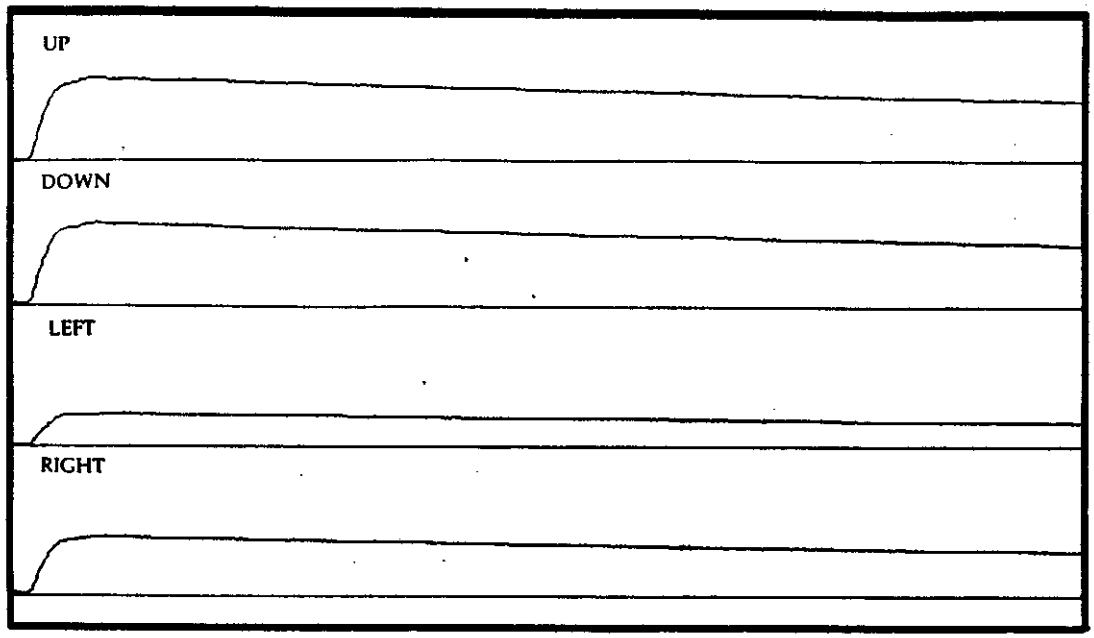

Figure 1. Voltage versus time traces obtained using the Struck DL401 FADC. Charge division is performed offline in order to determine an ion's position.

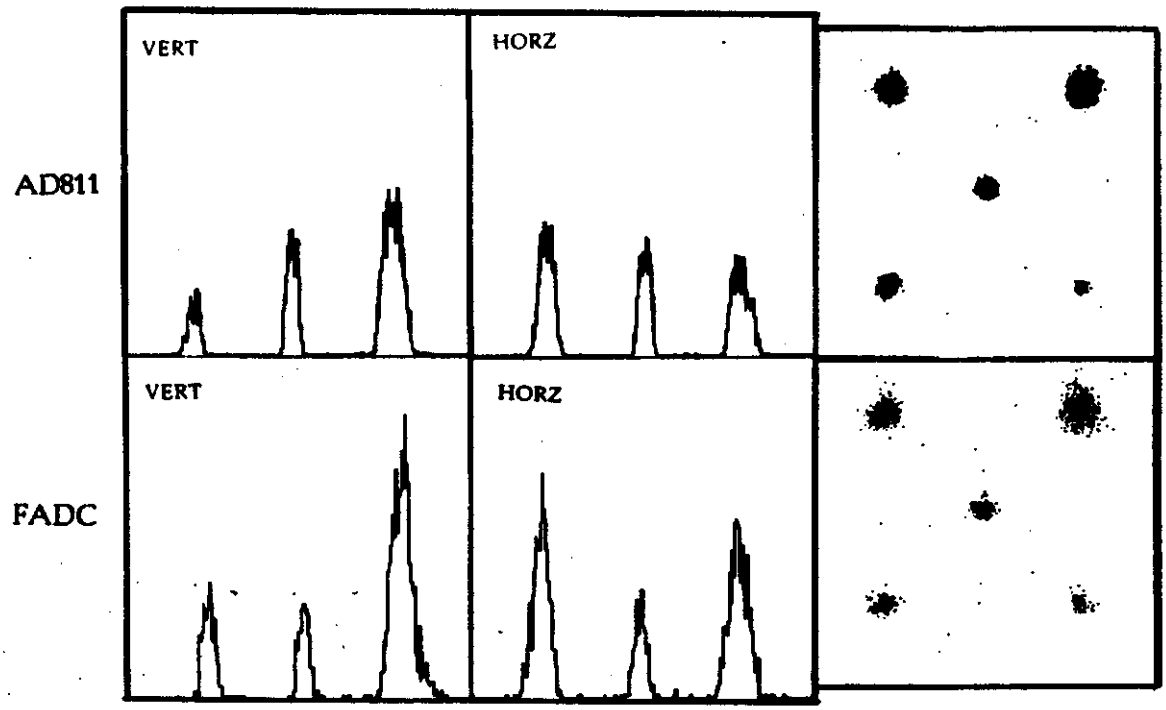

Figure 2. One and two-dimensional position histograms acquired with the Ortec AD811 peak-sensing ADC and the Struck DL401 FADC. Slightly better resolution is obtained with the 12-bit AD811.

Though the resolution using the FADC is not yet as good as that of the conventional electronics, this is not unexpected. The peak-sensing ADC used in the conventional electronics has 12 bits of resolution, while the FADC has only 8 bits. Without more complex calculational techniques that utilize the time information the FADC produces, its resolution is limited. Future plans for the system include switching from the common differentiating preamps to linear preamps. This would allow both fast and slow signals from the detector to be observed, additional information that may enhance resolution. Another technique would involve simulating a shaping amplifier in software, with several stages of differentiation and integration. With more advanced calculational techniques, the resolution of the FADC system may eventually match or exceed the resolution of the conventional electronics.

References

1. D. Swan, J. Yurkon, and D. J. Morrissey, *Nucl. Inst. Meth.*, in press (1994).
2. A. Savitzky and M. J. E. Golay, *Anal. Chem.* , 36 (1964) 1627.

PROGRESS TOWARDS THE DEVELOPMENT OF A LARGE-AREA, HIGH-EFFICIENCY NEUTRON DETECTOR

P.D. Zecher, A. Galonsky, J.J. Kruse, and J. Wang

A recent experiment performed at the NSCL measured the electromagnetic excitation of ^{11}Li [1,2] by making a complete kinematic measurement of the three reaction products: 2 neutrons and a ^{9}Li fragment. The neutrons were detected in a forward array of neutron detectors. This detector array, while suitable for an initial measurement, had several drawbacks. We have attempted to reduce or eliminate the array's limitations by constructing a new detector, which has come to be called the *Neutron Wall.*

The array was constructed of 54 small, cylindrical detectors closely packed into two planes whose normal was parallel to the beam direction (see Figure 1). Each detector is filled with a liquid hydrocarbon

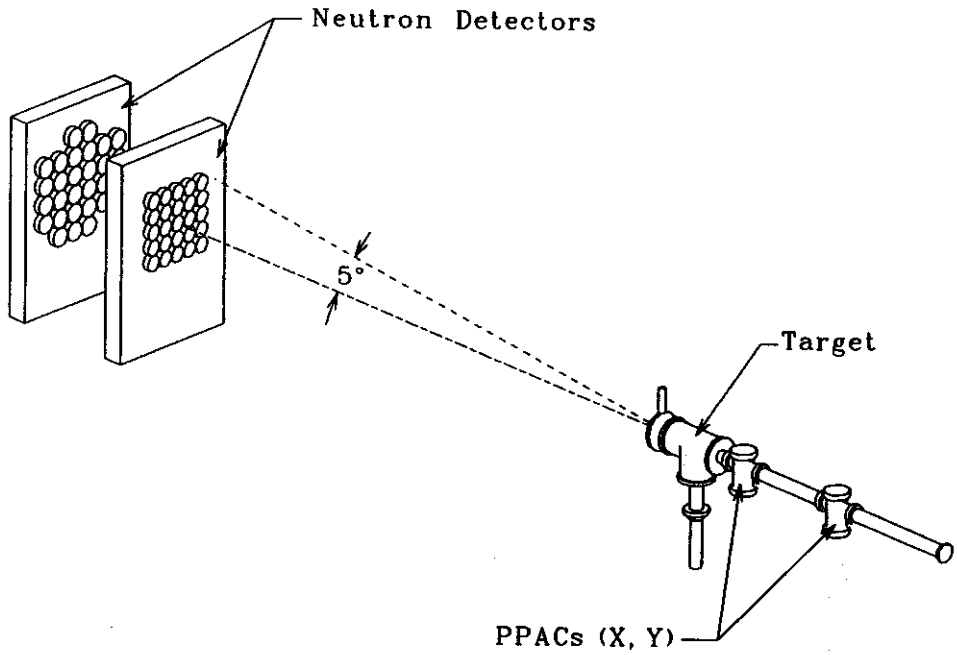

Figure 1: A view of an experimental layout for the neutron detector arrays. Adapted from [1].

scintillator. To detect a neutron, we observe the scintillation generated by an energetic charged particle produced by an interaction between the neutron and a hydrogen or carbon nucleus. In our energy range (~30MeV) the most probable interaction is elastic scattering by the hydrogen. Reactions with the carbon (e.g. C(n,p)N and C(n,n')3α) also produce detectable events, but the elastically scattered carbons do not have enough recoil energy to be detected. Since a neutron event is detected through a random scattering process, the event's luminosity in the scintillator is not sufficient for determining the neutron's energy. Therefore, we use the neutron's time of flight to measure its energy.

The cylindrical detectors used in the ^{11}Li experiment have a detection efficiency for a single neutron of about 10 percent. To detect two neutrons in coincidence, the efficiency is about 1 percent. One of the

drawbacks with an array of cylindrical detectors is that the minimum dead space between the detectors is 50% of the total area covered by the array. By whatever factor the dead space could be eliminated, the total efficiency for 2-neutron detection would improve by that factored squared. With the very low beam intensities of ^{11}Li available, the experimenters closely packed the detectors to minimize the dead space and obtain the most efficiency possible for low values of ^{11}Li breakup energy. The small solid angle of the array limited the breakup energy they could observe. They placed the 54 detectors in two arrays, subtending roughly the same solid angle, making it possible to detect neutrons that were collinear.

The second array sees some neutrons that have been scattered in the first array. If the interaction in the forward array was with the scintillator, and it made a detectable signal, the event is called crosstalk. Most of these events can be identified and corrected off-line. Unfortunately, there is no means of identifying events where the neutron scatters off the non-scintillator material (e.g. scintillator housing, lightpipe, PMT, base). We can only attempt to correct the data for this effect by using elaborate simulations [1]. For the detectors used, only 30% of the mass was scintillator material.

If we are to construct a new detector for this experiment, there are four characteristics we can hope to improve. First, we can increase the area covered, allowing the study of larger breakup energies. Second, we can attempt to reduce the dead space to increase the efficiency. Third, we can try to reduce the photomultiplier tube (PMT) to scintillator volume ratio, reducing the detector's cost. Fourth, if we make the scintillator housing more efficient in its mass compared to scintillator mass, we will reduce the amount of undetectable secondary scattering.

Our solution is to replace the cylindrical detectors with a "wall" of long, narrow, rectangular cells of scintillator (see Figure 2) viewed at each end by a PMT. This arrangement greatly decreases

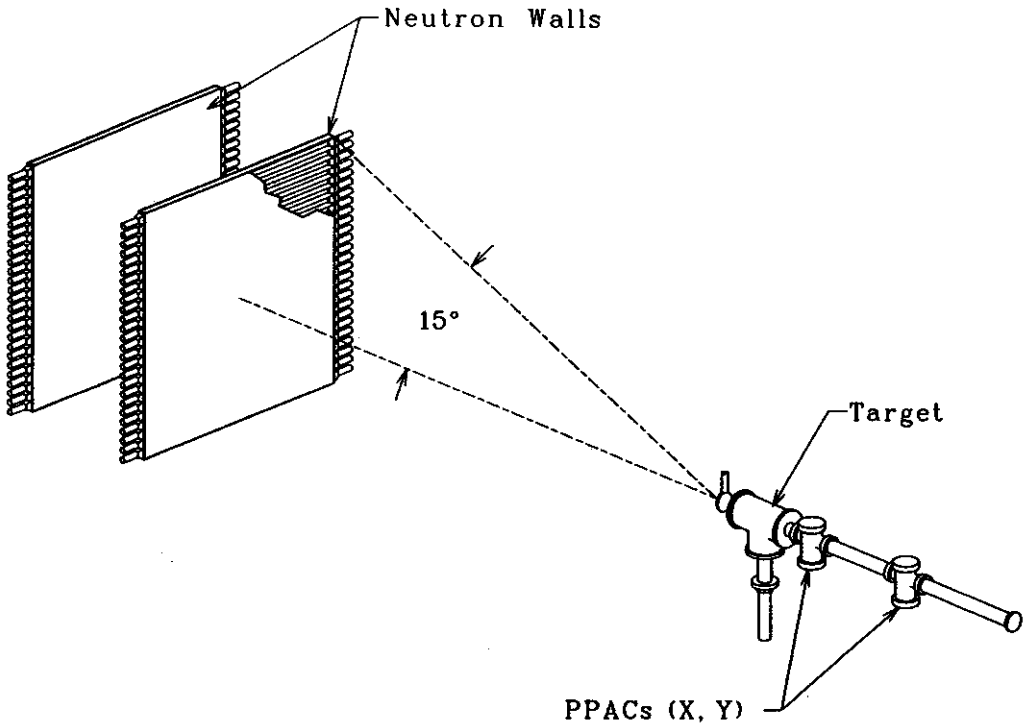

Figure 2: Schematic layout of the Neutron Wall detector.

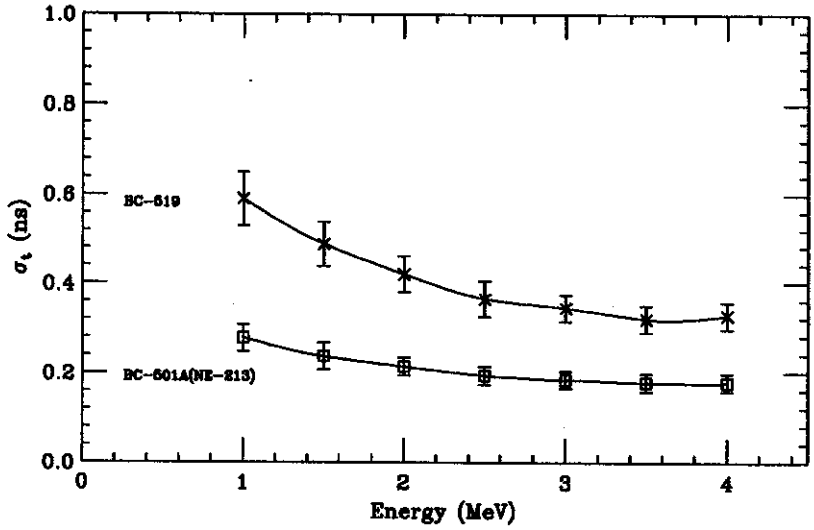

Figure 3: Time resolution as a function of energy for BC-519 and NE-213 in a small 3 inch long by 2-inch diameter cylindrical detector. σ_t is the width parameter of a Gaussian fitted to the time difference spectrum obtained from PMT's at opposite ends of the detector.

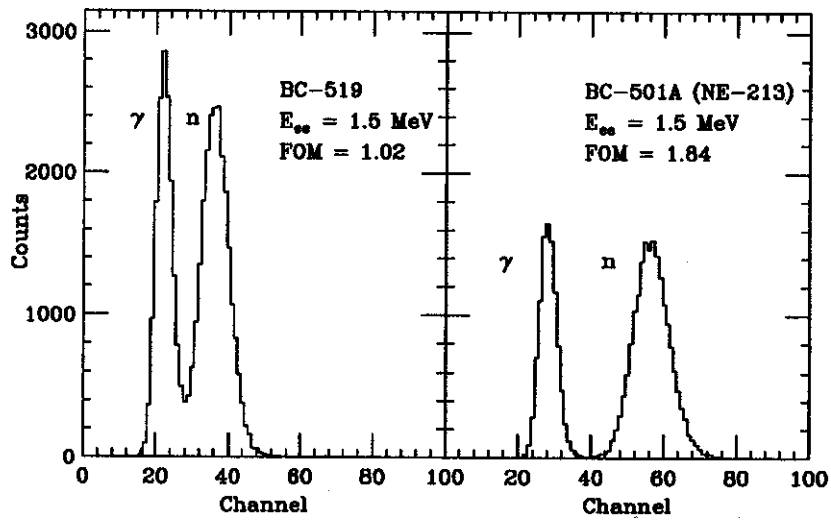

Figure 4: An example of n-γ discrimination in BC-519 and NE-213 for an electron equivalent energy of 1.5 MeV showing the corresponding figure-of-merit values. The graphs show intensity vs. pulse height.

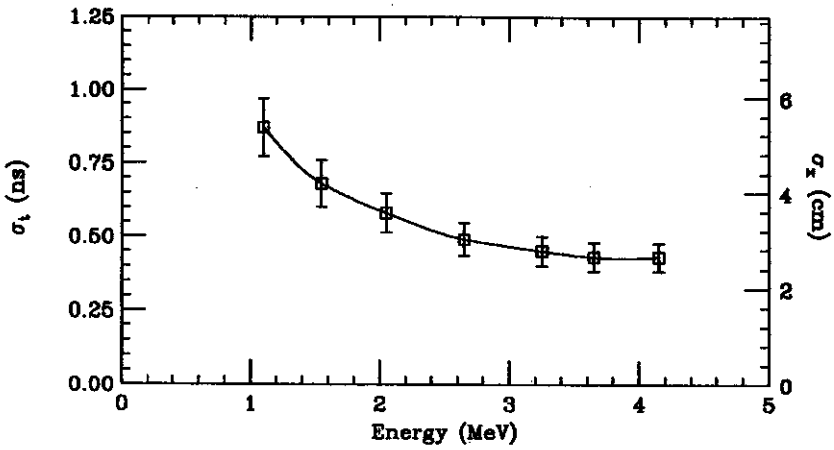

Figure 5: Time and Position resolution vs. pulse height at the center of a two-meter-long scintillation counter. σ_t and σ_x are the width parameters of a Gaussian fitted to the time difference spectrum obtained from PMT's at opposite ends of the detector, scaled for the appropriate units, ns and cm, respectively.

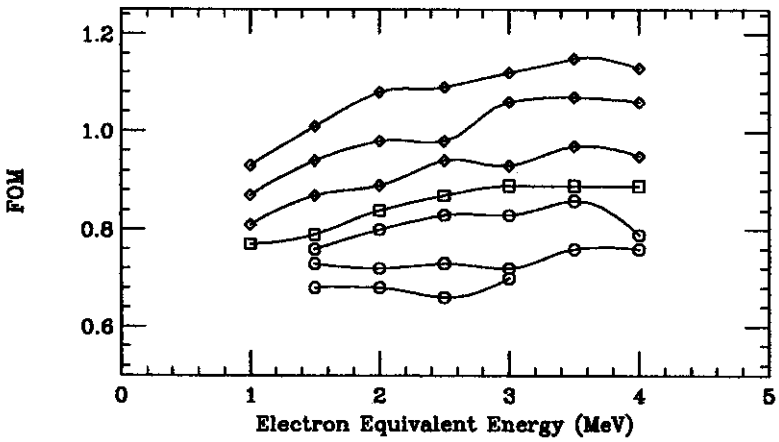

Figure 6: Figure-of-merit vs. pulse-height measured at 7 positions along the detector spaced 20 cm apart. The square data points represent measurements at the center of tube, diamonds positions closer to the PMT and circles farther from the PMT.

the PMT/scintillator-volume ratio. It also greatly decreases the dead space and significantly reduces the secondary scattering by non-scintillator material. Making each cell 2 meters long greatly increases the area covered, allowing larger breakup energies to be observed. Lastly, with good position resolution along the length of the cell and by making the height, perpendicular to the beam direction, smaller than the diameter of the cylindrical detectors, the angular resolution is improved. Each cell has to meet three criteria: good position resolution, good energy resolution, and good n-γ, pulse-shape resolution.

Position resolution and energy resolution are both functions of the time resolution of the cell. The position is determined by measuring the time difference between the PMT signals. The energy, as measured by time-of-flight, is determined from the sum of the times. The resolution of both measurements is determined by adding in quadrature the resolution of each time signal. For the neutron wall to be a viable option, the time resolution must be less than 1 ns and the position resolution must be better than the 5 inch diameter of the cylindrical detectors.

Because of induced radioactivity during an experiment, not all gamma-rays can be identified from their timing. Consequently, each cell must have an n-γ, pulse-shape discrimination ability. For our purposes, the cell's pulse-shape discrimination must be acceptable down to pulse sizes of approximately 1 MeV electron equivalent energy. There are two commercially available scintillators that advertise n-γ discrimination capabilities. The most commonly used scintillator is a xylene solution developed by the former Nuclear Enterprises, Inc., called NE-213 (from Bicron, Inc., BC-501A). The other scintillator is a mineral oil solution developed by Bicron, Inc., called BC-519. Aside from mineral oil being a safer compound with which to work, BC-519 offers a higher hydrogen to carbon ratio with roughly the same number of carbons per volume. The extra hydrogen does two things; it adds a little bit of efficiency and it helps in the detection of crosstalk events. Unfortunately, it has a lower light output than the NE-213; to compensate for the lower output, some sacrifice in time resolution or efficiency must be made. Also, BC-519's n-γ discrimination capability has not been well studied. The tradeoffs between these scintillators led us to complete an in-depth comparison of NE-213 and BC-519.

Measurements of BC-519 and NE-213 were made in two different detectors: a 3-inch long, 2-inch diameter cylindrical detector, and a 2-meter long, 2-inch diameter cylindrical detector. Both detectors were viewed at each end by a 2-inch Burle 8575 PMT. The time resolution was measured in both detectors by illuminating the scintillator with a collimated gamma-ray beam of 4.2 MeV. Figure 3 shows the time resolution as a function of recoil electron energy for the 3 inch long detector. The variation between the two scintillators is largely the result of BC-519's lower light output.

The n-γ discrimination is accomplished by comparing the charge integral of the total pulse to the charge integral of the pulse's tail [3]. A common measurement of the quality of discrimination is the so called figure-of-merit (FOM). It is defined as

$$\mathrm{FOM} = \frac{\text{Separation of n and } \gamma \text{ peaks}}{\Sigma(\text{FWHM of n and } \gamma \text{ peaks})}.$$

A value of 1 is considered good n-γ separation and larger values indicate better separation. Figure 4 shows an example of the FOM for 1.5 MeV electron equivalent energies from the 3-inch-long detector for both BC-519 and NE-213. Although the separation is quite good in both of these examples, it is clear that NE-213 is much better at discriminating between neutrons and gamma-rays. With the 2-meter cell, some events get farther from the PMT, the amount of light collected drops and the n-γ discrimination gets

worse. Even so, the NE-213 FOM is still acceptable at distance of 1 meter; the FOM for BC-519 is too badly degraded for events far (~1 meter) from the PMT. Consequently, we decided to use NE-213 in the final detector.

A number of prototypes were constructed and tested. The best design had the scintillator housed in a square Pyrex tube 183 cm long and with an approximately 5cm x 5cm cross section. At each end, a 2 inch Burle 8575 PMT was attached. The time and position resolution, measured by illuminating the cell with a 4.2 MeV, collimated, gamma-ray beam, are shown in Figure 5. The results are shown as a function of recoil electron energy for events at the center of the cell. The left axis shows the time resolution and the right side shows the corresponding position resolution. The resolution is best for events at the center of the tube and gets worse towards the ends, but this is not a significant effect. Clearly, both position resolution and time resolution meet the necessary criteria.

The n-γ discrimination characteristics were measured by illuminating the entire cell with a PuBe source. The data were cut on the position and on the energy of the recoiling protons (expressed in electron equivalent energy). Figure 6 shows the FOM as a function of energy for 7 different positions along the tube, each spaced 20 cm from its neighbor. Since each PMT can independently determine if an event was a neutron or a gamma-ray, good discrimination is only needed from near a PMT out to the center of the cell. With this in mind, the n-γ discrimination capabilities are sufficient.

The results from the prototype are very encouraging. We feel we can extend the design to a complete detector which will cover an area of 2 meters by 2 meters. Such a detector will greatly increase our detection efficiency for large ^{11}Li breakup energies and will increase our overall detection efficiency. Also, the detector's's modular design will allow for a wide variety of neutron experiments at the NSCL. We plan to have completed the design by the end of the spring of 1994 and the completed detector by the end of 1994.

References

1. D. Sackett, K. Ieki, A. Galonsky, et al., Phys. Rev. C48, 118 (1993).
2. K. Ieki, D. Sackett, A. Galonsky, et al., Phys. Rev. Lett. (1992).
3. J.H. Heltsley, et al., Nuclear Instruments and Methods, A263 (1988).

TIME ANALYSIS IN THE MSU 4π ARRAY

J. Yee, A.M. Vander Molen, D. Craig, E. Gualtieri, S. Hannuschke, W.J. Llope, R. Pak, N. Stone, and G.D. Westfall

In the normal setup of MSU 4π Array, the relative time of flight of each particle with respect to the triggering signal gets recorded for the case of phoswiches and MWPCs.[1] The time difference between the RF and the triggering signal is also recorded. But this information was never used to obtain the velocity of a particle directly partly because we can get the energy value from the pulse height in the case of phoswich detectors. This is very difficult for the MWPCs, however. So, we devised a method to obtain the velocity using time information.

In fig.1, θ_{ff} is the folding angle of two fission fragments,[2] and v is the velocity of the faster of the two fragments. The solid line indicates the Viola's velocity for fission.[3] Data are from the reaction ^{40}Ar + ^{232}Th at 35 MeV/n. In target fission, v should be close to the solid line, while as more linear momentum is transferred, in other words as θ_{ff} becomes smaller, the v value should become bigger and more spread out.

Fig.1 shows good agreement both in the absolute value of v and the shape of the distribution.

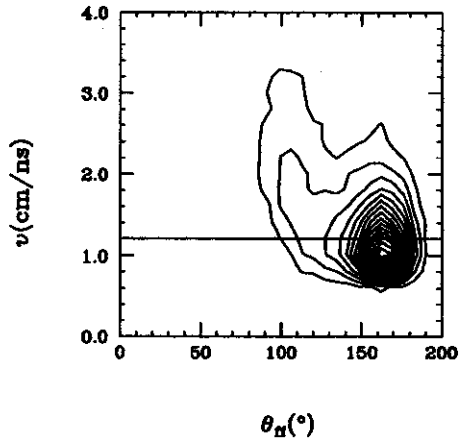

Figure 1: Velocity vs Folding Angle of the Fission Fragments

References

1. L'User's Guide to the MSU 4π Array
2. M. Conjeaud et. al., Phys. Lett. 159B, 244 (1985)
3. V.E. Viola et. al., Phys. Rev. C31, 1550 (1985)

A ZERO DEGREE DETECTOR FOR THE 4π ARRAY

N. Stone, D. Craig, E. Gualtieri, S. Hannuschke, W. Llope, A. Nadasen[a], E. Norbeck[b], R. Pak, J. Yee, D. Swan, A. Vander Molen, and G. Westfall

We have designed a "zero-degree detector" (ZDD) for the MSU 4π Array, which will cover the laboratory polar angles between $\sim 0.5^{\circ}$ and 1.5° . The detector will be made from two layers of fast scintillating plastic, and is designed to resolve fragment charges and energies via two methods. In the first, fast (projectile-like) fragments which pass through the first thin layer will be identified via $\Delta E/E$ measurements. In the second, slow-moving (residual) fragments which stop in the first layer will be identified via ΔE/Time-of-Flight (TOF) measurements.

Simulations have been performed using the code FREESCO, and the results (Fig. 1, bottom right) predict a nearly monotonic relation between the charges of fragments with $Z \gtrsim 3$ emitted in this angular region and the impact parameter of the collision. At lower incident energies (Fig. 1, bottom left),

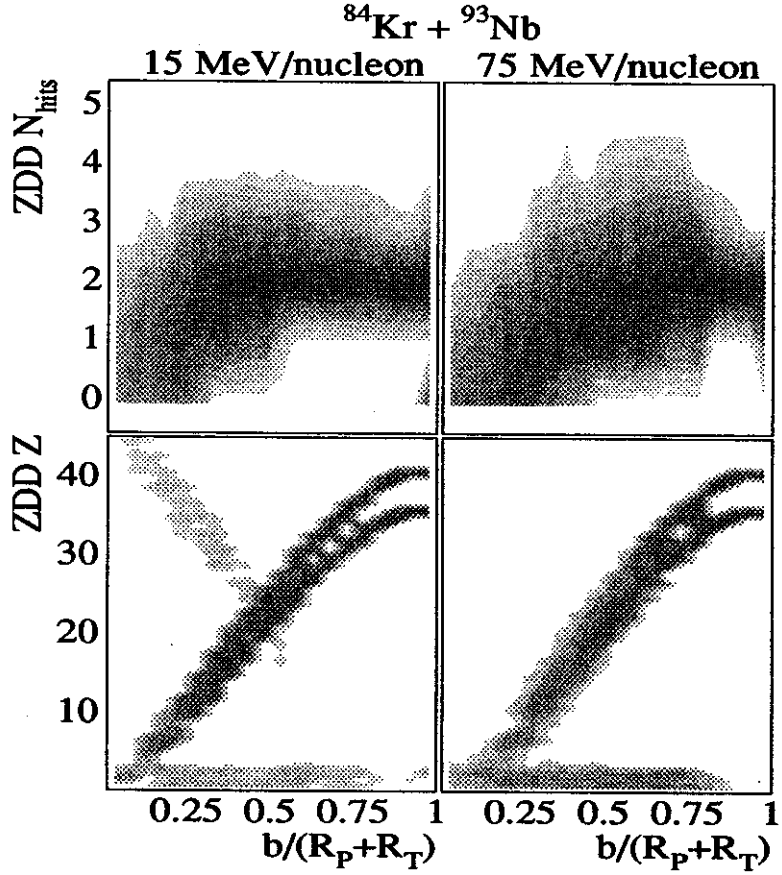

Figure 1: Results of FREESCO model calculations for 15 and 75 MeV/nucleon beams.

evaporation residues survive the disassembly, and the charges of such residues also show a monotonic dependance on the impact parameter. These residues will be distinguished from other large fragments by their TOF. Thus, the advent of a ZDD is expected to provide valuable information directly related to the impact parameter of observed collisions. This information is unaffected by the dynamics and statistical nature of the collisions, and hence provides a means of selection of impact parameter which

is alternative and complementary to, *e. g.*, centrality cuts based on global observables like the charged particle multiplicity or the total transverse kinetic energy.

The detector must be made from "fast" scintillating plastic (Bicron's BC404), due to its location in the beam. This was chosen for its fast decay time (1.8 ns) and high light output (68% Anthracine). The first (ΔE) layer of the detector will be 0.75 mm thick in the beam direction. Figure 2(a) is a plot of the fractional energy loss of fragments with varying incident energies in 0.75 mm thick scintillating plastic. This figure shows that particles with $Z \leq 15$ for KE/A $\geq$ 25 MeV will be transmitted through this first layer. The second (E) layer will be 30 cm thick, stopping all particles with KE/A $\gtrsim$200 MeV.

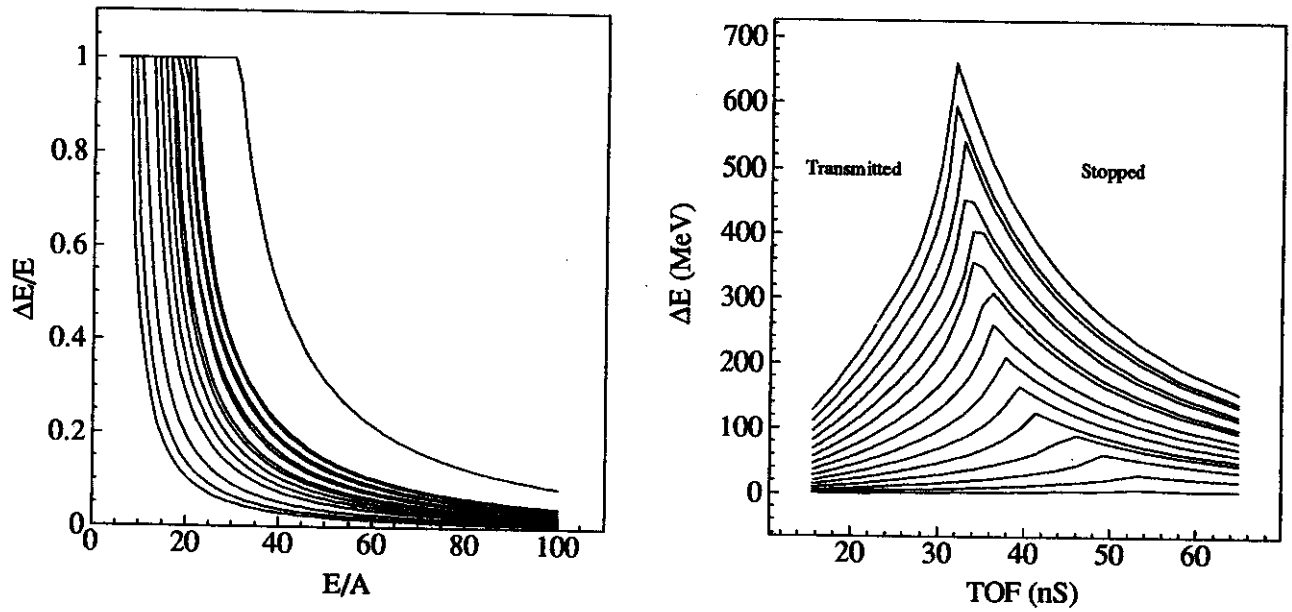

Figure 2: (a, left) The fractional energy loss of fragments (Z=1-15, and Z=36) in 0.75 mm scintillating plastic versus the incident energy. The "punch-in" energies are clearly seen here as those points where ΔE/E falls below 1. (b, right) Deposited energy, in 0.75 mm scintillating plastic, versus TOF, for a 3 m flight path, for fragments (Z=1-15).

These two layers will be optically isolated, enabling the use of all "fast" plastics, and each divided into 8 segments, for reasons which follow. As seen in Fig. 1(top frames), the fragment population of the ZDD can be as high as 4 particles per event, and is routinely as high as 2. Several fragments entering the ZDD may be emitted from the same moving source, causing correlations at the face of the ZDD. This degree of segmentation is thus necessary to minimize multiple hits in each segment.

The ΔE segments will be fitted with UVT light guides, which will be optically coupled to Phillips XP2262B photomultiplier tubes (PMTs). These are moderately fast, reliable PMTs, widely used in high-speed physics applications. The PMTs will operate in the negative HV mode for speed and pulse fidelity, and will be surrounded by μ-metal shields, to isolate them from electromagnetic interference. The thick segments will be directly coupled to the PMTs. There is a small hole in the center of the ZDD (for $0^\circ \leq \Theta \leq 0.5^\circ$) which will minimize the likelihood of extraneous hits from beam particles. Its size was calculated using typical emittances for beams extracted from the K1200 cyclotron which were delivered to the 4π vault. Figure 3 shows a cut-away view of the ZDD.

The ZDD must be placed far from the target (~3 meters), for the following reason. Meaningful TOF measurements require reliable start and stop times. One of these can easily be taken from the detector

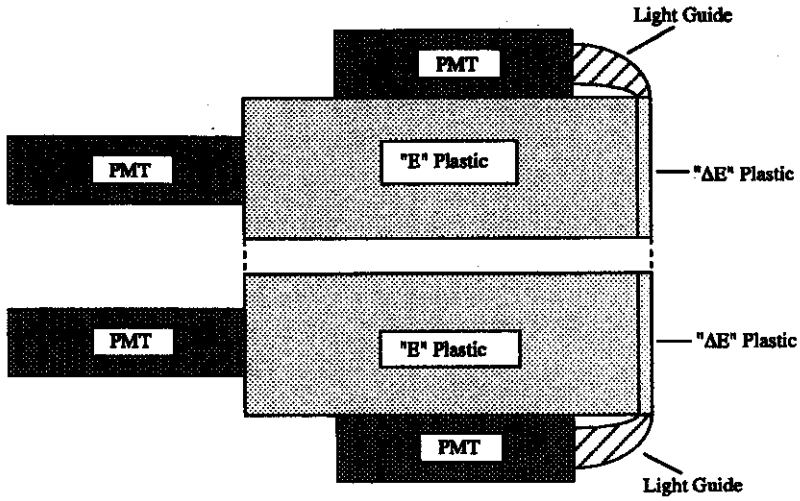

Figure 3: Cut-away diagram of the ZDD, showing placement of PMTs and light guides.

signal, while the other requires more care. One option is to run with a "start" detector at the entrance to the 4π Array, yielding a precise indication of the arrival time of a beam particle. This has the disadvantage of effectively introducing an additional target, showering the 4π Array with false hits, as shown in the past (exp. #92015). A second option, which we have chosen for this implementation, is to digitize the cyclotron RF signal, which is inherently correlated to the arrival of beam particles at the 4π vault, which come in "buckets." The width of these buckets, in time, is a measure of the strength of that correlation.

The width of a typical RF bucket is nominally 40°, in a 360° cycle. However, the cyclotron phase slits can be used to tune this to as low as 4°. For the beams proposed in experiment #93033 (^{84}Kr at 15 to 85 MeV/nucleon), such a width in RF corresponds to a timing width of $\lesssim 1.1$ ns. This improvement in timing resolution comes at a cost of intensity; by factors that range from 3 to 30. However, even with such intensity losses, it is predicted that the cyclotron will still be able to provide sufficient beam intensities ($\gtrsim 5$ p pA) for the requested beams. Based on energy loss and TOF calculations (see Fig. 2(b)) and these factors, the ZDD must be placed $\gtrsim 3$ meters from the target for adequate fragment charge resolution.

It will be necessary to build a separate vacuum chamber to house the ZDD. We have designed such a chamber which will allow horizontal and vertical positioning of the ZDD so as to center the detector on the beam axis. Misalignments of the beam can be as large as 0.6°. The current design for this chamber will meet the above requirements and, in addition, provide a free-standing, independently functional test-chamber. The inclusion of this chamber will require minor, but reversible, revisions to the existing beam line behind the 4π Array. Figure 4 shows the beamline as it will appear with those additions.

This design of the ZDD is a refinement of the one given in experimental proposal #93033, which was submitted to the NSCL Project Advisory Committee (PAC 16) and approved on December 7, 1993 for 168 hours of beam time.

a. University of Michigan, Dearborn
b. University of Iowa

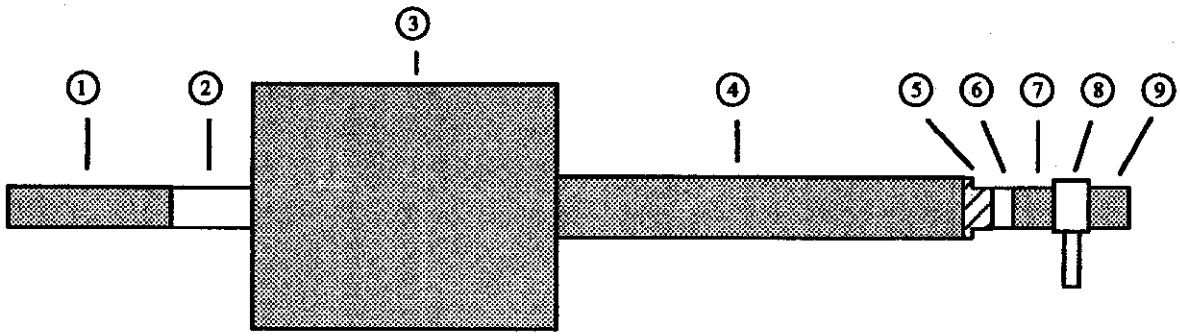

= Components in stock

= Components which can be purchased pre-made

= Components which will require hired labor and/or shop time

Component List

1. 4" Beam Tube
2. Bellows
3. Vacuum Chamber
4. 6" Beam Tube
5. ISO-160/ISO-100 Reducer
6. ISO-100/Marmon Adapter
7. ASA-6/Marmon adapter
8. Gate Valve
9. ASA-6/Custom adapter

Figure 4: Scale version of the modified exit beam line, with a description of components.

FIRST RESULTS FROM THE NEW HIGH RATE ARRAY FOR THE 4π ARRAY

R. Pak, W.J. Llope, D. Swan, J. Wagner, G.D. Westfall, D. Craig, E. Gualtieri,
S. Hannuschke, N. Stone, A.M. Vander Molen, and J. Yee

The forward array of the MSU 4π Array has been recently upgraded to a newly designed close-packed phoswich array called the High Rate Array (HRA) [1]. This configuration offers minimum dead area, good granularity over the subtended solid angle, and very high rate capabilities. The installation of the completed HRA occurred on schedule in December 93.

The HRA consists of three pentagonal rings of 10, 15, and 20 fast/slow plastic scintillators. The array spans polar angles from $\sim 2.9°$ to $\sim 18.0°$, subtending all solid angle between the Maryland Forward Array (MFA) and the rest of the 4π Array. This results in $\sim 95\%$ geometric efficiency for the entire detector system. A schematic view of how the HRA mounts forward of the 4π Array is shown in Figure 1.

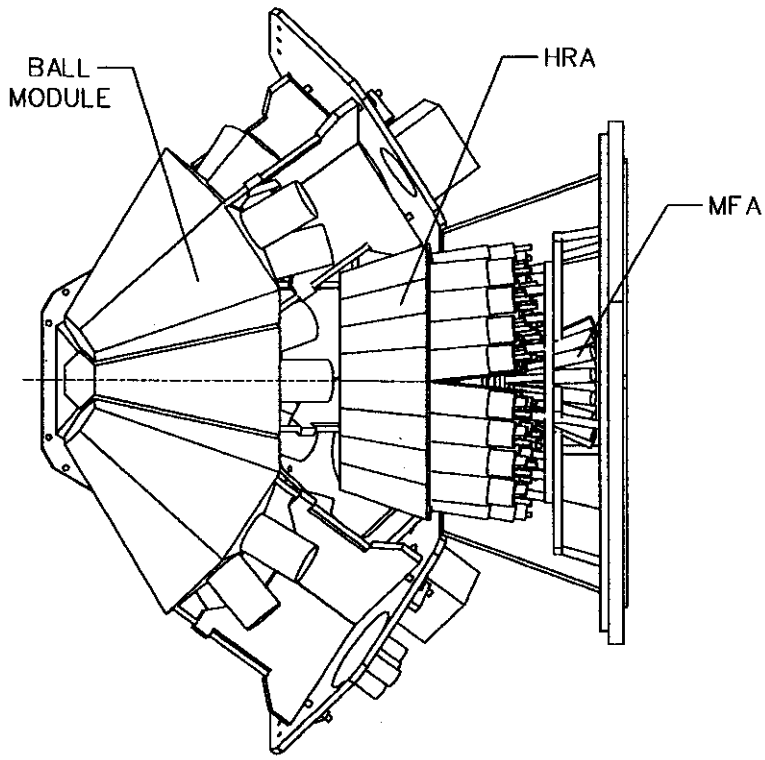

Figure 1: Schematic view of how the NSCL High Rate Array (HRA) mounts in the 4π Array between the Maryland Forward Array (MFA) and the modules in the main Ball.

A 45 element design was choosen so that no additional electronics would be necessary. The only investment was in scintillator plastic and the mechanical support structure. Machining was done at the NSCL, and all additional fabrication was carried out by the 4π Group.

The individual detectors are fast/slow plastic counters which measure E, ΔE, and time by the same technique presently used for the phoswiches in the rest of 4π Array [2]. The detectors are painted with an epoxy based paint pigmented with TiO_2 and are glued together in five wedges of nine detectors.

Only this epoxy layer and a thin reflective foil (to insure no cross talk) separate the detectors, effectively minimizing the dead area. A 4.5 kÅ-thick (0.12 mg/cm^2) aluminum layer is evaporated onto the front face to minimize light leaks while maintaining a low particle kinetic energy threshold. The array is positioned as close to the target as would allow a 5 cm. diameter phototube to be optically coupled onto the back of each detector, which is about 71 cm.

Figure 2 shows a ΔE vs. E spectrum for one of the HRA detectors in the innermost ring closest to the beam axis (polar angle to the center of this detector $\sim$ 5.4°). The data shown are a compilation of samples at beam energies from 35 MeV/nucleon to 115 MeV/nucleon in 10 MeV/nucleon steps for the system ^{40}Ar+^{45}Sc. Clearly there is charge resolution up to Z = 17. Although not apparent from this Figure,

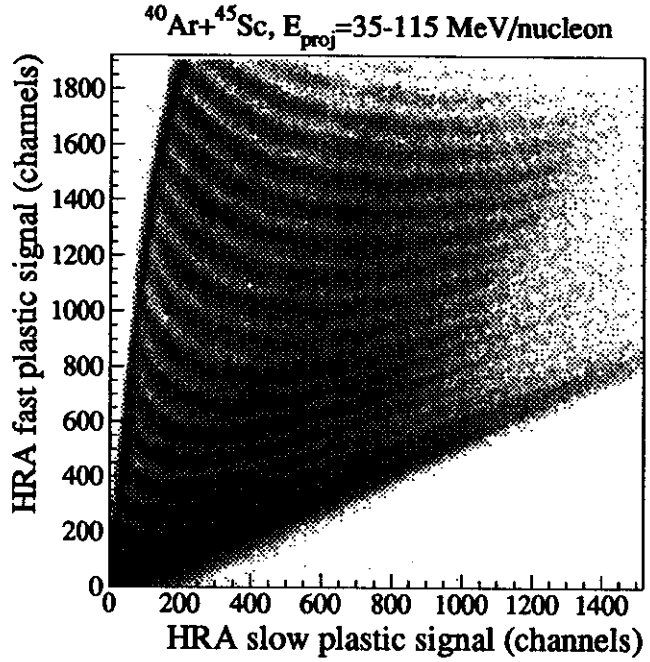

Figure 2: ΔE vs. E spectrum for HRA detector at an angle $\sim$ 5.4° off the beam axis.

there is also p, d, and t resolution for the HRA detectors. The spectrum shown also demonstrates the stability of the HRA phoswiches against drifts in gain since these data were taken over a period of about a week. Methods for treating the slight saturation in the HRA signals for above Z $\sim$ 13 is currently under investigation.

The High Rate Array has already been used in three experiments, which were collaborations with Hope College, the University of Maryland, and SUNY at Stony Brook. The calibration and analysis of these data is in progress. Four additional experiments which will utilize the HRA have recently been approved and are scheduled be to run in the coming year.

References

1. R. Pak, W.J. Llope, D. Swan, J. Wagner, G.D. Westfall, D. Craig, E. Gualtieri, S. Hannuschke, N. Stone, A.M. Vander Molen, and J. Yee Annual Report NSCL/MSU (1992).
2. G.D. Westfall, J.E. Yurkon, J. van der Plicht, Z.M. Koenig, B.V. Jacak, R. Fox, G.M. Crawley, M.R. Maier, B.E. Hasselquist, R.S. Tickle, and D. Horn, Nucl. Inst. and Meth. A238, 347 (1985).

DETECTION EFFICIENCY OF BaF_2 FOR 15 - 150 MEV NEUTRONS

R.A. Kryger, A. Azhari, E. Ramakrishnan, M. Thoennessen, and S. Yokoyama.

As part of our program to study neutron-unbound light nuclei via sequential neutron decay spectroscopy[1], we have evaluated the neutron detection efficiency of BaF_2 scintillation detectors. BaF_2 has several key properties which make it a potentially useful neutron detector. These include fast light response, which allows subnanosecond timing, as well as the capability to distinguish neutrons from photons via pulse-shape discrimination (PSD)[2]. Unfortunately, there is very little information available regarding the neutron detection efficiency of BaF_2. Only Kubota, *et al.* [3] have reported efficiency results for neutrons with energies above 10 MeV in coincidence with pulse-shape identification. Furthermore, their data only covered neutron energies between 15 and 45 MeV. We have completed an expanded measurement of neutron efficiency for neutron energies between 15 and 150 MeV using a 25 cm long hexagonal BaF_2 crystal detector with a 5.9 cm edge-to-edge front face. These detectors are available at the NSCL and are used primarily for high-energy γ-ray studies.

The BaF_2 efficiency was measured relative to the efficiency of a 7.6 cm long cylindrical NE213 liquid-scintillator detector with 12.7 cm diameter. Neutrons over a broad energy range were produced by using a pulsed 70 MeV/A ^{14}N beam from the K1200 cyclotron incident on a 1.3 cm thick brass beam stop. The two neutron detectors were placed at 23° with respect to the beam axis, slightly above and below the horizontal plane. A thin plastic scintillator detector was placed in front of the two detectors to veto incident charged particles. Data was taken at two detector distances (5.3 m and 2.4 m) in order to cover a broad range of neutron energies. For each detector, neutron time-of-flight (TOF) and pulse-shape signals were recorded. Offline, the neutron energy was determined from the TOF relative to the peak in the time spectrum associated with γ-rays emitted from the target. The FWHM of the γ-peak, providing a measure of the time resolution, was 1.3 ns for the BaF_2 detector and 0.9 ns for the NE213 detector. Neutron/γ-ray discrimination was achieved using standard techniques. The neutron discrimination required a 7.0 MeV-electron equivalent (MeV-ee) light threshold for the BaF_2 detector.

The TOF spectra for the NE213 detector showed a large background in the region of interest due to low-energy neutrons from the previous beam burst. By requiring a 3.9 MeV-ee light threshold on the NE213 events, this background could be eliminated in the 2.4 m data, but it was not practical to raise the threshold high enough to eliminate this effect in the 5.3 m data. A similar background was also seen in the 5.3 m data for the BaF_2 detector. We used the measured TOF spectrum in the 2.4 m position to subtract out this low-energy background in the 5.3 m data. This was done for both the NE213 and BaF_2 detectors. The BaF_2 detector efficiency was computed as a function of TOF according to the relationship

$$\epsilon_{\mathrm{BaF}}(t) = \frac{\left(\frac{dY_{\mathrm{BaF}}(t)}{dt\Delta\Omega_{\mathrm{BaF}}}\right)}{\left(\frac{dY_r(t)}{dt\Delta\Omega_r}\right)\left(\frac{1}{\epsilon_r(t)}\right)} \qquad (1)$$

where $dY_{BaF}(t)/dt\Delta\Omega_{BaF}$ and $dY_r(t)/dt\Delta\Omega_r$ are the time spectra for the BaF_2 and NE213 reference detectors transformed to the same neutron flight path distance and normalized by solid angle, and $\epsilon_r(t)$ is the absolute neutron detection efficiency of the NE213 detector for neutrons with energy corresponding to

time-of-flight t. The NE213 detector efficiency $\epsilon_r(t)$ was calculated using the Monte Carlo program of Cecil *et al.*[4] which was written for modeling hydrocarbon scintillator response to neutrons. The calculation incorporated the NE213 scintillator geometry and the 3.9 MeV-ee light threshold. The BaF_2 efficiency determined from this analysis for both the near (squares) and far (circles) detector positions is shown in Figure 1 as a function of neutron energy. The error bars reflect the statistical uncertainties in the TOF data and a ±5% uncertainty assumed for the calculated NE213 detector efficiency. The effect of the 1 ns time bins transformed to neutron energy can be seen in the spacing of the data along the x-axis. The solid and dashed lines in Figure 1 show calculated efficiency functions for a cylindrical NE213 detector with the same length and volume as the hexagonal BaF_2 detector used in the present measurement. The two lines correspond to a light threshold of 7.0 MeV-ee (solid) and 0.5 MeV-ee (dashed) to illustrate the effect of the light threshold. Since the PSD between neutrons and photons in NE213 can typically be achieved well below a 7.0 MeV-ee light threshold, the second calculation with a 0.5 MeV-ee threshold is a more practical efficiency curve to compare with the BaF_2 results. The BaF_2 neutron efficiency is seen to drop substantially below 50 MeV. This effect results primarily from the pulse shape discrimination requirement and the related 7.0 MeV-ee light threshold. Above 70 MeV neutron energy, the BaF_2 efficiency is found to surpass that of a comparable NE213 detector. Furthermore, the BaF_2 efficiency continues to increase with neutron energy while the NE213 efficiency is slowly decreasing. These results suggest that BaF_2 is a highly suitable neutron detector for neutrons above ~ 50 MeV.

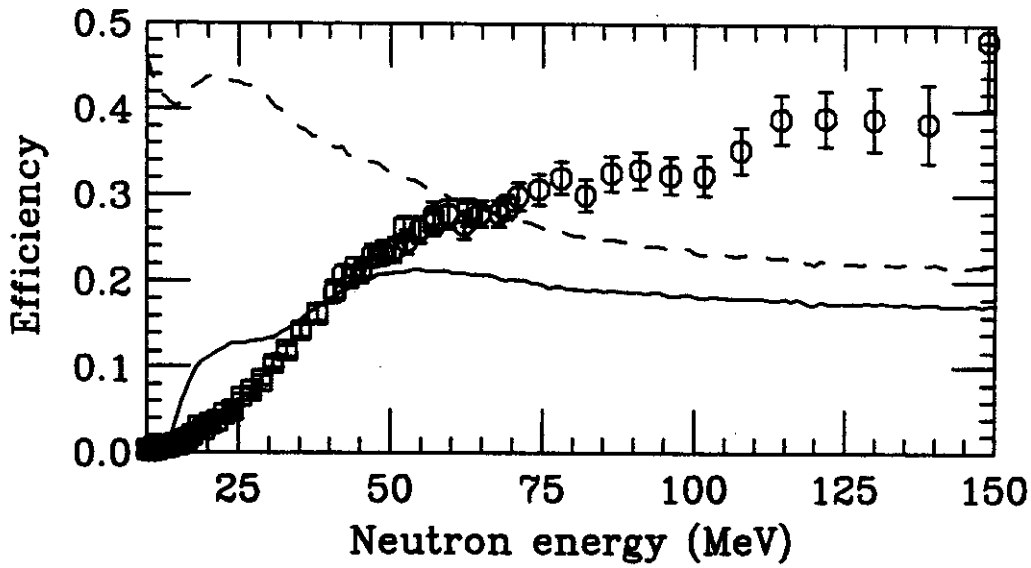

Figure 1: The absolute neutron detection efficiency of the BaF_2 detector as a function of neutron energy for the 2.4 m data (squares) and the 5.3 m data (circles). The solid and dashed lines correspond to calculated efficiencies for a cylindrical NE213 detector of the same length and volume as the hexagonal BaF_2 detector with light thresholds of 7.0 and 0.5 MeV-ee, respectively.

References

1. R.A. Kryger, *et al.*, Phys. Rev. C47, R2439 (1993).
2. T. Matulewicz, *et al.*, Nucl. Instrum. Meth. A274, 501 (1989).
3. S. Kubota, *et al.*, Nucl. Instrum. Meth. A285, 436 (1989).
4. R.A. Cecil, *et al.*, Nucl. Instrum. Meth. 161, 439 (1979).

ENERGY CALIBRATION OF MINIBALL-CSI DETECTORS

C.Schwarz, W.C. Hsi, M.J. Huang, D.R. Bowman, D.R. Kim, W.G. Lynch, L. Phair and M.B. Tsang

Introduction

The MSU Miniball array is a compact 4π fragment detection array to study Multifragmentation in intermediate and high-energy nuclear reactions. It consists of 188 detectors arranged in 11 rings, θ_{lab}=9°-160° around the beam axis covering 89% of 4π in solid angle. Each detector is composed of a 40 μm thick plastic scintillator foil and a 2 cm thick CsI(Tl) crystal selected for good scintillation uniformity. The detectors are read out by photomultiplier tubes. Elemental identification up to Z≈18 and isotopic identification of H and He nuclei is achieved by exploiting pulse shape discrimination techniques. Thresholds for particle identification range from E/A≈1.5 MeV for alpha particles to E/A≈3 MeV for Ca ions. Detailed information about the Miniball array can be obtained from Ref. 1.

Energy response of CsI(Tl) Crystals

The light output of CsI(Tl) crystals to various charge particles has been previously studied with light charged particles and heavy ions [2-5]. The nonlinearity of the light output of CSI(Tl) crystals increases for particles of lower energies and high atomic numbers. At energies above 5-6 AMeV, the light output shows quite linear response. In Ref. 4, the light output L of the CsI(Tl) crystals used in the Miniball detector was parameterized as

$$L(E,Z) = \alpha(Z)E + \beta(Z)\left[e^{-\gamma(Z)E} - 1\right], \qquad (1)$$

where α, β, and γ are parameters as function of charge **Z**, and **E** is the energy loss in the CsI(Tl) crystal [2]. This functional form is consistent with previous measurements [2,5,6]. It reproduces the nonlinear behavior of the CsI(Tl) light output in the low energy region and the linear behavior at higher energies up to E≈25 AMeV.

In most experiments, additional calibration points can be obtained from charge particles that punch through the 2cm long CsI(Tl) crystals since the energy loss for known fragments in the crystal can be calculated. These additional high energy data points, however, cannot be described by Eq. (1), which over predicts the light output by 20±5% for α-particles that punch through the CsI crystals. The discrepancy correlate with the gain of the individual detectors used. For simplicity and convenience, we have chosen the proton punch-through channel, 75 MeV for the Miniball as a measure for the gain of the photomultiplier. For reactions with incident energies above 50 MeV/A, proton punch through's can be obtained routinely for detectors forward of 150 degree, thus allowing global energy calibrations for the Miniball detectors with minimum efforts.

Saturation effect of photomultipliers

The electrical signal from the dynodes of a photomultiplier is not a linear function of the light seen by the photo cathode. Depending on the gain of a photomultiplier the multiplication factor for the last dynodes is decreased due to space charge limitation [8]. In order to understand this effect we bombarded low intensity beam directly into 10 different Miniball detectors with ^{6}Li, ^{12}C, and ^{18}O beams ranging from E/A=22 to 80 MeV. Fig.1 shows the fractional deviation of the light output predicted by Eq. 1 from the observed light output. Here, the light output is expressed as the normalized QDC channel. The fractional deviation is defined as

$$f = \frac{Ch\# - L(E,Z)}{L(E,Z)}, \qquad (2)$$

where Ch# denotes the measured QDC-channel # for a fragment with charge Z and energy E, respectively. For the ^{12}C fragments, the data were fitted with a straight line shown in the upper panel of Fig. 1. The same fit also agrees well with the ^{6}Li data (see lower panel). By combining calibrations obtained in previous Miniball experiments, similar agreement was achieved for the fragments ^{4}He, ^{6}Li, ^{10}B, ^{12}C, ^{14}N, ^{16}O, and ^{20}Ne, measured in this and other experiments [4,6,7].

Correction for the saturation effect

In order to correct for saturation effects one wants to get a corrected QCD-channel number, CH#$_{corrected}$ which is as close as possible to the value predicted by Eq. 1. Hence one can write Eq. 2 as

$$f(CH\#) = \frac{CH\# - CH\#_{corrected}}{CH\#_{corrected}}, \qquad (3)$$

and write the corrected QDC-channel as

$$CH\#_{corrected} = \frac{CH\#}{1 + f * CH\#}. \qquad (4)$$

The spreading of data points from 10 different Miniball detectors shown in Fig. 1 is of the order of 10-15%. This uncertainty can be traced to the accuracies of some of the electronic components used in the photo-multiplier base and represents the systematic error associated with using these universal relationships for all Miniball detectors.

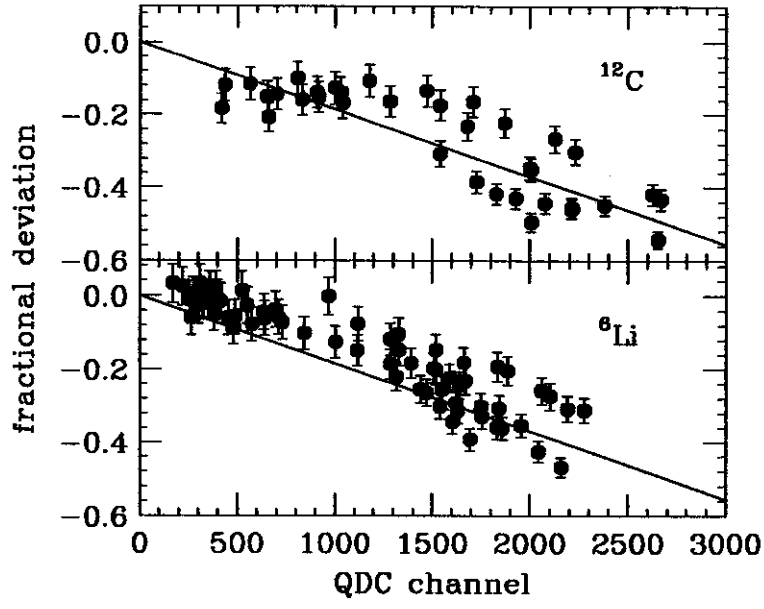

Fig 1: Fractional deviation of the light output of Miniball detector CsI(Tl) crystals as defined in Eq 1 as a function of the normalized QDC channel. The upper (lower) panel shows the results for ^{12}C(^{6}Li) fragments, respectively.

To demonstrate the correction effect we calibrated the light output of detectors for ^{4}He and ^{12}C fragments. As seen from Fig. 2 the correction becomes more important with increasing QDC-channel. While the ^{12}C data at 250 MeV are corrected by about 10%, the correction for the ^{4}He data at 300 MeV is 30-40% according to the higher light output.

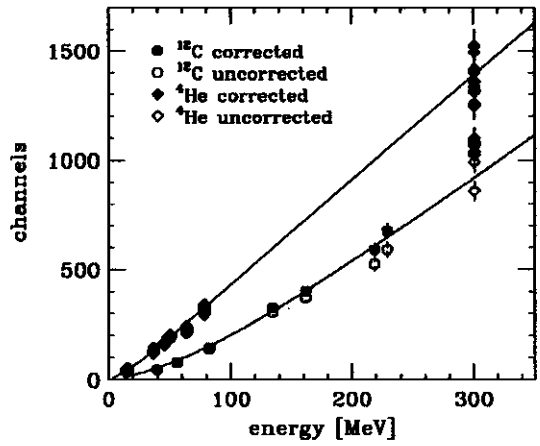

Fig. 2: Calibration curves for ^{4}He and ^{12}C fragments (solid data points) including the saturation correction. The open symbols show the uncorrected data points.

Energy calibration

Since α, β, and γ in Eq. 1 are dependent on the fragment charge Z, it is advantageous to find a smooth parameterization of each parameter as a function of the fragment charge. Hence, a calibration for fragments can be found which are not measured. Similar to Colonna et al. [5] we have chosen

$$\alpha(Z) = a_1 + a_2 e^{-a_3 Z}$$
$$\beta(Z) = b_1 - b_2 e^{-b_3 Z}$$
$$\gamma(Z) = c_1 + c_2 e^{-c_3 Z} \qquad (5)$$

Table 1: The values of a_i, b_i and c_i

χ^2/n = 3.27	i=1	i=2	i=3
a_i	1.339E-2	5.925E-3	3.846
b_i	229.7	5.039E-3	1.967E-4
c_i	0.4142	4.995	7.824E-2

The light fragments ($Z \leq 2$) could not be fit by a smooth parameterization (Eq. 5), here α, β, and γ were fit as single quantities but in connection with the other 10 parameters to have a consistent detector normalization. Hence the total number of fitted parameter increased to 13. The parameters were found by minimizing χ^2 with respect to the ^{12}C calibration curve. For detectors for which no ^{12}C data were available, the ^{4}He data were normalized to the corresponding calibration curve. The values of a_i, b_i and c_i are shown in Table 1 for fragments with Z/A=0.5. The saturation correction factors, according to Eq. 2, were fitted by $f=1.85\times10^{-4}$ for the Miniball as shown in Fig. 3 and its insert.

An additional constraint was applied to the fit not to allow the fitted curves to cross. For clarity, multiple calibration data points for the same energy and fragment charge were averaged with the spread of the data

indicated by the error bars. For energies larger than 30 MeV per nucleon, the calibration shows an accuracy of 10-15% and the accuracy improves to 5-10% at lower energies. The insert of Fig 3 shows the fit for various fragments more clearly. While most of the fragments follow the predicted systematic trends, both the ^{6}Li and ^{10}B particles (crosses) seem to deviate from the calculated curves. As most of these data have been taken from various experiments analyzed by different people at different times, a consistent set of data for these two elements would be desirable to understand the observed deviation and to establish a systematic trend.

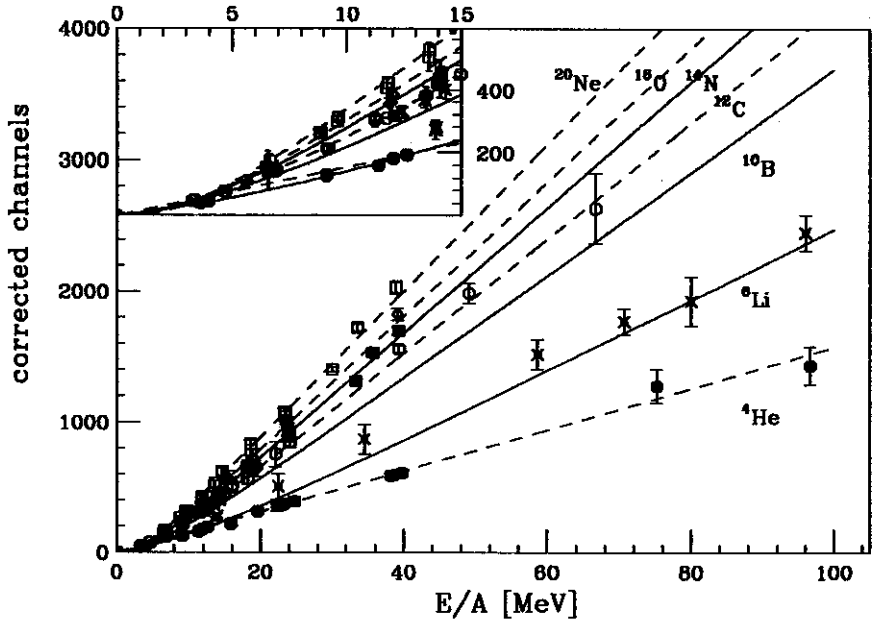

Fig. 3: Calibration data for ^{4}He(solid circles), ^{6}Li (open fancy crosses), ^{10}B(crosses), ^{12}C (open circles), ^{14}N (solid squares), ^{16}O (open diamonds) and ^{20}Ne(open squares). The lines are fits to the data (solid lines for odd charge elements, dashed for even charge elements).

Even though the Miniball array contains CsI crystals from different manufactors [1], within 10-15%, all the CsI detectors have very similar light response independent of the origin of the crystals. This allowed the energy calibration of all the Miniball detectors with the algorithm outlined above.

References

1. R.T. De Souza et al., Nucl. Instr. and Meth. **A295** (1990) 109.
2. A.R. Quinton et al., Phys. Rev. **115** (1959) 886.
3. J. Alarja et al., Ala86, Nucl. Instr. and Meth. **A242** (1986) 352.
4. Y.D. Kim, thesis, Michigan State University, 1991.
5. N. Colonna, Nucl. Instr. and Meth. **A321** (1992) 529.
6. E. Valtonen et al., Nucl. Instr. and Meth. **A286** (1990) 169
7. G. Peaslee et al., submitted to Phys. Rev. C (1994) R2271
8. J.B. Birks, The Theory and Practice of Scintillating Counting, Pergamon Press, Oxford, 1st edition, 1964, p. 120ff

NEUTRON YIELD AND SPECTRA MEASUREMENTS FOR SHIELDING ANALYSIS USING STOPPED BEAMS OF ^{4}He, ^{12}C AND ^{16}O AT 155 MeV PER NUCLEON

G.I. Britvich[a], A.A. Chumakov[b], R.M. Ronningen, and R.A. Blue

The K1200 cyclotron at the National Superconducting Cyclotron Laboratory is designed to accelerate ions of mass 2 through 238 to energies between 100 and 200 MeV per nucleon. The proposed coupling of the K500 and K1200 cyclotrons will provide ion beams having intensities up to one particle microampere for the lighter ions. Beams with these characteristics produce copious amounts of penetrating radiation, the most important being neutrons. Therefore, there are significant radiation issues. To assess current and future radiation shielding needs we have very recently measured neutron yields and energy spectra for ^{4}He, ^{12}C, ^{16}O ions at 155 MeV/u stopping in a thick target. Measurements were made inside and outside of concrete shielding walls using a set of Bonner spheres. The preliminary results for ^{12}C are discussed below.

Data for neutron production from ions heavier than helium and having energies near 200 MeV are relatively scarce. Neutron angular and energy distributions for a 710-MeV helium beam stopping in targets of water, carbon, steel, and lead have been measured [1] by Cecil et al. Time-of-flight techniques were used. Tuyn et al.[5] have carried out measurements of neutron production from a beam of ^{12}C, having an energy of 86 MeV per nucleon and stopping in an aluminum target. They measured the yields, energies, and angular distributions of the neutrons using activation methods.

In previous annual reports we have described a simple, phenomenological model which nicely reproduces the data of Cecil et al. The model treats projectile fragmentation and thermal sources of neutrons. The agreement between the data and the calculations was found to be reasonably good, considering the model's simplicity. Fig. 1 shows a comparison between the model and Tuyn et al.'s measurements of neutron yields. The largest disagreement is at zero degrees, where the measured yield is a factor of 4.3 larger than calculated. None-the-less, the agreement is also reasonably good.

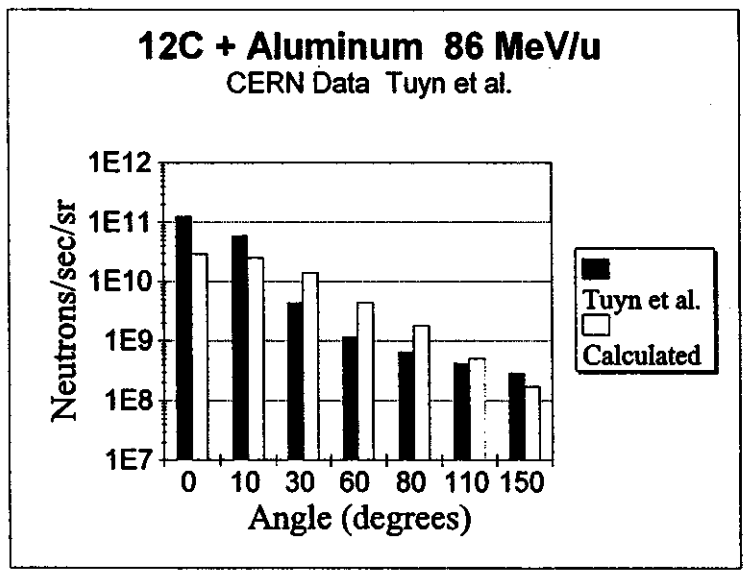

Figure 1: Model calculations compared to the data of Tuyn et al. for a beam of ^{12}C having an energy of 86 MeV/nucleon stopping in an aluminum target.

To further test this model's "source term," and to test our calculations of shielding we did two experiments. First ^{12}C, then ^{4}He and ^{16}O ions having 155 MeV per nucleon were stopped in the medium acceptance pot of the A1200. The Faraday cup, constructed of "Hevimet," an alloy of tungsten and copper, was used as the stopping target. Neutron flux measurements were made at four points inside the Analysis Hall and seven points outside of the Analysis Hall, using a set of Bonner spheres. The sphere diameters were 2, 3, 5, 8, 10, and 12 inches. The 12 inch and five inch spheres were used for most of the points. The full set of spheres was used at two points, one inside and one outside the shielding, both points having a common angle of 94 degrees with respect to the beam. Similar measurements were made using ^{4}He and ^{16}O beams and will be reported on later.

The Bonner sphere response was checked with a plutonium-beryllium neutron source. These data and the thick-target data were unfolded to obtain the neutron energy spectra and the average neutron energy. The code PREF was used for the unfolding. The average energy of neutrons from the ^{12}C beam outside of the concrete shielding was measured to be about 4 MeV.

The neutron production model provides a source term for calculating neutron yields inside the shielding, calculating neutron yields outside of the shielding, and calculating the dose equivalent rate at some distance R from the source. These can be compared to the data. We used an approach similar to the "Moyer model"[2] to do calculations outside the shielding. First, the source term is reduced by the R^{-2} dependence from a point source. Then, there is an exponential attenuation of neutrons in the concrete shielding. Appropriate energy-dependent effective attenuation lengths for neutrons in concrete [3] were used. The attenuation by steel shielding was estimated by multiplying the attenuation lengths for concrete by the ratio of steel-to-concrete densities. (The density of concrete used at the NSCL is 2.40 g/cm^3.) The result is an energy distribution of neutrons at point R. The neutron flux energy distributions were then multiplied by appropriate neutron flux-to-dose-equivalent-rate conversions [4]. The dose-equivalent rate at point R was determined by integrating the converted distributions. Figure 2 shows a comparison between the measurements and our model's predictions for a point source outside the shielding.

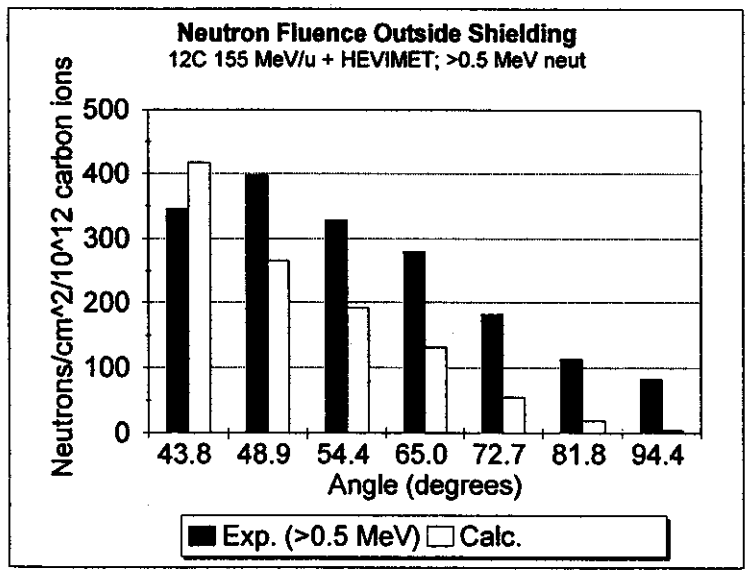

Figure 2: Model calculations compared to measured [Britvich et al.] neutron fluence for a beam of ^{12}C having an energy of 155 MeV/nucleon stopped in a target of Hevimet. The neutrons were measured outside concrete shielding.

Our experience at the NSCL from radiation safety surveys is that for typical beams having around 80 MeV/amu the predicted and measured dose equivalent rates agree to about a factor of two. During the ^{12}C experiment a measurement of dose was made using a portable neutron "rem meter," also calibrated with a PuBe source. Our shielding calculation predicted a higher dose than measured, by a factor of four. The calculations are expected to be conservative because the shielding model assumes no more than one interaction between the neutron and the shielding material. Hence, the calculated spectrum has more high energy neutrons contributing to the dose than is observed. In addition to our new data, a thick target neutron yield experiment [7] using carbon and helium beams in this energy regime has recently been completed at the NSCL. Results from this experiment, when available, also will be very useful to test our model.

We are also investigating the use of more recent nuclear reaction models to generate the source term. Bauer [8] is presently calculating neutron energy spectra and angular distributions using the Boltzmann-Uehling-Uehlenbeck equation. This should result in a significantly improved source term.

a. Superconducting Supercollider Laboratory, Waxahatchie, Tx
b. Institute for High Energy Physics, Protvino, Moscow, Russia

References

1. R.A. Cecil, B.D. Anderson, A.R. Baldwin, R. Madey, A. Galonsky, P. Miller, L. Young, and F.M. Waterman, Phys. Rev. C **21**, 2471 (1980).
2. B.J. Moyer, Lawrence Berkeley Laboratory, University of California Report UCRL-9769 (1961).
3. J.B. Marion and F.C. Young, Nuclear Reaction Analysis, p. 103, North Holland Publishing Company, Amsterdam (1968).
4. H. Wade Patterson and Ralph H. Thomas, Accelerator Health Physics, p. 70, Academic Press, New York, (1973).
5. J.W.N. Tuyn, R. Deltenre, C. Lamberet, and G. Roubaud, CERN Technical Memorandum HS-RP/TM/80-68 (1980).
6. G. Britvich et al., to be published.
7. L. Heilbronn et al., NSCL experiment 92046.
8. W. Bauer, private communication.

A PROTOTYPE ELECTROMAGNETIC CALORIMETER FOR THE SOLENOIDAL TRACKER AT RHIC

W.J. Llope, J. Moskalik, G.D. Westfall, A.M. Vander Molen, D. Swan, and J. Yurkon.

The Relativistic Heavy-Ion Collider (RHIC) at Brookhaven National Laboratory will provide colliding beams of heavy-ions up to gold at 100 GeV/nucleon beginning at approximately the turn of the century. Four major experiments are planned, and the first of these to be fully approved as a construction project is the Solenoidal Tracker At RHIC (STAR) [1]. The physics goals of this experiment involve the search for signatures of the formation of the Quark-Gluon Plasma (QGP), and the study of the properties of strongly interacting matter at very high energy densities, i.e. several GeV/fm^3.

The STAR baseline detector consists of a large Time Projection Chamber (TPC), a Silicon Vertex Tracker (SVT), a room-temperature solenoidal magnet, several sets of trigger counters, and the associated electronics and data acquisition systems. However, none of these detector sub-systems are capable of measuring neutral particles, which may carry as much as a third of the total energy in the event. The capabilities of the STAR experiment are thus greatly enhanced via the addition of an Electromagnetic Calorimeter (EMC), allowing the granular measurement of photons, leptons, and jets with transverse momenta larger than ~150 MeV/c. Observables related to the basic collision dynamics, such as the total and differential transverse energy, as well as observables expected to provide signatures for QGP formation, are available *at the trigger level* from an EMC.

Such electromagnetic calorimetry has been included in the design of the STAR experiment, and general aspects of the design of these calorimeters have already been specified. The STAR-EMC will consist of an azimuthally symmetric barrel and two end-cap calorimeters composed of alternating 5 mm thick lead and 4 mm plastic scintillator plates. The transport of the scintillation light will occur via the coupling of short wavelength-shifting (WLS) optical fibers to the scintillator plates, which are thermally spliced to longer clear fibers (CFs) which are routed through the solenoidal magnet to externally mounted photomultiplier tubes (PMTs). The EMC will be 21 radiation lengths deep and the barrel will be subdivided into 2400 towers (40×60 in η and ϕ) which together cover 2π in azimuth and $|\eta| \leq 1$. Room for a "shower max" detector (SMD) at a depth of 5 X_0 in the barrel EMC to aid in γ/π^0 discrimination and to increase the position resolution is also provided. Fiber-optic visual light and radioactive source systems will be used to calibrate and monitor each read-out channel of the EMC.

Relying heavily on past experience [3] in calorimeter development, the goals of the project described in this Report are the following:

- to construct a small prototypical Pb/Sci/Optical fiber EM calorimeter that can be used to optimize the construction techniques and some details of the design of the full EMC for STAR,
- to develop stable automated methods for construction, as well as efficient assembly and storage jigs,
- to develop stable automated test stations for the grading of the individual components of the optical readout chain,
- to provide optical and radioactive source calibration inputs to each readout channel,
- to implement a fast transportable transputer-based data acquisition system using FERAs and similarly simple electronics, and
- to study the performance of the device for a variety of test beams (p, n, π^+, π^-, e^+, e^-, μ^+, μ^-,

& γ) and energies. In particular, it is important to measure the energy resolution, the lateral shower profiles (for position resolution and side leakage), the longitudinal shower profiles (for lepton/hadron discrimination, albedo, and back leakage), the fast timing characteristics, and the effects of non-normal particle incidence.

A complete assembly drawing of the fiducial volume of the small prototype calorimeter is shown in Figure 1. The calorimeter consists of 6 decoupled towers of 20 layers of 4mm plastic scintillator and 5mm Pb plates. There are two scintillator sizes, 24.3x15.5cm and 24.3x31cm - the upper half of the active region contains 4 towers of the small scintillators (longer edge horizontal), while the lower half has 2 towers of the large scintillators (longer edge vertical). For the STAR-EMC barrel, an (effective) tower size of (0.21,0.105) in (η,ϕ) corresponds to approximately 46x23cm at the 220cm inner radius of the barrel near η=0, which is the same dimension as the sum of one large and one small scintillator stack in the prototype. The scintillator plates are held in place above and below by small I-beam spacers, which hold the Pb plates separated by 6.6mm.

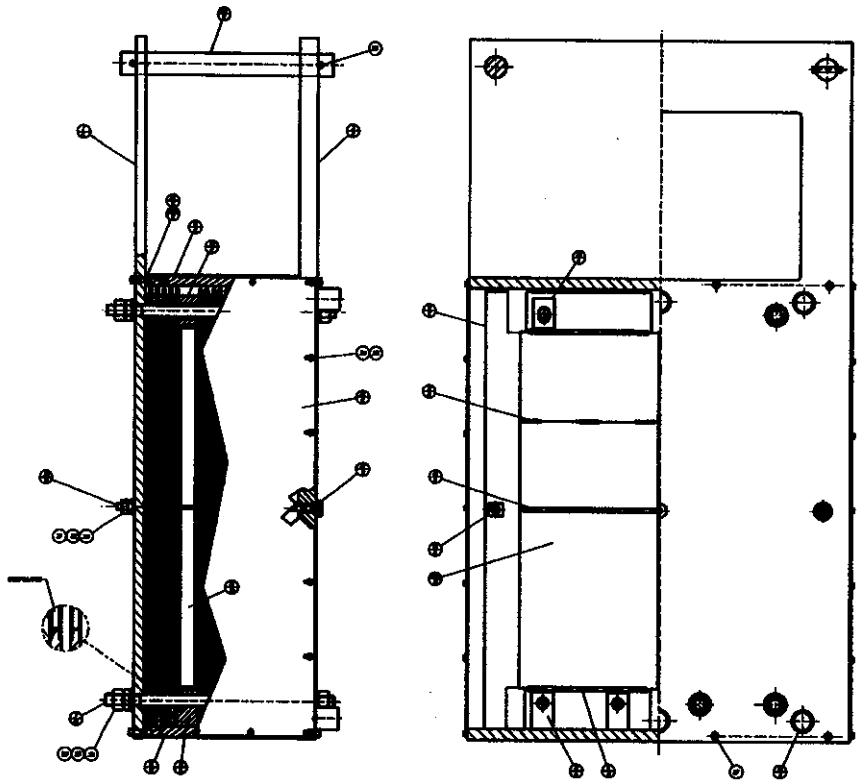

Figure 1: The assembly drawing giving the side and front views of the prototype EMC for STAR being built at the NSCL.

Each scintillator is read-out on both sides by ~0.97mm diameter wavelength shifting fibers, which are attached to the shorter sides of the small scintillators and the longer sides of the large scintillators. The WSFs are thermally spliced to longer clear fibers, which are routed either up or down, then back and out, through flexible tubing to a dark box which holds the PMTs. This box is designed so that a number of different groupings of fibers to PMTs is possible, allowing the changes in the lateral and longitudinal segmentation of the active volume.

A computer operated, temperature controlled, pulsed LED system is being developed to provide

optical calibration inputs to each of the PMTs for the monitoring of short-term gain shifts. A ~1 mCi 60-Co or 137-Cs radioactive source calibration system is also planned to allow monitoring over longer terms and to provide an absolute calibration scale.

An aluminum box of 1" inner thickness is included after 5 Pb/Sci layers to allow the insertion of a prototype SMD, the cables for which are routed horizontally through the side plates of the device. The aluminum front and back plates are similar in thickness to those planned the full EMC (~20mm and ~30mm respectively). The device is about 2'x4'x1' in dimension, and weighs ~1200 pounds.

Many of the raw materials needed to construct the prototype calorimeter, e.g. the lead plates, scintillator plates, optical fibers, and PMTs, have been obtained from other institutions contributing the the STAR-EMC effort. These materials are presently in a dedicated room at the NSCL, which will house the construction and testing of the optical read-out chain. The stacking of the calorimeter will be done in another clean room, perhaps on the "roof" of the NSCL. An automated device for the rapid and efficient thermal splicing of the optical fibers has been obtained from the MSU-HEP group.

Most of the work done so far at the NSCL has concentrated in the specification of the mechanical design of the device. So far, in about 300 hours of CAD, 33 different components have been detailed and are presently being constructed at UCLA. The major concern during the design phase is that one half ton of unstrengthened Pb plates, which will slowly deform with time, must be held in place amongst delicate networks of optical fibers. In this regard, the following aspects of the present design are notable.

Provisions were made for intended and unintended changes in the depth of the device. Such changes are possible due to the slow creep of the unstrengthened Pb, but also given that the design of the stack may be intentionally changed. For example, sheets of 0.5mm non-magnetic stainless steel cladding will eventually be attached to both sides of each Pb plate, adding 1cm to the depth of the stack. Additionally, while the I-beam spacers minimize the stresses on the optical components, they also introduce ~1.3mm air gaps on both sides of each scintillator plate, resulting in a total of 5.2cm of air in the stack of 18.0cm of Pb and scintillator. If all I-beams would be removed, revisions to the top, bottom, and side plates would be necessary. However, an alternative possibility requiring no changes in design is the removal of the I-beam spacers only from the first five layers of Pb/scintillator, i.e. all of the layers in front of the SMD box. The calorimeter would then be ~1.3cm thinner.

To allow for such modest changes in depth, the width of the top and bottom plates are less than that needed to enclose the stack (in the present design, i.e. with the I-beams and without the cladding). Some number of thin shims are used to close the gap, depending on the actual height of the stack after the N^{th} restacking. The bolts that connect the front plate with the top and bottom plates pass through holes in these shims, holding them firmly in place and keeping the interior of the device dark. The bolt holes for the side plates are slotted where they attach to the back plate.

Provisions were also made for subtle changes in the height of the active volume, which also provide adjustable vertical support to the scintillator plates. Above, below, and at the sides of the active volume, the Pb plates are separated by wide aluminum spacer blocks, through which long horizontal bolts are inserted. These blocks are slotted to fit into the (horizontal) I-beam spacers, which hold the scintillators layer from above and below. The spacer blocks at the bottom are fixed in position, while those above are adjustable vertically.

The length of WSF before the splice will be ~5mm less than the length of the side of the scintillator plate to which it is attached. After the splice to the CF and pending some performance tests, the WSF and splice will be attached directly to the scintillator. The scintillator and attached WSF fiber are then

wrapped in DuPont Tyvek or aluminized mylar. The firm attachment of the splice to the scintillator plate will reduce the mechanical stress on the splice itself. The CFs are then bent over a ~2" radius of curvature towards the back of the device in slots in the Pb plates, grouped into bundles, and run through flexible opaque tubing up to the dark box. Commercially available foam packing material will be used to support the fibers in the slots in the Pb plates. The same will also be inserted between the Pb plates at the outward sides of the scintillator layers to provide lateral support to the scintillators.

The uppermost small scintillator plates rest on the tops of the small scintillators below. These are held in place between the Pb plates by small plastic shims. The adjustable spacer blocks allow the use of I-beam spacers between these two scintillators if necessary. However, this region of the active volume is important for the studies of the lateral profiles of the showers, and the I-beams introduce dead regions which can just as easily be studied at other positions on the face of the calorimeter.

The dark box is intended to hold 6 PMTs, and to allow quick changes in the groupings of the CFs to individual PMTs. Commercially available flexible tubing will be used to bring the fiber bundles to the dark box. The PMTs and bases extend out the back of this box, allowing air cooling and free access to the cable connections.

The fibers are held to the face of the phototube in a manner similar to that used in the E814/877 PCal [4]. Cylindrical squeezable rubber couplers (like rubber "stoppers") with about 45 ~1.1mm diameter holes are made with commercially available Silicone rubber compounds and a special mold. The fibers from the individual scintillator plates are inserted into these holes so that they extend ~1mm past the end of this coupler. A fiber carrying the light from the LED optical calibration system is also inserted. Then, a hose clamp is tightened around the circumference of this coupler, firmly holding all of the fibers in place. This assembly is then attached using L-brackets and springs to, in order, a clear silicone rubber "cookie" and the face of the PMT. After a short time, the cookie molds around each fiber, improving the efficiency of this junction. Short sections of fiber are inserted in any unused holes in the coupler to insure that all fibers are evenly held.

A central tube for the transport of a radioactive source through the middle of the active volume is included in the present design. This part of the design is not yet final though, as large solid angle effects are possible with such a strategy. The source pig and motor/encoder for the movement of the source are to be located on a separate stand behind the device. A source path through the calorimeter along the outward sides of the scintillators would be less susceptible to solid angle effects and hence more effective, although such a path might interfere with the cabling of the SMD.

A stacking jig allowing crane and forklift access to the device has been designed and is being constructed at UCLA. The methods to be used to stack the device have been specified. Also specified are many small details, e.g. numbering schemes for the fibers, and several promising fiber routing schemes for the extraction of the lateral and longitudinal shower profiles.

The CAD phase of the project is completed. The optimization of the splicing process for the actual fibers to be used in the prototype has begun. Each spliced fiber and scintillator plate will be individually graded on the bench, and the 240 individual optical readout channels will be assembled. Skilled undergraduates would be employed for the splicing, wrapping, and bench testing. A major goal, given the scale of the full EMC, is the development of rapid and consistent methods for each step in the assembly process.

The prototype is expected to be ready for the collection of test beam data by the middle of July, 1994. It is presently assumed that the first data-taking run will be done with ~200 MeV/nucleon 2-H

beams at the NSCL, allowing the shakedown of the electronics, the transputer DAQ system, the laser calibration system, et cetera.

References

1. Conceptual Design Report for the Solenoidal Tracker at RHIC (STAR), Lawrence Berkeley Laboratory report LBL-5347, June, 1992.STAR Conceptual Design Report Update, January, 1993.
2. Conceptual Design Report, The Electromagnetic Calorimeter for the Solenoidal Tracker at RHIC, Lawrence Berkeley Laboratory report LBL-5380, September, 1993.
3. T.C. Awes *et al.*, Nucl. Inst. Methods A279, 479 (1989); E. Bernardi *et al.*, Nucl. Inst. Methods A262, 229 (1987); A. Beer *et al.*, Nucl. Inst. Methods 224, 360 (1984); C. DeMarzo *et al.*, Nucl. Inst. Methods 217, 405 (1983); J. Fent *et al.*, Nucl. Inst. Methods 211, 315 (1983); M.J. Corden *et al.*, Phys. Scripta 25, 11 (1982); H. Abramowicz *et al.*, Nucl. Inst. Methods 180, 429 (1981); M. Basile *et al.*, Nucl. Inst. Methods 163, 93 (1979); W. Hofman *et al.*, Nucl. Inst. Methods 163, 77 (1979); M. Holder *et al.*, Nucl. Inst. Methods 148, 235 (1978).
4. D. Fox *et al.*, Nucl. Inst. Methods A317, 474 (1992); J. Simon-Gillo *et al.*, Nucl. Inst. Methods A309, 427 (1991); J. Simon-Gillo, Ph.D. Thesis. Texas A&M University, 1991 (unpublished).

OPERATING EXPERIENCE WITH THE K100 NEUTRON THERAPY CYCLOTRON; MEDICAL USE ON A FULL SCHEDULE

H. Blosser & R. Maughan[a]

In the years 1984-1990 Detroit's Harper Hospital sponsored the construction of a superconducting medical cyclotron at the National Superconducting Cyclotron [1,2]. The goal of this project was to provide a neutron beam with characteristics appropriate for treating cancer patients with tumors resistant to conventional photon radio-therapy. After testing at the NSCL, the cyclotron was to be installed at Harper Hospital and function as a standard element of the array of therapeutic radiation producing devices in the Gershenson Radiation Oncology Center. From the perspective of the medical users it was very desirable for the cyclotron to be operationally as similar as possible to operation of a medical electron linear accelerator (the main device used for treatment of cancer in modern radiation therapy centers). The major step in achieving the desired functional similarity, namely mounting the cyclotron directly on a rotating gantry in the same fashion as a medical linac, had come into the regime of feasibility as a consequence of the order-of-magnitude weight reduction which high field superconducting cyclotrons had established relative to room temperature cyclotrons. Thus a superconducting K100 cyclotron to accelerate deuterons to 50 MeV could be built with an overall weight of about 25 tons giving a weight reduction of more than 10 fold compared to the 250 to 350 tons of room temperature K100 cyclotrons.

By the early summer of 1990, design, construction, and testing of the medical cyclotron at the NSCL had been completed and in July 1990 the accelerator and gantry were moved to the Gershenson Radiation Oncology Center of Harper Hospital. With the cyclotron installed at the hospital, operation with beam resumed in August 1990, and patient treatments began in September 1991 (after about one year of biological testing, comparing dose monitoring devices with other neutron facilities in the world, training medical staff, etc.).

The general arrangement of the cyclotron and support system is shown in Fig. 1. The cyclotron mounts on a pair of large steel rings with an opposite counter weight and is able to rotate through a full 360 degree arc relative to a patient positioned on a conventional radiation therapy treatment table. A novel moving floor system provides a comfortable working situation for medical technicians even when the cyclotron is directly below the patient, the passive, roller mounted wood floor being pushed out of way by the cyclotron as it rotates to these angles.

The general arrangement of the cyclotron is shown in Fig. 2. The cyclotron is extremely simple since it operates always at a fixed energy and produces neutrons in an internal beryllium target so that no extraction system is required. Adjustable parameters are then the ion source gas flow and current, the voltage on the radiofrequency accelerating system, and the current in the main superconducting coil. This simplicity allows a daily operating regime in which the cyclotron is turned on at the beginning of each day by a member of the Oncology Center's Physics/Engineering support group, and, after calibration tests, the cyclotron is turned over to medical technicians (nurses) who use it throughout the day to deliver treatments to patients in a pattern quite identical to the operating pattern for the medical linear accelerators. The Medical Center in fact operates on a personnel plan where medical technicians are periodically rotated from accelerator to accelerator so that each technician is familiar with all of the radiation delivery devices in the center; technician assignments on a day-to-day or week-to-week basis can then provide for vacations, sick leave, holidays, etc. by adjustments within the total group of medical technicians; the dislocation due to an unexpected absence is then much easier to absorb then would be the case if a particular accelerator had its own dedicated staff.

At the beginning of a work day, the morning helium fill and start up of the cyclotron involves a period of 2-1/2 hours and this work is started at 5:30 a.m. so that the cyclotron will be ready for patient treatments beginning at 8:00 a.m. The majority of the start up time is occupied by the helium fill with an additional 30 minutes required on Monday morning since the cyclotron is allowed to warm to approximately 60 degrees Kelvin over the weekend to minimize personnel and energy costs of the refrigeration system. The start up is handled by a single technician who after the fill is complete turns on the magnet (requiring approximately 30 minutes) and thereafter the ion source and radiofrequency system and performs a series of operational tests and calibrations. The magnet then remains on for the rest of the operating day whereas both ion source and radiofrequency system are switched off between irradiations (thereby providing redundant protection against accidental system start up).

A gradual buildup of active medical protocols (and patient load) occurred through the year 1992 and by the spring of 1993 the facility had reached a level of full exploitation, carrying a patient load in which approximately 450 radiation fields would be delivered each month in approximately 150 patient treatment sessions. At this level of utilization, the patient load shown in Table 1 is approximately the same as that carried by other neutron therapy facilities at a corresponding stage of development.

The majority of patients treated have been prostate patients in stages 3 and 4 (i.e. advanced, disseminated tumor), this being the most common example of a very threatening illness not amenable to surgical correction and highly resistant to conventional photon therapy. The initial results of the neutron therapy program have been highly favorable relative to photon comparisons, but overall medical conclusions must await results of evaluations of possible late after effects, a problem which other studies have found to be more severe with neutrons than with photons. (Recently published results [3] from the University of Washington neutron therapy facility show that these undesirable late effects are greatly reduced in centers where both 360 degree gantries and fully shaped collimation systems are available; the fact that both of these features are provided in the Harper Hospital neutron therapy system then provides a basis for optimism in expecting that five year evaluations will be comparably favorable to the results now available.)

Figure 3 shows the operating availability of the cyclotron and the "utility" i.e. the fraction of availability time in which patient treatments were actually in process. For nine of the twelve months availability was at the 90% level whereas substantial disruptions occurred in August, November and January due largely to faulty operating procedures with the liquid helium system, which have since been corrected.

a. Gershenson Radiation Oncology Center, Harper Hospital, 3990 John R., Detroit, MI 48201

References

1. Superconducting Cyclotron for Medical Application. H. Blosser, J. Bailey, R. Burleigh, D. Johnson, E. Kashy, T. Kuo, F. Marti, J. Vincent, A. Zeller, E. Blosser, G. Blosser, R. Maughan, W. Powers, J. Wagner, IEEE Trans. on Mag. 28(1989)1746.
2. A Superconducting Cyclotron for Neutron Radiation Therapy. R. Maughan, W. Powers, H. Blosser, Medical Physics 21(1994)779.
3. Photon versus Fast Neutron External Beam Radiotherapy in the Treatment of Locally Advanced Prostrate Cancer: Results of a Randomized Prospective Trial. K. Russell, R. Caplan, G. Laramore, C. Burnison, M. Maor, M. Taylor, S. Zink, L. Davis, T. Griffin, Int. J. Radiation Oncology Biol. Phys., 28(1993)47.

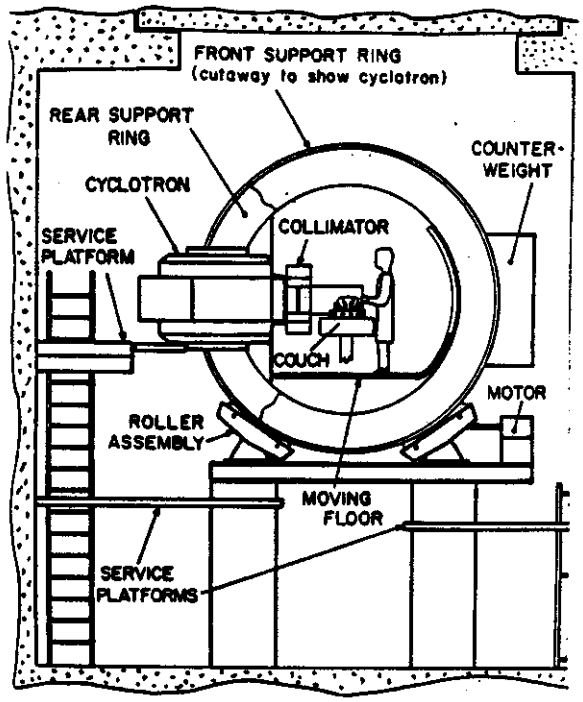

Fig. 1 -- Section view of the medical cyclotron facility showing the cyclotron support ring, patient couch (with patient) and technician standing on the moveable floor.

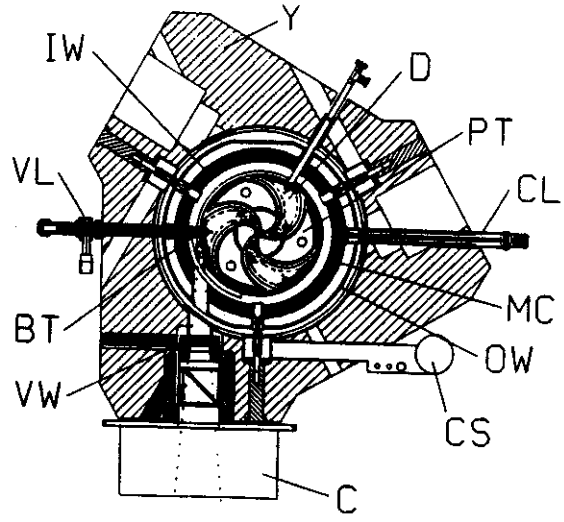

Fig. 2 -- Median plane section view of the cyclotron proper BT-beryllium target, C-collimator, CL-coil leads, CS-cryostat safety port, D-magnet pole tip, IW-cryostat inner wall, MC-main coil, OW-cryostat outer wall, PT-accelerating electrode, VL-vacuum lock, VW-vacuum window & Y-magnet yoke.

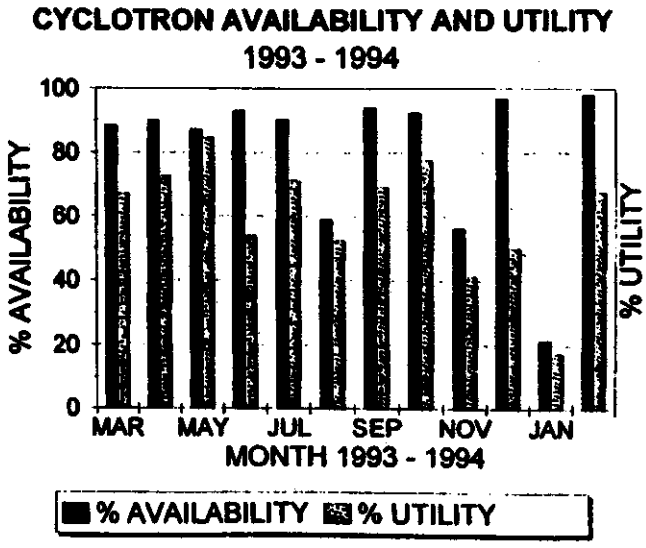

Fig. 3 -- Operating statistics on the superconducting cyclotron for first year of fully scheduled therapy operation.

COMPARISON WITH SOME OTHER MAJOR FACILITIES

YEAR	ROC # OF Tx	ROC # OF FIELDS	NAC # OF Tx	NAC # OF FIELDS	U OF W # OF Tx	U OF W # OF FIELDS
1	299	711	112	241	1493	2954
2	1392	3910	872	1999	1823	3674
3			1203	2977	1966	4016
4			1482	3767	1830	3845
5			1354	3513	1599	3485
6					1575	3509
7					1947	4360
8					2068	4629

Table 1--Statistical comparison of number of patient treatment sessions "Tx" and the total number of radiation "fields" for the Harper facility (ROC) and for the neutron therapy facilities at the National Accelerator Centre in Cape Town, South Africa (NAC) and for the neutron therapy facility at the Univ. of Washington Hospital in Seattle, WA. (UofW).